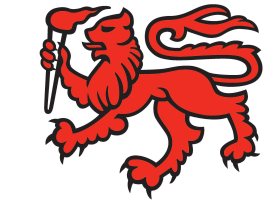

Vertical Land Motion of the Australian Plate

by

Anna R. Riddell

Bachelor of Surveying and Spatial Sciences (Honours)

School of Geography, Planning, and Spatial Sciences
College of Sciences and Engineering

Submitted in fulfilment of the requirements
for the degree of Doctor of Philosophy (Geomatic Engineering)

University of Tasmania, January 2021

Declaration of originality

This thesis contains no material which has been accepted for a degree or diploma by the University or any other institution, except by way of background information and duly acknowledged in the thesis, and to the best of my knowledge and belief no material previously published or written by another person except where due acknowledgement is made in the text of the thesis, nor does the thesis contain any material that infringes copyright.

Anna Riddell
(20 January 2021)
PhD Candidate
School of Geography, Planning, and Spatial Sciences
University of Tasmania

Authority of access

The publishers of the papers comprising Chapters 2, 3 and 4 hold the copyright for that content, and access should be sought from the respective journals:

Chapter 2 was published by Wiley as Riddell, A. R., King, M. A., Watson, C. S., Sun, Y., Riva, R. E. M. & Rietbroek, R. 2017. Uncertainty in geocenter estimates in the context of ITRF2014. Journal of Geophysical Research: Solid Earth, 122, 4020-4032, doi: 10.1002/2016JB013698.

Chapter 3 was published by Wiley as Riddell, A. R., King, M. A. & Watson, C. S. 2020. Present-Day Vertical Land Motion of Australia From GPS Observations and Geophysical Models. Journal of Geophysical Research: Solid Earth, 125, doi: 10.1029/2019jb018034. This is an open access article under the terms of the Creative Commons Attribution License, which permits use, distribution and reproduction in any medium, provided the original work is properly cited.

Chapter 4 has been submitted and is under review with Geophysical Journal International, 20 September 2020.

Chapter 4 has also been published as Riddell, A., King, M. & Watson, C. 2020. Ongoing postseismic vertical deformation of the Australian continent from far-field earthquakes. Earth and Space Science Open Archive, doi: 10.1002/essoar.10504158.1.

The remaining non published content of the thesis may be made available for loan and limited copying and communication in accordance with the Copyright Act 1968.

Anna Riddell
(20 January 2021)
PhD Candidate
School of Geography, Planning, and Spatial Sciences
University of Tasmania

Statement of co-authorship

The following people and institutions contributed to the publication of work undertaken as part of this thesis:

Candidate Anna Riddell, School of Geography, Planning, and Spatial Sciences, University of Tasmania

Author 1 Matt King, University of Tasmania (Primary Supervisor)

Author 2 Christopher Watson, University of Tasmania (Supervisor)

Author 3 Yu Sun, Delft University of Technology (Co-author)

Author 4 Riccardo Riva, Delft University of Technology (Co-author)

Author 5 Roelof Rietbroek, University of Bonn (Co-author)

Author details and their roles:

Paper 1: Riddell, A. R., King, M. A., Watson, C. S., Sun, Y., Riva, R. E. M. & Rietbroek, R. 2017. Uncertainty in geocenter estimates in the context of ITRF2014. Journal of Geophysical Research: Solid Earth, 122, 4020-4032.

Located in Chapter 2. Riddell (80%), King (5%), Watson (5%), Sun (2.5%), Riva (2.5%), Rietbroek (5%)

Anna Riddell was the primary author who developed the idea, carried out its execution and analysis, and was responsible for the manuscript preparation. Matt King and Christopher Watson motivated and assisted in the design of the study, contributed to the interpretation and critically revised the manuscript. Yu Sun and Riccardo Riva provided data from previous analysis; Roelof Rietbroek provided data and validation analysis. All authors helped refine the manuscript and gave final approval for publication.

Paper 2: Riddell, A. R., King, M. A. & Watson, C. S. 2020. Present-Day Vertical Land Motion of Australia From GPS Observations and Geophysical Models. Journal of Geophysical Research: Solid Earth, 125.

Located in Chapter 3. Riddell (80%), King (10%), Watson (10%)

Anna Riddell was the primary author who developed the idea, carried out its execution and analysis, and was responsible for the manuscript preparation. Matt King and Christopher Watson motivated and assisted in the design of the study, contributed to the interpretation and critically revised the manuscript. All authors helped refine the manuscript and gave final approval for publication.

Paper 3: Riddell, A. R., King, M. A. & Watson, C. S. 2020. Ongoing postseismic vertical deformation of the Australian continent from far-field earthquakes. Submitted to Geophysical Journal International.

Located in Chapter 4. Riddell (80%), King (10%), Watson (10%)

Anna Riddell was the primary author who developed the idea, carried out its execution and analysis, and was responsible for the manuscript preparation. Matt King and Christopher Watson motivated and assisted in the design of the study, contributed to the interpretation and critically revised the manuscript. All authors helped refine the manuscript and gave final approval for publication.

We the undersigned agree with the above stated proportion of work undertaken for each of the above published (or submitted) peer-reviewed manuscripts contributing to this thesis:

Anna Riddell (18 May 2020)
Candidate
School of Technology, Environments and Design

Matt King (29 May 2020)
Primary Supervisor
School of Technology, Environments and Design

Elaine Stratford (16 June 2020)
Head of School
School of Technology, Environments and Design

Abstract

Vertical Land Motion of the Australian Plate

by Anna RIDDELL

The surface deformation field on Earth represents an integrated response to a complex array of geophysical processes that occur over different temporal and spatial scales. High-accuracy measurements of surface deformation can therefore inform our understanding of processes ranging from past and present mass loading (e.g. water redistribution between land and ocean, atmospheric pressure, continental surface and groundwater storage, non-tidal ocean, glacial isostatic adjustment), crustal dynamics (e.g. tectonic motion, elastic and viscoelastic relaxation), as well as subsurface and internal processes (e.g. geocentre motion, mantle convection). The vertical component of surface deformation is both particularly important, yet problematic to observe. Vertical deformation informs our understanding of processes that often present a natural hazard to society (e.g. earthquake, tsunamis and volcanic eruptions), and are critical to enable quantitative predictions of regional sea level change which poses an increasing concern to coastal and island communities.

Geodetic time series are used to monitor the deformation of the solid Earth, but their accurate interpretation depends entirely on the stability and accuracy of the underlying reference frame. This thesis undertakes a homogeneous reprocessing of Global Positioning System (GPS) data to serve as the foundation to aid in the understanding of reference frame accuracy and stability, as well as to investigate the present-day deformation of the Australian continent. With a focus on the vertical coordinate component at GPS site locations installed throughout the Australian AuScope network, space geodetic time series are utilised alongside modelled estimates of mass surface transport, glacial isostatic adjustment, coseismic offsets and postseismic deformation. Through the use of time series and spectral analysis, noise characterisation and spatiotemporal filtering, three key contributions are made to improving knowledge regarding vertical deformation across the Australian continent.

First, this thesis explores the temporal variation of the motion of the reference frame origin and its deviation from an assumption of long-term linear motion. The realisation of the International Terrestrial Reference Frame (ITRF) origin is reliant on a single geodetic technique, Satellite Laser Ranging (SLR), which is sensitive to the movement of the Earth's centre of mass. A comparison of the network translations calculated from surface mass transport models with those observed by SLR finds that unaccounted for variability and temporal correlation exists. Non-linear trends and coloured noise are identified in the SLR translations, which increases uncertainties in the rates by a factor of five (upper bound) compared to a linear and white-noise-only assumption. The uncertainty of the ITRF2014 SLR Z rate is reduced by

27% since the previous model of ITRF2008 with the consideration of a powerlaw and white noise model and short-term non-linear motion. The attainment of a stable reference frame with increasing accuracy to serve as the foundation for all geospatial activity presents an ongoing challenge for the Earth Science community.

Second, the disagreement between large-scale geophysical theory and present-day observations of land motion across Australia is investigated. Recent but sparsely distributed GPS measurements suggest that the vertical motion of the Australian continent at permanent GPS sites is between 0 and -2 mm/yr. Current understanding of the Earth's rheology and the knowledge that Australia is located in the far-field of past ice sheet loading suggests that the expected vertical motion of the crust should be close to zero. GPS data from more than 100 new Australian Global Navigation Satellite System (GNSS) stations are processed, capitalising on the recent national investment in geodetic infrastructure. The investigation of large-scale geophysical models and GPS observations of vertical land motion in Australia reveals that the velocities disagree at the millimetre per year level. The novel use of spatiotemporal filtering, multivariate regression, and modelling short-term geophysical effects is shown to reduce the uncertainty of vertical velocity estimates at Australian GPS sites by 35%. It is shown that despite the level of noise in the filtered time series remaining too high to isolate land motion from glacial isostatic adjustment (the solid Earth response to ice-ocean mass changes), significant insight is gained into the spatial and temporal evolution of Australian GPS sites and the surface motion they monitor. The El-Niño Southern Oscillation is identified as a driver of spatially coherent motion following the removal of surface mass transport as common mode deformation.

Third, the elastic and viscoelastic response of the crust within the Australian plate is investigated using several large earthquakes along the Indo-Australian plate boundary and a recent intraplate earthquake. Postseismic motion of the Australian continent has been comprehensively studied in the horizontal direction, but there is a lack of studies that investigate the vertical component. Earthquake events in the far-field of AuScope GNSS sites are identified, selecting events that are not yet present within publicly available deformation models. Ongoing far-field postseismic deformation of the Australian continent from large plate-boundary earthquakes is supported by evidence from forward viscoelastic models and GPS observations. Evidence of changes in vertical velocity up to several mm/yr are observed in the GPS time series following large earthquakes. Models constrained by earthquake rupture parameters as far as 2000 km from the Australian continent suggest that coseismic deformation occurs in the vertical direction by up to 3 mm and postseismic deformation up to 4 mm/yr over 2004.9-2010.0 (with the magnitude of both varying spatially and by earthquake). Modelled postseismic deformation due to an historic earthquake in 1979 to the south of New Zealand indicates ongoing present-day deformation in

Australia. Far-field deformation from intraplate and large plate boundary earthquakes can be observed in Australian GPS time series and provides information on how the Earth responds to changing stress fields.

Each of these advances presents a novel incremental advance to our understanding of surface deformation across the Australian plate. The inclusion of coloured noise and non-linear transients in the definition of geocentre motion is important to accurately assess frame uncertainty and its contribution to interpretation of geophysical processes. The surface deformations modelled and observed in this thesis push the limit of signal to noise present in current space geodetic analyses and available geophysical models. New insights in the spatial patterns of the surface deformation field informs our understanding of relevant processes and highlights an ever-increasing demand for accurate position and velocity estimates.

Acknowledgements

Firstly I would like to express my gratitude to all those that have been part of my PhD journey. To take on a PhD feels like a very selfish exercise and I am forever grateful to those that have been there for the good days and the not so good days.

I am appreciative for the financial and moral support from Geoscience Australia. The scholarship enabled me to focus on my research with minimal distraction. I thank my colleagues at GA for their belief in me and continued encouragement. I look forward to returning to working at GA.

Thank you to my fellow scholars within Geography and Spatial Sciences. The tea-room culture and initiation of cake-able offences provided a welcome forum for collegial discussion, idea bouncing, fact checking and random discussion. I enormously enjoyed my time at the University of Tasmania and was proud to represent the University at various science and outreach events, made even more enjoyable by getting to play with the augmented sandpit, tectonic jigsaws and inflatable beach balls.

Thank you to my supervisors Matt and Christopher, for constantly providing sound advice and guidance. The friendship between you was a joy to witness, with your quick wit and intelligent banter making complex and challenging problems understandable and enjoyable. It has been an honour to work with you and I am grateful for your willingness to support my academic and personal adventures.

Thank you to my friends and family who have inevitably sat through my garbled explanations of the conundrum of the day. I apologise for the days where I needed to download my problems with little consideration of the mental dump I was submitting you to. Thank you for listening with patience, providing me with encouragement and for sharing in my achievements. Your ongoing support has been a lifeline. A special thank you to Peta for her help with the awesome graphics.

A very special mention goes to my extraordinary husband Rob for the endless support, love and parenting of our two children. This research would not have been possible without being able to come home to you at the end of each day. You have let me chase my dreams for the last 4 years and I only hope that I can provide you with an equal measure of the strength and endorsement you have provided me.

Contents

List of Figures

List of Tables

List of Abbreviations

AIC	**A**kaike **I**nformation **C**riteria
ANU	**A**ustralian **N**ational **U**niversity
AOD1B	**A**tmosphere and **O**cean **D**ealiasing level-1B
BIC	**B**ayesian **I**nformation **C**riteria
CATREF	**C**ombination and **A**nalysis of **T**errestrial **Re**ference **F**rames
CE	**C**entre of **E**arth
CF	**C**entre of **F**igure
CM	**C**entre of **M**ass
CME	**C**ommon **M**ode **E**rror
CN	**C**entre of **N**etwork
CORS	**C**ontinuously **O**perating **R**eference **S**tation
CSR	**C**enter for **S**pace **R**esearch at University of Texas
DORIS	**D**oppler **O**rbitography and **R**adiopositioning **I**ntegrated by **S**atellite
ECMWF	**E**uropean **C**entre for **M**edium-range **W**eather **F**orecasts
ENSO	**E**l-**N**iño **S**outhern **O**scillation
GFZ	**G**eo**f**orschungs**Z**entrum Potsdam, German Research Centre for Geosciences
GGM	**G**eneralised **G**auss **M**arkov
GIA	**G**lacial **I**sostatic **A**djustment
GIPSY	**G**NSS-**I**nferred **P**ositioning **Sy**stem and Orbit Analysis Simulation Software
GLDAS	**G**lobal **L**and **D**ata **A**ssimilation **S**ystem
GNSS	**G**lobal **N**avigation **S**atellite **S**ystem
GPS	**G**lobal **P**ositioning **S**ystem
GRACE	**G**ravity **R**ecovery **A**nd **C**limate **E**xperiment
GRanD	**G**lobal **R**eservoir **an**d **D**am database
ICA	**I**ndependent **C**omponent **A**nalysis
ICCC	**I**nter-**C**ommission **C**ommittee on "Geodesy for Climate Research
IERS	**I**nternational **E**arth **R**otation and Reference Systems **S**ervice
ILRS	**I**nternational **L**aser **R**anging **S**ervice
IMBIE	**I**ce-sheet **M**ass **B**alance **I**nter-comparison **E**xercise
InSAR	**In**terferometric **S**ynthetic **A**perture **R**adar
IPCC	**I**ntergovernmental **P**anel for **C**limate **C**hange
ITRF	**I**nternational **T**errestrial **R**eference **F**rame
JPL	**J**et **P**ropulsion **L**aboratory
LAGEOS	**L**aser **G**eodynamics **S**atellite
MSM	**M**ass **S**urface **M**odel
MERRA	**M**odern- **E**ra **R**etrospective analysis for **R**esearch and **A**pplications
MPIM	**M**ax **P**lank **I**nstitute for **Meteorology**
NASA	**N**ational **A**eronautics and **S**pace **A**dministration
OBP	**O**cean **B**ottom **P**ressure
OMCT	**O**cean **M**odel for **C**irculation and **T**ides
PCA	**P**rincipal **C**omponent **A**nalysis
PLW	**P**ower **L**aw and **W**hite

PPP	**P**recise **P**oint **P**ositioning
PREM	**P**reliminary **R**eference **E**arth **M**odel
PSD	**P**ower **S**pectral **D**ensity
RACMO	**R**egional **A**tmospheric **C**limate **Mo**del
RINEX	**R**eceiver **In**dependent **Ex**change
RMS	**R**oot **M**ean **S**quare
SINEX	**S**olution **In**dependent **Ex**change
SLR	**S**atellite **L**aser **R**anging
SMT	**S**urface **M**ass **T**ransport
VLBI	**V**ery **L**ong **B**aseline **I**nterferometry
VLM	**V**ertical **L**and **M**otion
WRMS	**W**eighted **R**oot **M**ean **S**quare

Chapter 1

Introduction

1.1 Overview

We live on a dynamic planet. Observations from seismic and geodetic techniques as well as modelling approaches inform our understanding of the deformation of the Earth's surface. Over recent decades horizontal site velocities from space geodetic techniques such as the Global Positioning System (GPS) have been used to study plate tectonic kinematics in global (e.g. Argus and Heflin, 1995; Kogan and Steblov, 2008; Larson et al., 1997) and regional settings (e.g. Márquez-Azúa and DeMets, 2009; McClusky et al., 2000). More recently, vertical velocities from GPS have been used to determine absolute sea level from tide gauges (Bouin and Wöppelmann, 2010; Han et al., 2015; Wöppelmann et al., 2009; Wöppelmann and Marcos, 2016), to assess the response of the Earth's surface to previous ice loading (e.g. Nocquet et al., 2005; Sella et al., 2007), and for monitoring transient and ongoing deformation in earthquake prone zones (e.g. Beavan et al., 2010a; Correa-Mora et al., 2009) and in their far-field (Tregoning et al., 2013). For an accurate and stable reference frame, unbiased position estimates and velocities with realistic uncertainties are necessary to advance understanding in each of these application areas.

Our knowledge of the properties of the upper part of the Earth's crust, including its modern-day stress fields, informs decisions with implications across social, scientific and economic domains. Present-day geological and geomorphological events that cause deformation of the Earth's crust are controlled in part by stress fields and crustal dynamics that can be interpreted to better understand the 'when, where and how' of earthquake events (Hillis et al., 2008; Sandiford et al., 2004; Seeber and Armbruster, 2000; Stein, 1999), and that helps inform our understanding of how solid-earth deformation occurs. Geodetic point positioning techniques, such as Global Navigation Satellite System (GNSS), and in particular GPS, can provide time series of site locations suitable to monitor crustal dynamics in space and time (Bock and Melgar, 2016). Three-dimensional time series of deformation across networks of GNSS sites offers an important insight into evolving crustal stress fields, vital for improving our understanding of various Earth processes, such as solid-earth deformation.

The assessment of vertical land motion at tide gauge sites is key to understanding relative and absolute sea level changes over the last century in both global and regional contexts (Santamaría-Gómez et al., 2017; Wöppelmann and Marcos, 2016). Relative sea level measurements are important for understanding local implications of inundation and adaptation methods (Karegar et al., 2017), yet differ from absolute sea level measurements derived from satellite altimetry. Under a warming climate, rising sea levels are one of the key factors that will impact coastal communities (Gehrels, 2016; Han et al., 2015). The measurement of sea level by traditional techniques, such as tide gauges, is complicated by the location of the instrument on land which is in turn influenced by motion of the Earth's surface (King et al., 2012; Wöppelmann and Marcos, 2016). Monitoring of surface motion at tide gauge locations is commonly undertaken using levelling surveys or observed as position differences over time with GNSS. The sea level problem is one of many drivers that require high accuracy and spatially comprehensive measurements of vertical land motion.

Australia's economic, social and cultural identities are strongly tied to the coast, with 85% of its population living within 50 km of the coastline (Clark and Johnston, 2017). The majority of the nation's critical infrastructure – transport, energy, commercial, defence and residential – lies along the coastline and are vulnerable to changes in sea level and the occurrence of extreme events (Steffen et al., 2014). Global sea level is the topic of considerable research with billions of dollars invested globally towards understanding coastal impacts, adaptation and mitigation (Steffen et al., 2014; Steffen et al., 2019). Non-linear deformation caused by short-term crustal dynamics can influence relative sea level measurements from tide gauges where it is commonly assumed that crustal motion is linear, being driven by millennial-scale geophysical processes. Noting the importance of vertical land motion estimates for climate and geophysical applications, reducing the scatter and common-mode errors in GNSS observations will enable improved identification, quantification, and interpretation of geophysical phenomena, as well as providing an understanding of the drivers of Australia's vertical movement.

Geodetic time series include signals which vary over days to millennia and over global to highly local spatial scales. Figure 1.1 shows a schematic representing major geophysical drivers of these signals globally. Because they act over long temporal and spatial scales, of particular interest are Glacial Isostatic Adjustment (GIA), the solid Earth's response to past ice-ocean loading changes (Mitrovica and Milne, 2002; Tamisiea and Mitrovica, 2011), and postseismic deformation (Hearn, 2003; Tregoning et al., 2013). Both are due to viscoelastic deformation of the Earth's mantle. Models of GIA are in contradiction with observed vertical motion for Australia, with models suggesting $\sim$ 0.5 mm/yr uplift, but geodetic observations suggesting $\sim$ 1.0 mm/yr subsidence, while postseismic deformation of Australia is considered to be negligible in the vertical (Altamimi et al., 2016; Tregoning et al., 2013). However, these models and geodetic data are yet to be fully investigated in Australia. If these

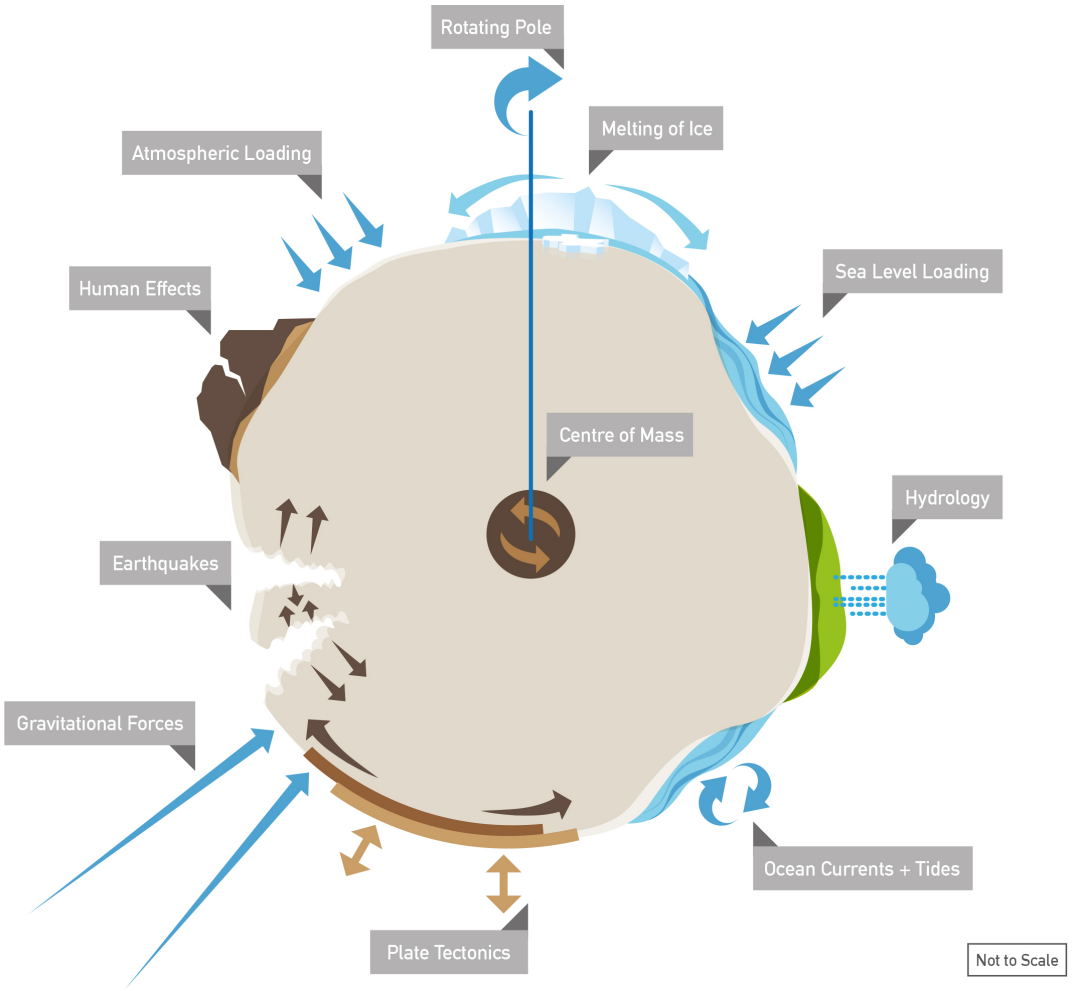

FIGURE 1.1: Schematic illustration of the broad number of processes that influence surface position

signals are not of primary interest, then they represent potentially important biases or noise in the time series, especially so for studies which assume long-term linear surface motions (Hearn, 2003). Deformation from both GIA and postseismic sources in Australia is examined in this thesis as contributing factors to the observed vertical movement of the continent.

Beyond these large-scale geophysical signals, geodetic time series also include other geophysical signals and measurement error, which can be considered as sources of noise. Addressing the need to reduce noise and uncertainty in GNSS analysis and in the realisation of the geodetic terrestrial reference frame is a further primary focus of this thesis. GNSS analysis still faces many sources of error, bias and uncertainty (Bock and Melgar, 2016). The scientific need to reliably estimate small deformations in three-dimensions underlies a constant refinement to GNSS analysis and interpretation to achieve greater accuracy, precision and reference frame stability. Residual error will remain in GNSS coordinate solutions due to inaccurate models of otherwise systematic biases, irrespective of whether the models are applied directly or

indirectly at the observation level by the user. For example, the velocity of the vertical coordinate component has been shown to be sensitive to the (mis-)modelling of surface mass loading processes (e.g. Tregoning and Dam, 2005; van Dam et al., 2001), Earth rotation parameters and satellite and clock products (e.g. Teferle et al., 2009), inadequate modelling of the troposphere (e.g. Boehm et al., 2006), improper application of transmitter and receiver antenna phase variations and offsets (e.g. Cardellach et al., 2007; Ge et al., 2005), neglecting higher order ionospheric terms (e.g. Fritsche et al., 2012; Hernández-Pajares et al., 2007; Kedar et al., 2003), the treatment of seismic deformation (e.g. Métivier et al., 2014; Tregoning et al., 2013), signal reflection and multipath (e.g. King and Watson, 2010), and the over- or under-zealous application of discontinuities in coordinate time series (e.g. Gazeaux et al., 2013).

The International Terrestrial Reference Frame (ITRF) attempts to meet accuracy and stability goals of the Global Geodetic Observing System of 1 mm and 0.1 mm/yr respectively (Gross et al., 2009). However, non-linear geocentre motion has exceeded 0.1 mm/yr and can no longer be considered as a negligible effect (Dong et al., 2014). The need to monitor global change processes, such as distinguishing relative sea level rise from land subsidence (Wöppelmann and Marcos, 2016); satellite altimetry estimates of global sea level (Desai and Ray, 2014); global plate motion models (Argus et al., 2010); and for comparison of site motion models, such as postglacial rebound and ice mass loss (Argus, 2012), at a level below 1 mm/yr illustrates the requirement for an accurate and precise global geodetic reference frame with the consideration of non-linear temporally correlated error sources.

Much of the noise in geodetic GNSS time series, which leads to biases in velocity when estimating a linear model, have large spatial and temporal scales spanning months to years. Therefore, at least partly, the noise is expressed as regionally correlated signals that can mask reduced accuracy with improved precision. Geodetic measurements of site positions are not considered independent but are temporally correlated in both regional networks (e.g. Beavan, 2005; Langbein, 2008; Williams et al., 2004; Zhang et al., 1997), and global networks (e.g. Amiri-Simkooei, 2007; Mao et al., 1999; Santamaría-Gómez et al., 2011; Williams et al., 2004). Some of these error sources can be identified as having a common source with similar magnitudes over a large area and can be consequently removed using spatial filtering methods (Wdowinski et al., 1997). This reduces the day-to-day scatter and improves the uncertainty estimates on the parameters such as site velocities (e.g. Dong et al., 2006; Nikolaidis, 2002; Teferle et al., 2009; Wdowinski et al., 1997).

The inappropriate treatment of coloured and flicker noise can lead to uncertainties a factor of five too small (Riddell et al., 2017), thus artificially inflating confidence in the estimation of the underlying geophysical process. This thesis seeks to improve GNSS time series interpretation across the Australian continent using spatiotemporal filtering to identify spatially coherent patterns of behaviour. Traditionally, geodetic site motions have been most commonly modelled as being linear over time

with possible instantaneous offsets due to hardware changes or seismic evidence and annual/semi-annual signals with time-constant amplitudes. The notion of a standard linear site model is slowly being challenged as improvements in analysis approaches are made that deliver an insight into non-linear and transient signals.

To detect and correctly interpret geophysical signals of interest in geodetic time series, the residual noise needs to be first understood (Beavan, 2005; Davis et al., 2012). To determine the change over time at a site (its velocity), the standard procedure is to estimate a linear trend (intercept and slope) together with seasonal signals (in-phase and quadrature components to periodic signals with solar annual and semi-annual periods). With amplitudes of a few millimetres, the periodic components can be partially attributed to surface mass transport from hydrologic loading (van Dam et al., 2001), atmospheric loading (Tregoning and Watson, 2009; van Dam et al., 1994), non-tidal ocean loading (van Dam et al., 2012; Williams and Penna, 2011), and present-day ice mass changes (Riva et al., 2017). As a prerequisite to estimating the site velocity (position velocity) with realistic uncertainty, the noise structure in geodetic time series needs to be modelled and quantified (Amiri-Simkooei, 2009; King and Watson, 2010; Langbein, 2004; Langbein, 2012). The choice of processing strategy (baseline or point positioning), observation models, terrestrial reference frame, site dependent effects, as well as time period and span all influence velocities estimated from GNSS time series (Bock and Melgar, 2016; Santamaría-Gómez et al., 2013). Systematic errors expressed at similar time scales also contribute to periodic variation that can affect the uncertainty of the site velocity.

Observations of geophysical signals from GNSS may also be biased through errors in the realisation of the Earth's reference frame, and more specifically the centre of mass and/or scale (Wu et al., 2011; Wu et al., 2012). The theoretical origin of the current internationally recognised reference frame is the centre of mass of Earth, (Altamimi et al., 2016), and is the point around which all geocentric Earth satellites orbit (Wu et al., 2012). The motion of the centre of mass of the solid Earth system is sensitive to contributions from changing ice sheets and their interiors, continental water storage including surface water and groundwater, crustal dynamics, the atmosphere, and the oceans (Figure 1.1). These features and processes also influence site positions. Since the origin of the ITRF is defined as the long-term mean centre of mass (Altamimi et al., 2016), geocentre motion will be absorbed into station coordinates and velocities, primarily in the height component (Appleby et al., 2016). Precise positioning on the surface of the Earth depends on the reliability of the reference frame where false or geophysically un-modelled geocentre motions will influence the accuracy of downstream products such as site positions and velocities. This thesis analyses the non-linear motion of the Earths centre of mass observed by Satellite Laser Ranging (SLR) and the expression of the resulting uncertainty at the surface.

Having an improved knowledge of uncertainty of the geocentre provides greater confidence in Chapters 3 and 4 to interpret geophysical signal and further separate

it from more local and regional sources of noise. To assist in the understanding of geodetic observations of vertical land motion in Australia, this thesis first explores reference frame error, noise, and the contributing geophysical processes. The importance of the centre of mass definition of the ITRF is explored together with how it relates to observations of vertical land motion. Key limitations arising from assuming that the noise processes associated with time series are simplistic in nature are investigated. Observations of time dependent deformations of the Earth's surface are inherently reliant on the stability and accuracy of the underlying reference frame, which is sensitive to the definition of the Centre of Mass, as well as the geophysical processes of other surface deformations that are included in the data processing steps. Geodetic techniques can provide observations of vertical land motions at the millimetre-scale, but the interpretation and data reduction techniques currently used are prone to simplification, which can lead to erroneous geophysical interpretation. This body of work aims to refine the estimates of vertical land motion across the Australian continent by investigating geophysical drivers of surface deformation and systematic errors in their expression in geodetic time series.

1.2 Australian context

The Indo-Australian Plate moves approximately 7 cm/yr towards the northeast. This motion is well-constrained by geodetic measurements from GNSS, Very Long Baseline Interferometry (VLBI) and SLR (Altamimi et al., 2012; Argus and Heflin, 1995; Tregoning et al., 2013). The Indo-Australian Plate is considered to be one of the most internally stable crustal plates (excluding the south-east region), with a recent study showing that a large portion of the plate is deforming horizontally at less than 0.2 mm/yr (Tregoning et al., 2013). In contrast, the present-day vertical velocity of the Australian crustal plate is not well understood and inconsistent with modelled estimates of vertical motion. Although the Australian continent is in the middle of the Indo-Australian tectonic plate and has previously been considered seismically inert, small magnitude intraplate events suggest that neo-tectonic regional seismic deformation and large events at the plate boundaries cause stress field changes. These intraplate events may appear as non-linear deformation signals in GNSS time series, and these have yet to be comprehensively studied using state-of-the-art analysis approaches.

Contemporary crustal stress fields are primarily controlled by broad-scale tectonic forces (Rajabi et al., 2017). The Indo-Australian Plate has complex plate boundary and internal mechanisms, where stress and strain build up from compression at the plate edges causes faults to rearrange to relieve the accumulated strain towards the centre of the plate. Examples of such strain release can be expressed in the form of intraplate earthquakes. Although the occurrence of 'moderate-large' ($>M_W$ 5.0) earthquakes are infrequent in Australia, there is still a record of events that have caused surface ruptures, listed in Table 1.1. Geodetic studies are not available for most of

these events (many of which predate the GPS). Although they have been studied using seismology, their small size and remote location with respect to Australian population centres means they are not always well observed. Large intraplate earthquakes, although rare, do occur within the Australian continent (Clark et al., 2014). Low resolution GNSS networks and the infrequency of these earthquakes puts them out of the scope of this thesis.

TABLE 1.1: Australian intraplate earthquakes with magnitude (M_W) greater than 5.0 that have caused surface ruptures over the period 1698 to 2019. NB: magnitudes are as reported by Geoscience Australia following an international effort to revise historic earthquake magnitudes in 2016.

Earthquake	Date	Magnitude (M_W)	Reference
Meckering, Western Australia	14 Oct 1968	6.5	(Gordon and Lewis, 1980)
Calingiri, Western Australia	11 Mar 1970	6.0	(Gordon and Lewis, 1980)
Cadoux, Western Australia	29 Jun 1979	6.1	(Denham et al., 1987)
Marryat Creek, South Australia	30 Mar 1986	5.7	(Crone et al., 1997; Machette et al., 1993; McCue et al., 1987)
Tennant Creek (series), Northern Territory	22 Jan 1988	6.2-6.6	(Bowman et al., 1990; Crone et al., 1992; Crone et al., 1997)
Newcastle, New South Wales	28 Dec 1989	5.4	(McCue et al., 1990)
Petermann Ranges, Northern Territory	21 May 2016	6.1	(Hejrani and Tkalčić, 2019; Polcari et al., 2018; Thom, 2017)

The AuScope Geospatial program was funded by the Australian Government to, in part, develop a new network of approximately 120 GNSS continuously operating reference stations to monitor crustal deformation, established under the National Collaboration Research Infrastructure Strategy. These sites have been installed across the Australian continent, as shown in Figure 1.2, since 2007 with each site consisting of a reinforced concrete pillar monument, geodetic choke ring antenna and multi-frequency code and carrier phase tracking receiver. Most of the sites were built, installed and collecting reliable data by 2015. This substantially densified the existing network in Australia and the South Pacific of about 20 sites. This large network is now of an age (more than 3 years) where horizontal and vertical site velocities can be reliably estimated from the continuous time series (e.g. Blewitt and Lavallée, 2002; Bos et al., 2010). The new AuScope network presents a unique opportunity to reassess regional and continental-scale surface deformation using advanced analysis approaches and a relatively dense spatial network of new data.

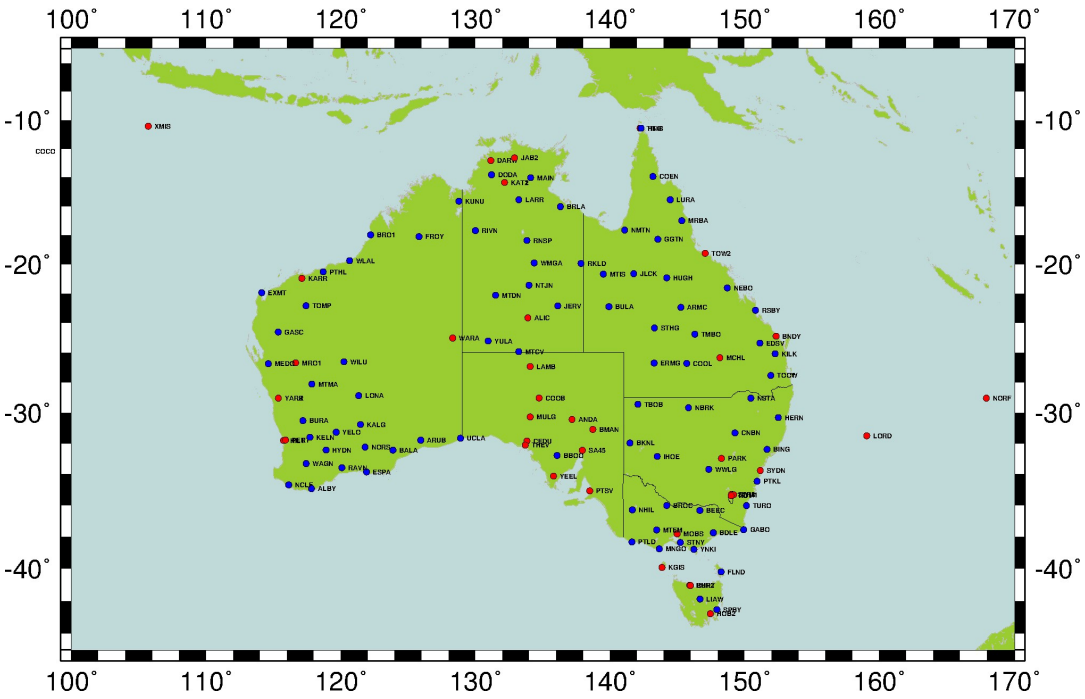

FIGURE 1.2: Australian AuScope GNSS network, including stations from the Australian Regional GNSS Network (ARGN, shown in red).

1.3 Research motivation and knowledge gap

In industries such as mining, maritime, transport, construction and agriculture, the use of precise positioning and location enabled services is growing rapidly, and there has been a significant increase in the use of positioning across society. Position and navigation information is now routinely used for emergency service responses, hazard modelling and land, utility and asset management where the need for accurate and reliable geodetic infrastructure and position and velocity products is paramount. A clear understanding of the inherent uncertainty is critical to ensure that the frame of reference meets user's needs, including the quality and integrity of the contributing geodetic data.

Scientific studies also depend on accurate and precise understanding of the vertical movement of Australia and its causes. Many studies that focus on vertical land motion at regional or continental scales tend to focus on land motion at coastal sites which has the obvious application to the determination of relative and absolute sea level. One of the primary factors that causes local sea level to differ from the global average is vertical land motion (King et al., 2012; Pfeffer et al., 2017). Existing sea level studies in the Australian region have only used a small number of GNSS sites. Four sites were used by King et al., 2012 to investigate vertical land motion at tide gauge stations; 12 sites were used in Burgette et al., 2013 and White et al., 2014, with a focus on GPS sites near Australian tide gauges; 13 sites were used by Santamaría-Gómez et al., 2012, again with a focus on GNSS sites located near the coast; and 36 Australian sites were used in Altamimi et al., 2016 for the realisation of ITRF2014.

The maturation of the AuScope network to $\sim$ 120 sites provides the opportunity for new research of crustal deformation of the Australian continent, capitalising on the availability of longer time series and better spatial coverage.

GPS observations from previous research indicates that the vertical motion of the Australian continent at a dozen permanent sites is between 0 and -1 mm/yr (Altamimi et al., 2016; Burgette et al., 2013; King et al., 2012; Santamaría-Gómez et al., 2012). Across Australia, recent model predictions of ongoing surface deformation due to GIA (the response of the solid Earth to past ice-ocean load changes), are ambiguous as to the sign of vertical land motion, although predictions have values of less than $\pm$0.5 mm/yr over the Australian landmass. GIA only represents one component of the signal of the vertical land motion, but is commonly the only signal that is considered in predictions of regional and coastal sea level change (Church et al., 2013). Neglecting non-GIA related sources of vertical land motion is likely to bias interpretation of sea level projections in some areas (Dangendorf et al., 2017; Han et al., 2015).

Over recent decades GNSS time series have been used to quantify the crustal deformation of the surface of the Earth in the horizontal direction due to postseismic relaxation, including Australia. However, there have not been any studies on the extent of Australian vertical land motion as a result of postseismic deformation. Tregoning et al. (2013) focused on observations and modelling of horizontal postseismic deformation due to 'Great Earthquakes' ($>M_W$ 8.0) using GPS data over the period 2000.0-2011.0. The presence of ongoing postseismic relaxation after Great Earthquakes thousands of kilometres from plate boundaries has significant ramifications for interpretations of regional surface deformation. Detection of far-field postseismic deformation from Great Earthquakes is possible in the horizontal component (e.g. King and Santamaría-Gómez, 2016; Kreemer et al., 2006; Watson et al., 2010) and is a fundamental requirement for the production of an accurate and stable global reference frame. The detection of vertical deformation from far-field postseismic earthquakes also has ramifications for the accuracy and stability of the global reference frame and GIA models of postglacial rebound.

Measurement of vertical land motion from GPS directly relies on the accurate determination of the centre of mass of the earth, as defined by the reference frame. The comparison of vertical land motion observed by GPS with values from GIA models could be biased by postseismic deformation over temporal scales from years to decades, and also complicated by shorter period signal due to surface loading changes that add noise to shorter GPS records. In the realisation of the current ITRF, the assumption remains that the centre of mass motion is linear and subject to a white noise process. An alternative model of non-linear and temporally correlated motion is presented in this thesis.

1.4 Thesis research questions and objectives

1.4.1 Research questions

Several questions remain when interpreting geodetic time series of surface displacement which are relevant to understanding the long-term (decadal to millennial) vertical displacement of Australia: To what extent can geodetic time series represent displacements beyond their data span? What is the appropriate model for this motion? How do short-period displacements or noise affect the ability to robustly estimate the model parameters? What is the characteristic of the noise in the context of the adopted model? Is the underlying geodetic reference frame sufficiently accurate to allow measurement at the accuracy required?

This thesis starts global in its focus, by investigating the global reference frame, before moving to study the Australian domain in greater detail. In this thesis, the following specific research questions (RQs) are addressed:

RQ1) What is the nature of the uncertainty in the centre of the mass of the Earth and how does this relate to GPS position estimates?

Characterising noise processes in the geocentre time series will allow better determination of the uncertainty in the centre of mass of the Earth as used in the current realisation of the International Terrestrial Reference Frame (ITRF2014). Geocentre motion as measured by Satellite Laser Ranging (SLR) is compared with geocentre motion from numerical surface mass loading models to characterise the noise parameters. Chapter 2 addresses RQ1, as shown in Figure 1.3, and examines how we can observe and model the centre of the Earth's mass in the context of ITRF2014. The work described therein quantifies uncertainties for linear geocentre motion with the existence of temporally correlated noise, where traditionally, only a white noise process has been considered. Chapter 2 explores the modelled motion of the geocentre with linear terms for the annual and semi-annual signals, but also considers temporally correlated coloured noise processes to account for non-linear geocentre motion.

RQ2) To what level is vertical land motion across Australia spatially coherent, over what timescales, and what are the dominant driving mechanisms?

The discrepancy between the expected long-term solid-earth deformation from glacial isostatic adjustment and present-day observations has not yet been resolved for the Australian region. Chapter 3 seeks to answer RQ2 where there is a perceived divergence between present-day observations and predicted land motion from a range of processes. Using advanced GPS analysis techniques, spatiotemporal filtering and multivariate regression, the differences between the models and observations are investigated. The research presented in Chapter 3 uses the full AuScope

Australian GNSS network (∼120 sites) that covers the full continental scale to determine if land motion across Australia is spatially coherent and whether the driving mechanisms of the vertical motion can be further understood. Vertical land motion from GNSS stations in Australia is compared with geophysical models (e.g. glacial isostatic adjustment and hydrological surface mass loading from the Gravity Recovery And Climate Experiment mission) to assess the spatial coherence and improve the accuracy of the velocity field across Australia. Due to improvements in the modelling and measurement of different contributions towards surface mass transport, GPS velocities are then compared with a range of GIA models.

RQ3) What is the magnitude, extent and duration of plausible far-field postseismic deformation in the vertical direction across the Indo-Australian Plate from large plate boundary earthquakes?

Coseismic and postseismic deformation represent one of many drivers of spatially coherent vertical land motion investigated in the previous research question. This requires further detailed investigation and, in Chapter 4, both coseismic and postseismic non-linear deformation of the Australian continent from large boundary events are observed in GPS time series and compared with modelled postseismic viscoelastic solid-earth deformation. The time series from Chapter 3 are used to continue the investigation into the reduction of noise and uncertainty in GPS position and velocity estimates in Chapter 4. Coseismic offsets and postseismic deformation are modelled using elastic and viscoelastic parameters, the latter with a range of one-dimensional Earth models with varying layered rheological structure. Vertical and horizontal GPS daily time series are used to assess the predicted surface deformation to select the best-fit Earth model properties that describes the crustal thickness and viscosity. Chapter 4 further explores if present-day deformation is potentially still underway at non-negligible levels due to an historic event that occurred before the modern satellite geodesy era.

1.4.2 Research objectives

By addressing the stated research questions, this thesis first seeks to understand temporally correlated noise and uncertainty in the reference frame as is required to robustly measure vertical land movement using geodetic techniques, and then seeks to understand vertical motion of the Australian continent using GPS observations and geophysical models of solid-earth deformation to determine dominant driving mechanisms and spatial coherence. Noting the above research questions, this thesis has the following research objectives:

1. Characterise the noise processes in the SLR geocentre time series to better determine the uncertainty in the centre of mass of the Earth as used in the current realisation of the International Terrestrial Reference Frame (ITRF2014).

   (a) Investigate the occurrence of coloured noise in the geocentre time series as observed by SLR.

   (b) Compare geocentre motion as measured by SLR with geocentre motion from surface mass loading models.

2. Consistently process the entire Australian AuScope GNSS network of 120 sites with advanced precise point processing techniques, producing a database of time series that are robust.

3. Develop a spatiotemporal model of vertical land motion in Australia from GNSS stations for comparison with global and regional geophysical models (e.g. GIA ICE-6G model, hydrological surface mass loading from GRACE).

   (a) Spatiotemporal analysis (such as empirical orthogonal functions) will be used to decompose GPS time series to determine the dominant modes of deformation that are expressed in vertical land motion time series across Australia.

   (b) Simultaneously estimate temporally correlated noise models to determine an Australian vertical velocity field using multivariate regression.

4. Model coseismic and postseismic deformation of the Indo-Australian Plate after the occurrence of large earthquakes and compare with GPS observations.

   (a) Conduct modelling of large plate boundary earthquakes in the Australian region with elastic and viscoelastic earth models.

   (b) Compare observed crustal deformation from GPS with the modelled deformation.

   (c) Investigate if Australia experiences ongoing deformation due to historic earthquake events that occurred prior to the geodetic record.

1.5 Thesis structure

The research questions are related to each chapter as shown in Figure 1.3.

The Introduction (Chapter 1) has provided an overview of the setting in which this research sits, providing both a global and regional context, by identifying the knowledge gap and research questions to be addressed.

Chapter 2 addresses RQ1 and looks at how we can observe and model the centre of the Earth's mass in the context of the ITRF2014 and how the stochastic and functional models of the realisation of the reference frame could be improved by considering the existence of coloured noise, where traditionally, only a white noise process is considered. Chapter 2 has been published as Riddell et al. (2017) *Uncertainty in*

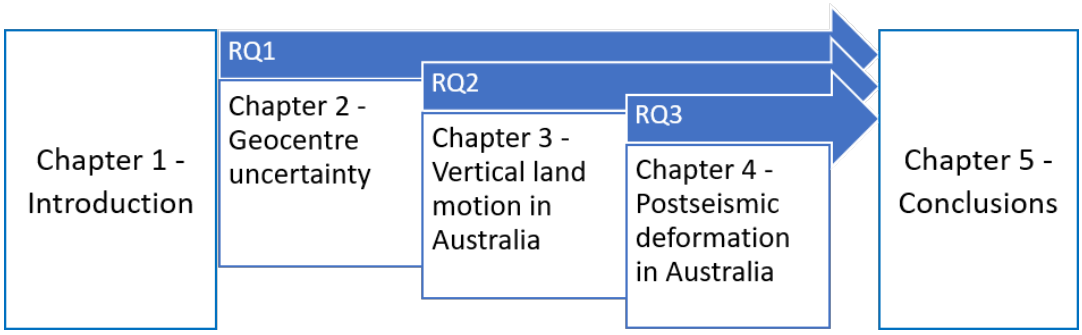

FIGURE 1.3: Thesis structure and link between chapters and research questions

geocenter estimates in the context of ITRF2014. Journal of Geophysical Research: Solid Earth (122).

Chapter 3 seeks to answer RQ2 where a discrepancy between present-day observations and models of land motion in Australia is identified. Using advanced GPS analysis techniques and spatiotemporal filtering, the differences between the models and observations are explored. Chapter 3 has been published as Riddell et al. (2020) *Present-day vertical land motion of Australia from GPS observations and geophysical models*. Journal of Geophysical Research: Solid Earth (125).

Chapter 4 focuses on RQ3 where non-linear postseismic deformation of the Australian continent from intraplate and large boundary events are observed and then modelled and compared with solid-earth deformation signals. The GPS time series from Chapter 3 are used as inputs. Chapter 4 has been submitted to Geophysical Journal International as Riddell et al. (2020) *Ongoing postseismic vertical deformation of the Australian continent from far-field earthquakes*.

Concluding remarks identifying the significance of the findings, the broader context of the results, and suggestions for future research are in Chapter 5.

The Appendices contain supporting information for each of the chapters, a list of oral and poster presentations, professional development opportunities, as well as public outreach and engagement activities undertaken during the course of this PhD.

Chapter 2

Uncertainty in geocentre estimates in the context of ITRF2014

Summary

Uncertainty in the geocentre position and its subsequent motion affects positioning estimates on the surface of the Earth and downstream products such as site velocities, particularly the vertical component. The current version of the International Terrestrial Reference Frame, ITRF2014, derives its origin as the long-term averaged centre of mass as sensed by Satellite Laser Ranging (SLR), and by definition, it adopts only linear motion of the origin with uncertainty determined using a white noise process. We compare weekly SLR translations relative to the ITRF2014 origin, with network translations estimated from station displacements from surface mass transport models. We find that the proportion of variance explained in SLR translations by the model-derived translations is on average less than 10%. Time-correlated noise and non-linear rates, particularly evident in the Y and Z components of the SLR translations with respect to the ITRF2014 origin, are not fully replicated by the model-derived translations. This suggests that translation-related uncertainties are underestimated when a white noise model is adopted, and that substantial systematic errors remain in the data defining the ITRF origin. When using a white noise model, we find uncertainties in the rate of SLR X, Y and Z translations of $\pm$0.03, $\pm$0.03 and $\pm$0.06 respectively, increasing to $\pm$0.13, $\pm$0.17 and $\pm$0.33 (mm/yr, one sigma) when a Power Law and White (PLW) noise model is adopted.

This chapter has been published as: Riddell, A. R., King, M. A., Watson, C. S., Sun, Y., Riva, R. E. M. & Rietbroek, R. 2017. Uncertainty in geocenter estimates in the context of ITRF2014. Journal of Geophysical Research: Solid Earth, 122, pp. 4020-4032. Minor changes have been made to the original published article for consistency in this thesis. This includes general terminology and grammar.

2.1 Introduction

The need to monitor global change processes, such as sea-level change and post-glacial rebound, at a level below 1 mm per year illustrates the requirement for an accurate and precise global geodetic reference frame. The International Terrestrial Reference Frame (ITRF) (Altamimi et al., 2016) attempts to meet accuracy and stability goals of 1 mm and 0.1 mm/yr respectively (Gross et al., 2009). As each iteration of the ITRF provides improvements in the precision and accuracy of the global reference frame, challenges remain to meet the accuracy and stability goals. Particularly challenging is the realisation of the origin (defined as the long-term averaged centre of mass of the Earth), and its evolution in time (Dong et al., 2014). Presently, this realisation is limited given it is determined using measurements from a single measurement technique [Satellite Laser Ranging (SLR), Altamimi et al. (2016) and Wu et al. (2011)] that is known to be affected by systematic biases and network asymmetry (Appleby et al., 2016). The ITRF2014 (and each predecessor) is a linear frame by definition, and consequently the long-term motion of its origin is described by a linear trend. Limitations arise given that when specifying the ITRF origin to coincide with the long-term origin of the SLR frame, only time-constant annual and semi-annual terms are included with a white noise model (Altamimi et al., 2007; Altamimi et al., 2011; Altamimi et al., 2016; Argus, 2012), neglecting any other non-linear motions as part of the functional or stochastic model.

Relative motion between the Centre of Mass of the total Earth system (CM) and the Centre of surface Figure (CF) of the solid Earth can be observed using space geodetic observations that tie Earth-fixed permanent geodetic sites and space-based satellite platforms. Both secular and seasonal geocentre motion occurs as a result of past and present mass re-distribution, where geocentre motion is the difference between CM and CF (the difference between geophysically determined origins). Past mass redistribution on the surface or interior such as glacial isostatic adjustment (GIA), induces secular geocentre motion, while intra-annual, seasonal and inter-annual signals relate to present day distributions, such as exchanges within and between the ocean, atmosphere, continents and cryosphere (Argus, 2012; Dong et al., 1997; Wu et al., 2012). SLR translations with respect to the ITRF2014 origin therefore consist of both measurement error and a component of real geocentre motion affected by the non-homogenous network distribution of SLR tracking stations. This leads to a sampling bias known as the "network effect", and should ideally reflect the offset between the network origin (CN) and the CM rather than the geocentre motion.

An alternative approach to studying geocentre motion uses observations and numerical models of surface mass transport to derive deformation of the solid Earth at the locations of the SLR stations (that change over time), from which network translations may be estimated. The mass transport models provide bounds on the network translations which are to be expected from known surface loading processes.

Any inconsistency between observed SLR translations and those derived from a surface loading model will hint at problems in either the SLR methods (observations or processing) or problems within the surface loading model. In this Chapter, SLR translations and output from two surface loading models are used to assess the uncertainty in the SLR translations with respect to the ITRF2014 long-term origin.

2.2 Data

The origin of ITRF2014 is defined such that there are zero translation parameters and rates at epoch 2010.0 between the International Laser Ranging Service (ILRS) long-term mean origin from SLR and ITRF2014 (Altamimi et al., 2016). The SLR temporal translation components used here have been derived with respect to the ITRF2014 origin that has been defined using the internal constraint method described in Altamimi et al. (2007) and Altamimi et al. (2016). The translations were estimated using a 7-parameter similarity transformation between each week and a SLR ITRF2014 network of 21 core stations. The time series of the 7-parameters were adjusted globally, in one run using the CATREF software [Combination and Analysis of Terrestrial Reference Frames, e.g. Altamimi et al. (2016)], with the full variance-covariance information of the total SLR SINEX time series. We analyse the translations from weekly combined SLR solutions relative to the ITRF2014 (linear) origin over the time span 1993.0 to 2015.0 in the temporal and spectral domains. The complete ILRS SLR reference frame solutions in SINEX format submitted for the realisation of ITRF2014 covers the time span 1983.0 to 2015.0. Only the data from 1993.0 on-wards are used here due to noisy data in the early section of the time series, producing large formal uncertainties in the SLR translation series before the LAGEOS-2 satellite was launched in 1992 (Dong et al., 2014). We compare the SLR translation time series with respect to the ITRF2014 long-term origin with two different estimates of network translations that are derived from independent surface mass transport models.

The ITRF2014 origin is considered theoretically representative of the long-term CM, where geocentre motion is defined as motion of the CM with respect to the CF (Altamimi et al., 2016). Linear motions for ground stations are assumed, with some discontinuities and post-seismic deformations enforced for sites affected by major earthquakes or equipment changes. The ITRF origin reflects CM on secular time scales due to it coinciding with the long-term average CM as observed by SLR, but on shorter (including seasonal) time scales, the ITRF origin reflects CF (Blewitt, 2003; Collilieux et al., 2009; Dong et al., 2003). We note that some of the literature considers the opposite convention, that is, displacement of CF with respect to CM, for example Métivier et al. (2010) and Dong et al. (2014).

Our first comparative geophysical model is from Rietbroek (2015), who calculated surface mass transport loading based on a combination of Gravity Recovery and Climate Experiment (GRACE) and radar altimetry data using an inversion approach

that applied conservation of mass to solve the sea level equation (Rietbroek et al., 2016). Surface displacement components are provided for the time span 2002.3 to 2014.5 with monthly sampling, here-on referred to as R15. R15 considers mass redistribution from the Antarctic and Greenland ice sheets, land glaciers, GIA, continental water storage, and contributions from the oceans and atmosphere. Although GRACE alone is not capable of observing degree-1 mass redistribution, combination with additional datasets and use of an inversion methodology enables derivation of surface mass transport values. The short data span is limiting given it covers only half of the SLR series, but remains useful given the independent GRACE-based approach.

Our second dataset was estimated from numerical surface mass transport models and solves the sea level equation to conserve mass for the global system after taking into account self-attraction and loading effects (Gordeev et al., 1977; Frederikse et al., 2016; Tamisiea et al., 2010) using fingerprints (Mitrovica et al., 2001) to represent the non-uniform redistribution of water. Here-on this mass surface model product is referred to as MSM. MSM yields values over the time span 1993.0 to 2015.0 with monthly sampling. This dataset includes modelled ocean and atmosphere mass redistribution (defined using the AOD1B product) (Flechtner et al., 2015), continental land glaciers (Marzeion et al., 2015), Greenland (van den Broeke et al., 2016) and Antarctic ice sheet surface mass balance changes from the Regional Atmospheric Climate Model (RACMO) version 2.3 (Noël et al., 2015), Global Reservoir and Dam database (GRanD) dam water retention (Lehner et al., 2011) using the filling rate method of Chao et al. (2008) and other terrestrial water storage from the Noah Global Land Data Assimilation System (GLDAS) product (Rodell et al., 2004).

Both the land glacier and dam retention components are sampled annually and have been linearly interpolated to monthly intervals for consistency with the other datasets, constraining the temporal resolution. It would be expected for these components to contain annual signals due to the seasonal nature of hydrologic mass exchange, and we return to this in the Discussion. A groundwater component is available using data from Wada et al. (2010). The contribution from groundwater to the overall signal is primarily linear with very small annual amplitude for the available period. Further data description for MSM is available in Appendix A and Frederikse et al. (2016), including uncertainties for the component contributions.

Surface displacements from each geophysical model were derived by redistributing loaded masses within a thin shell on the Earth's surface. They are spherically symmetric, stratified, and non-rotating Earth responses elastically redistributed over sub-secular (sub-daily to decadal) time scales. The displacements are proportional to the incremental load potential according to the load Love number theory (Farrell, 1972), and are derived from the elastic Preliminary Reference Earth Model (PREM) (Dziewonski and Anderson, 1981).

Following the methodology of Collilieux et al. (2009), network translations have been derived from station displacements due to loading effects from two distinct surface mass transport models and compared with SLR translations with respect to the ITRF2014 long-term origin to account for the network effect of the SLR station geometry.

From each of the geophysical models, network translations are computed following the methodology of Collilieux et al. (2009), using the ITRF2014 station positions and velocities plus the modelled surface mass loading deformation at each epoch of the respective dataset. At each epoch, we used only those SLR sites that were active. The monthly surface deformation values are interpolated from monthly to weekly values using a cubic spline. The two synthetic time series are then used to estimate transformation parameters, using Globk (Herring et al., 2015), with respect to ITRF2014 using the full covariance matrix of the ILRS combined solution submitted for ITRF2014 analysis. Following Collilieux et al. (2012), only three rotations and three translations were estimated (that is, scale was not estimated). Repeating the analysis with the scale parameter included produced only negligible changes to the estimated transformation parameters. Covariance information was used as given; an occasional site was automatically removed for a given week due to the estimated station adjustments being larger than 10-sigma. Given that the ILRS combined solution was generated using a loose constraint approach correlations exist between the Helmert parameters, some of the station displacements may leak into the rotation parameters (Collilieux et al., 2009). Here, the rotations have a mean and standard deviation of 0.00 ± 0.02 mas for all components from both models (one sigma), which induces station displacements below 1 mm.

The two network translation models, R15 and MSM are compared with the SLR translation components with respect to the ITRF2014 origin to assess the sensitivity of the SLR observed origin against geophysically modelled geocentre motion taking into account the network effect of the SLR observing network.

2.3 Comparison of SLR and modelled network translations

By construction, there are zero translation rates (trends) between ITRF2014 and the SLR stacked frame of weekly solutions over the time span 1993.0 to 2015.0. Annual and semi-annual periodic signals were not removed from the SLR translation components as these are signals of interest. Figure 2.1 (left) shows the three datasets in the temporal domain sampled at monthly epochs for clarity. The surface deformation values at each site were detrended before transformation (Collilieux et al., 2009). Formal errors are not available for either of the surface mass transport models, but uncertainties are available for the constituent datasets that contribute to each

model. Further information on the model uncertainties can be found in the associated references. Our use of two geophysical models aims to reflect, at least partly, the uncertainty in the two models.

Figure 2.1 (right) shows the SLR translations alongside the differences of R15 and MSM with SLR, where the qualitative agreement of the curves reveal that the differences are heavily influenced by signal not in R15 and MSM. Considering the residual series, the percentage of SLR variance explained by R15 is 12.5%, 1.3% and 2.1% for the X, Y, Z components, respectively, with MSM explaining 8.1%, 4.0% and 2.0%, respectively. The small proportion of variance explained by the surface mass transport models indicates that either the geophysical models are not able to capture the surface mass transport variability and/or systematic errors from the SLR technique are substantial. The visual agreement between R15 and MSM is noteworthy given the dissimilarity in the data used to construct the series. Surface thermoelastic effects, with annual amplitudes approaching 3 mm for radial displacements and 1.5 mm for transverse displacements (Xu et al., 2017), could explain some of the difference between the SLR translations and the respective network translations.

2.3.1 Seasonal variation

The dominant signal throughout the SLR translation series has an annual period with apparent variable amplitude. Over the full time series, the SLR translation annual signal in the Z component is approximately twice that of the SLR translation X and Y components (see Table 2.1). The greatest agreement in overall amplitude and its temporal variation between SLR, R15 and MSM is found in the X component, which is predominantly ocean-driven due to the limited land area along the X axis (X is in the direction of 0° N 0° E, Y of 0° N 90° E, and Z of 90° N).

The annual signal expressed in the residuals for each coordinate component (Figure 2.1d, e, f, SLR minus model) computed between the SLR origin and model based network translation estimates, demonstrate reasonable qualitative agreement in phase and amplitude, again demonstrating that both the R15 and MSM models significantly underestimate the amplitude of the annual signal within the SLR translations. To explore the strength of the annual signals more closely we computed the Power Spectral Density (PSD) using the Lomb-Scargle approach described by Press et al. (1992). Figure 2.2 shows the PSD for each dataset across each coordinate component. Lower frequency trends are less well resolved by R15 due to the restricted temporal span, and care should be taken not to over-interpret differences at these frequencies.

The annual signal expressed in MSM significantly underestimates the observed SLR amplitude in all components, particularly during the latter part of the Y component time series (Figure 2.1b) and remains visible as a peak in the residual PSD (Figure 2.2e). The shorter duration R15 model also underestimates the magnitude of the

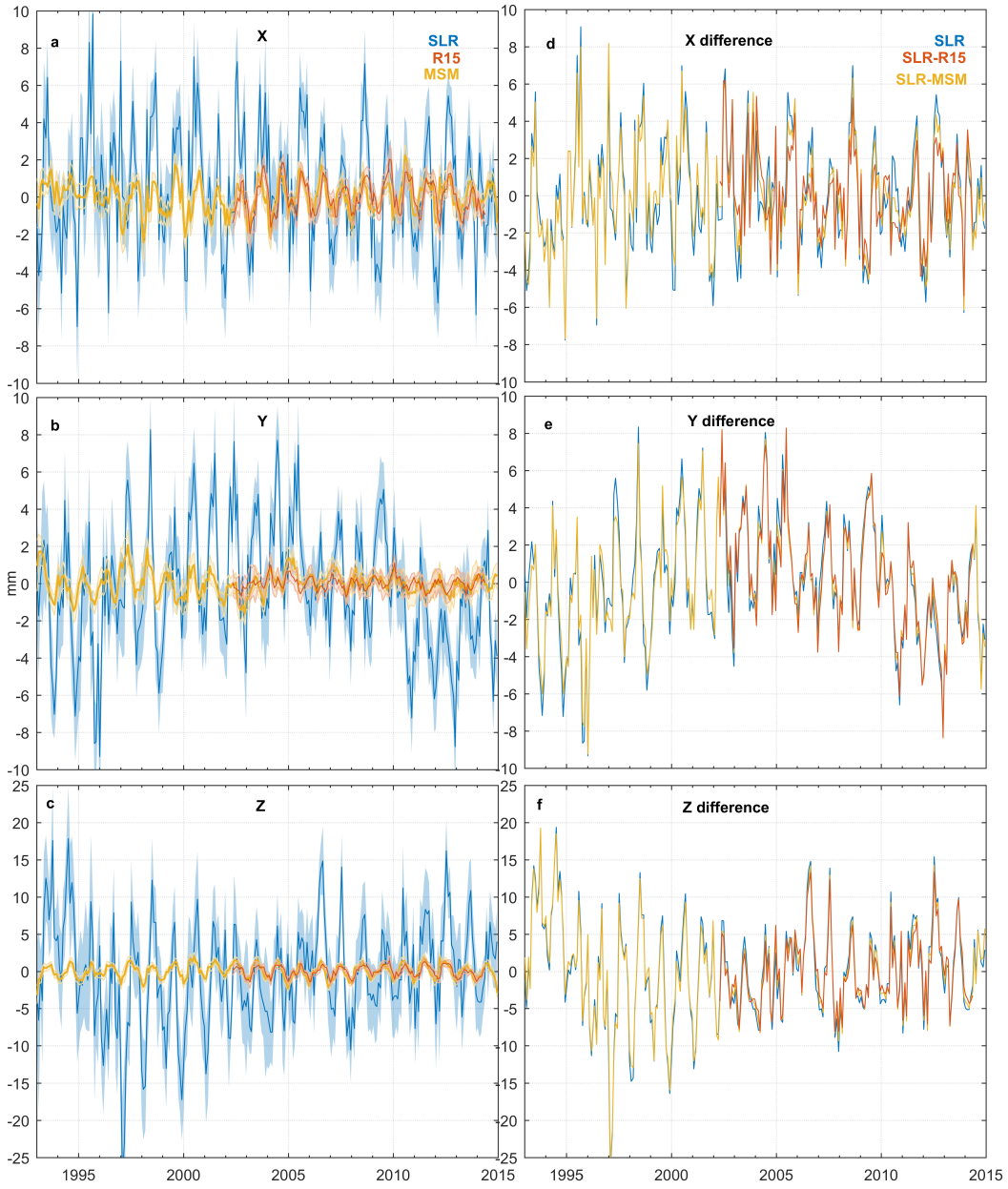

FIGURE 2.1: SLR translation components and two mass transport models (R15 and MSM). (a–c) Monthly translation series from SLR [1993.0–2015.0], R15 [2002.3–2014.5], and MSM [1993.0–2015.0] for each component (X, Y, and Z); the shaded area is transformation uncertainty. (d–f) SLR and differences of detrended monthly network translation time series for each component where the models have been subtracted from the SLR time series. Note the differences in scale of the Z component plots (Figures 2.1c and f) versus the X and Y components (Figures 2.1a, b, d, and e).

TABLE 2.1: Noise parameters from Hector of the full SLR data set and MSM network translation model [1993.0 2015.0][a]

	X								
	SLR			MSM			SLR-MSM		
model	white-only	PLW	GGM	white-only	PLW	GGM	white-only	PLW	GGM
AIC	1323.350	1282.103	1256.500	438.639	393.762	392.735	1225.414	1204.903	1198.35
BIC	1323.350	1289.263	1263.659	438.639	400.921	399.894	1225.414	1212.062	1205.51
k	0	-0.80	0.98 ± 0.30	0	-0.59	0.62 ± 0.30	0	-0.50	0.47 ± 0.18
1-phi			0.51 ± 0.14			0.02 ± 0.03			0.36 ± 0.19
STD	2.939	2.689	2.570	0.504	0.5041	0.554	2.443	2.3301	2.303
bias (mm)	-0.000 ± 0.181	-0.197 ± 2.123	-0.014 ± 0.306	0.005 ± 0.034	0.042 ± 0.173	0.025 ± 0.098	0.001 ± 0.150	-0.102 ± 0.602	-0.003 ± 0.229
trend (mm/yr)	-0.000 ± 0.028	0.017 ± 0.128	0.000 ± 0.048	-0.001 ± 0.005	-0.009 ± 0.016	-0.007 ± 0.014	-0.005 ± 0.024	0.007 ± 0.061	-0.003 ± 0.036
	Y								
AIC	1371.096	1222.215	1192.371	401.992	243.008	225.826	1193.983	1060.86	1064.138
BIC	1371.096	1229.374	1199.531	401.992	250.167	232.986	1193.983	1068.019	1071.297
k	0	-0.98	0.98 ± 0.13	0	-0.98	0.77 ± 0.11	0	-0.94	0.36 ± 0.04
1-phi			0.29 ± 0.08			0.17 ± 0.08			0.01 ± 0.01
STD	3.216	2.391	2.275	0.517	0.3769	0.367	2.302	1.7056	1.786
bias (mm)	-0.000 ± 0.198	-0.451 ± 8.952	-0.024 ± 0.473	0.008 ± 0.032	0.085 ± 1.318	0.025 ± 0.088	0.001 ± 0.141	-0.374 ± 2.525	-0.218 ± 0.567
trend (mm/yr)	0.000 ± 0.031	-0.027 ± 0.166	-0.008 ± 0.073	0.000 ± 0.005	-0.007 ± 0.026	-0.002 ± 0.013	0.006 ± 0.022	0.003 ± 0.082	0.002 ± 0.069
	Z								
AIC	1761.462	1638.007	1585.610	367.806	318.881	316.801	1626.136	1512.313	1508.971
BIC	1761.462	1645.166	1592.769	367.806	326.04	323.96	1626.136	1519.473	1516.13
k	0	-0.93	1.48 ± 0.32	0	-0.66	0.37 ± 0.07	0	-0.86	0.49 ± 0.07
1-phi			0.48 ± 0.10			0.05 ± 0.06			0.05 ± 0.04
STD	6.717	5.252	4.777	0.484	0.4375	0.436	5.203	4.1494	4.135
bias (mm)	-0.000 ± 0.413	0.637 ± 9.503	0.017 ± 0.871	0.004 ± 0.030	-0.053 ± 0.191	-0.025 ± 0.078	0.010 ± 0.320	0.892 ± 4.456	0.284 ± 1.061
trend (mm/yr)	-0.000 ± 0.065	-0.044 ± 0.328	0.006 ± 0.135	0.003 ± 0.005	0.004 ± 0.015	0.003 ± 0.012	-0.014 ± 0.05	-0.077 ± 0.223	-0.026 ± 0.156

[a]AIC is a measure of the relative quality of statistical models for a given set of data; BIC is a criterion for model selection among finite set of models; the model with the lowest AIC/BIC value is preferred; k is the spectral index; 1 phi is a GGM parameter; STD is the standard deviation (units mm).

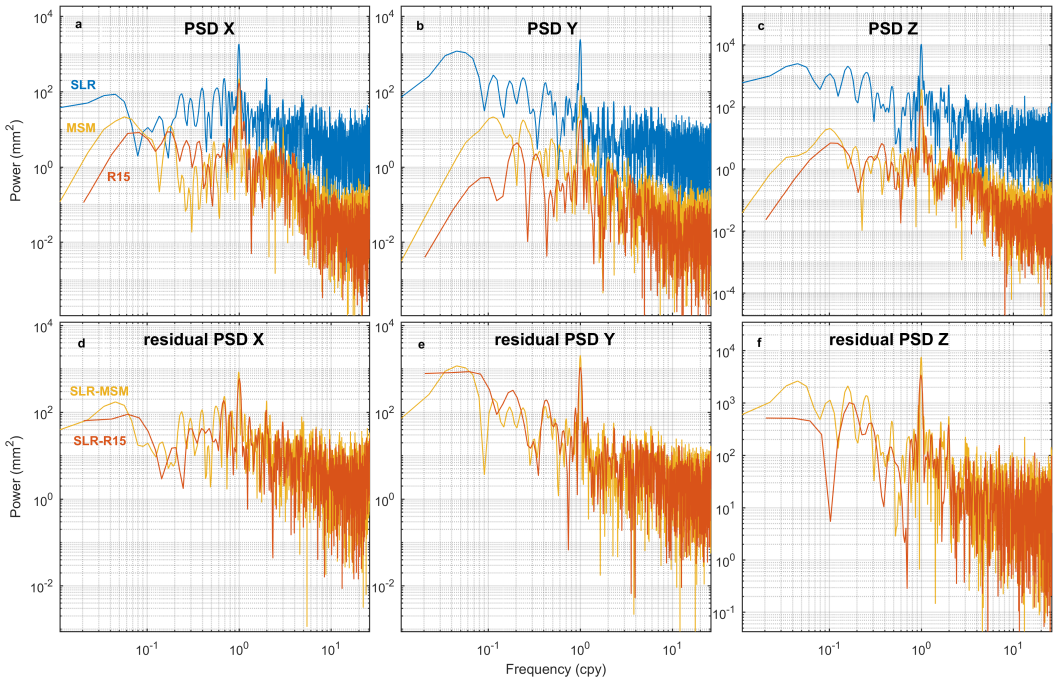

FIGURE 2.2: (a–c) PSD from Lomb-Scargle analysis of the data from SLR [1993.0–2015.0], R15 [2002.3–2014.5], and MSM [1993.0–2015.0], for each time series component (X, Y, and Z). (d–f) PSD of the residuals (data from Figures 2.1d–f) for each component. Note the differences in scale of the Z component plots (Figures 2.2c and f)versus the X and Y components (Figures 2.2a, b, d, and e).

annual signal, where the most notable differences for both R15 and MSM are with respect to the Z component (Figure 2.1c). This is confirmed by the presence of a residual peak at the one cycle per year frequency in the bottom panels of Figure 2.2.

The SLR series was compared with the MSM translations over the same time span as R15 (results not plotted here). In this analysis, the annual signal amplitude and phase of MSM were not statistically different from R15 in comparison to SLR over the shortened time span. The MSM dataset, over the R15 time span, is very similar to the SLR Y component, but has reduced agreement with the SLR X and Z components, particularly in the latter part (2002 onwards) of the time series (similarly as for R15) where the signal deviates (Figure 2.1). That the surface mass transport models are indistinguishable from each other in the later part of the time series provides confidence in their construction, noting again the dissimilarities in their constituent data series.

The magnitude-squared coherence of the SLR time series with each of the models in Figure 2.3, provides further evidence that an annual signal is clearly present in both the observations from SLR and the network translation estimates from geophysical models. A strong peak in each component is centred about one cycle per year, with an average magnitude-squared coherence of 0.9 across the X, Y and Z components.

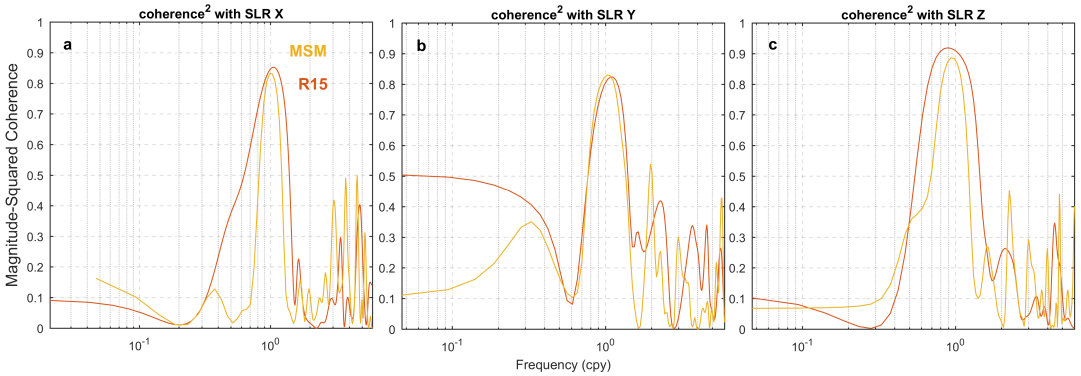

FIGURE 2.3: (a–c) Coherence-squared of SLR translation components with network translations from surface mass transport models (R15 and MSM).

Figure 2.3a shows agreement in the X component is poor for signals other than annual, particularly between SLR and R15. Better agreement at other frequencies is evident in the Y and Z components between SLR and the network translation models. Other less significant peaks are observed at sub-annual periods, but they are not considered further here.

To assess the time-variability of the time series, we follow a similar method to Argus (2012) whereby each time series is divided into four-year segments, each overlapping by one year, producing seven segments in our analysis. A linear plus seasonal model was fitted to each segment, with the amplitude for each origin component shown in Figure 2.4a, b, c, each centred on the mid-point of the segment. Four years is sufficient to reliably estimate the linear plus annual and semi-annual terms (Blewitt, 2003). For the SLR data, a number of annual amplitudes computed from segmented data are significantly different to those computed over the full series in the Y and Z components. While natural variation in these terms is expected, some of the behaviour appears systematic and specific to SLR. For example, the Y component shows a marked reduction in amplitude following the segment centred on 2003.5 (Figure 2.4b), which is not reflected in the R15 data, and only marginally reflected in the MSM data. The largest variability in SLR annual amplitude is found in the Z component (Figure 2.4c), with the large deviation in the segment centred on 1997.5 not reproduced by either R15 or MSM.

We also note a decrease in the uncertainty of the annual amplitude across the SLR data segments, most noticeably in the X and Z components. This perhaps reflects refinements in the SLR observing networks' geometry and operation capacity over time (Varghese, 2013).

2.3.2 Noise characteristics

Examination of Figure 2.2 shows clear features other than the dominant annual signals. The noise floor of the SLR dataset is substantially higher than that of both the

network translation models, presumably associated the effect of measurement error. The SLR X component (Figure 2.2a) shows a flatter (whiter) spectrum than in Y and Z indicating increased time-correlated noise in the latter components. The spectra of SLR-R15 and SLR-MSM (Figure 2.2 d, e, f) also suggests time-correlated noise across each component.

To further examine the properties of the time-correlated noise, we tested various noise models for each dataset using Hector software (Bos et al., 2013), examining white noise-only, random walk, flicker, autoregressive moving average, autoregressive fractionally integrated moving average, Generalised Gauss Markov (GGM) or Power Law and White (PLW) models. Noise model parameters and summary statistics were estimated along with a linear rate and annual plus semi-annual periodic terms. We used both the Akaike Information Criterion (Akaike, 1973) and Bayesian Information Criterion (Schwarz, 1978) to identify the preferred noise model for each time series. The characteristics of the SLR series are best fit by a GGM or PLW model, in strong preference to a white noise-only model (see Table 2.1). Where a white noise-only model was estimated in Hector, our values are consistent with the time constant annual and semi-annual terms of Altamimi et al. (2016).

The uncertainty in the rate of the SLR translations, estimated with a PLW noise model over the complete time span, is a factor of five larger in comparison to a white noise-only model (see Table 2.1). That is, white noise uncertainties for X, Y and Z rates respectively of $\pm$0.03, $\pm$0.03 and $\pm$0.06 increase to $\pm$0.13, $\pm$0.17 and $\pm$0.33 (mm/yr) when a PLW noise model is adopted. A PLW noise model was chosen instead of GGM for the remaining analysis as a conservative estimate of rate uncertainty. We examined the apparent offset around 2010 in the SLR origin Y component (Figure 2.1b, e), as described by Altamimi et al. (2016), and found it to be statistically insignificant when estimated as an offset within the noise analysis. Neither of the geophysical models show an offset at this time. Together, this suggests that the apparent discontinuity is simply characteristic of power law time-correlated noise with spectral indices close to -1 (flicker noise) (Williams, 2003a). No other offsets were estimated for the datasets. Neither of the network translations from the geophysical models capture the long period variability in the SLR series particularly well. The removal of the models from the SLR series results in generally no change to the spectral index for the PLW model in the X, Y and Z components for both MSM and R15, (see Table 2.1 and Table 2.2).

2.3.3 Time variable trends

We next consider the multi-year trends in the SLR translation time series. By convention, the linear rate of each SLR origin translation component are not statistically different from zero (Altamimi et al., 2016) over the full time series. However, low frequency variability is evident in the SLR time series, particularly in the Y and Z components (Figure 2.1b, c). This signal is not present in either of the mass transport

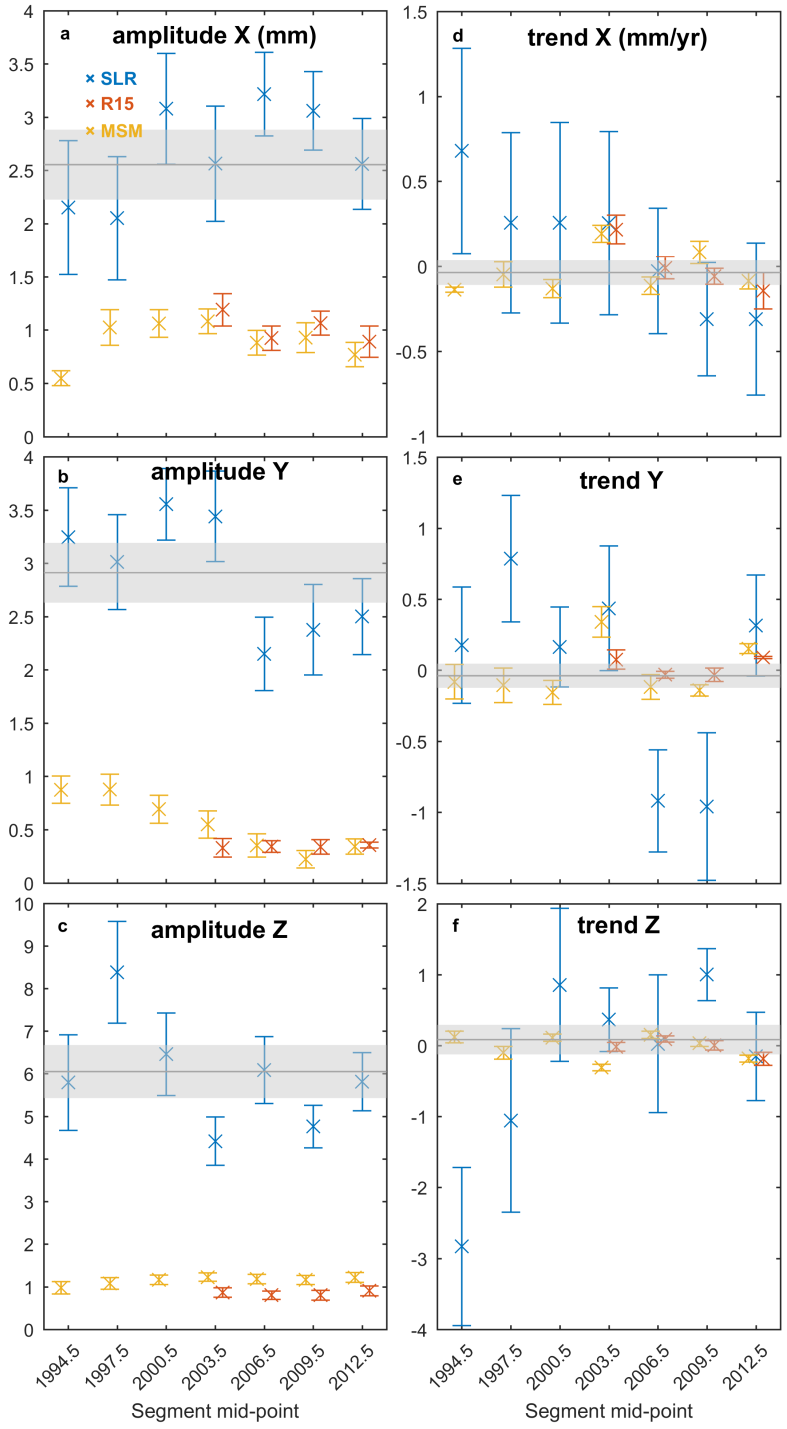

FIGURE 2.4: (a–c) Annual amplitude and uncertainty of each network translation component where each data set has been segmented into 4 year segments with one year overlap for SLR, R15, and MSM with a PLW noise model. Uncertainties are one sigma. (d–f) Linear rates and uncertainty with a PLW noise model of the time series (Figures 2.1d–f). The shaded area is the respective amplitude and linear rate values for the full SLR time series with one sigma uncertainty [1993.0–2015.0]. R15 and MSM have been offset in time for clarity. Four year segments are as follows: 1993.0–1997.0, 1996.0–2000.0, 1999.0–2003.0, 2002.0–2006.0, 2005.0–2009.0, 2008.0–2012.0, and 2011.0–2015.0.

TABLE 2.2: Noise parameters from Hector of the shortened SLR dataset and R15 network translation model [2002.3 – 2014.5]

	X								
	SLR			R15			SLR-R15		
model	white-only	PLW	GGM	white-only	PLW	GGM	white-only	PLW	GGM
AIC	717.384	688.717	668.043	205.392	182.117	171.120	635.281	627.398	623.919
BIC	717.384	694.698	674.024	205.392	188.084	177.087	635.281	633.365	629.886
k	0	-0.90	1.13 $\pm$ 0.39	0	-0.67		0	-0.47	0.44 $\pm$ 0.23
1-phi			0.50 $\pm$ 0.16						0.35 $\pm$ 0.26
STD	2.776	2.464	2.313	0.489	0.443	0.428	2.131	2.043	2.021
bias (mm)	-0.000 $\pm$ 0.229	-0.008 $\pm$ 3.682	-0.022 $\pm$ 0.413	0.026 $\pm$ 0.040	-0.031 $\pm$ 0.225	0.022 $\pm$ 0.062	0.066 $\pm$ 0.176	0.183 $\pm$ 0.559	0.072 $\pm$ 0.265
trend (mm/yr)	-0.000 $\pm$ 0.065	-0.014 $\pm$ 0.270	0.004 $\pm$ 0.115	0.009 $\pm$ 0.012	0.012 $\pm$ 0.032	0.009 $\pm$ 0.017	-0.101 $\pm$ 0.050	-0.105 $\pm$ 0.106	-0.104 $\pm$ 0.075
	Y								
AIC	705.882	646.078	628.424	-20.596	-43.518	-46.146	572.596	551.285	550.747
BIC	705.882	652.059	634.405	-20.596	-37.551	-40.178	572.596	557.252	556.514
k	0	-0.93	0.92 $\pm$ 0.19	0	-0.63	0.39 $\pm$ 0.11	0	-0.80	0.29 $\pm$ 0.07
1-phi			0.31 $\pm$ 0.11			0.12 $\pm$ 0.12			0.06 $\pm$ 0.06
STD	2.670	2.129	2.020	0.225	0.205	0.204	0.719	1.5286	1.573
bias (mm)	0.000 $\pm$ 0.220	0.204 $\pm$ 3.932	0.043 $\pm$ 0.485	0.002 $\pm$ 0.190	-0.001 $\pm$ 0.091	0.003 $\pm$ 0.038	0.325 $\pm$ 0.142	0.357 $\pm$ 0.962	0.342 $\pm$ 0.291
trend (mm/yr)	0.000 $\pm$ 0.062	0.079 $\pm$ 0.245	0.022 $\pm$ 0.133	-0.006 $\pm$ 0.005	-0.001 $\pm$ 0.014	-0.004 $\pm$ 0.010	-0.387 $\pm$ 0.041	-0.351 $\pm$ 0.109	-0.368 $\pm$ 0.078
	Z								
AIC	905.651	860.284	832.483	141.685	121.640	112.263	787.566	766.569	764.327
BIC	905.651	866.265	838.464	141.685	127.607	118.230	787.566	772.536	770.294
k	0	-0.95	1.33$\pm$ 0.37	0	-0.63		0	-0.61	0.36 $\pm$ 0.10
1-phi			0.49 $\pm$ 0.13			0.99 $\pm$ 0.00			0.10 $\pm$ 0.11
STD	5.267	4.404	4.044	0.393	0.361	0.350	3.590	3.287	3.268
bias (mm)	0.000 $\pm$ 0.434	-0.023 $\pm$ 10.493	0.006 $\pm$ 0.860	0.002 $\pm$ 0.033	-0.017 $\pm$ 0.157	0.003 $\pm$ 0.048	0.100 $\pm$ 0.297	-0.019 $\pm$ 1.337	0.052 $\pm$ 0.612
trend (mm/yr)	-0.000 $\pm$ 0.123	-0.066 $\pm$ 0.529	0.032 $\pm$ 0.239	0.006 $\pm$ 0.009	-0.002 $\pm$ 0.024	0.006 $\pm$ 0.014	0.239 $\pm$ 0.085	0.197 $\pm$ 0.214	0.201 $\pm$ 0.167

models (Figure 2.1, noting the same scale is used in the left and right panels). The non-linear signature observed in the temporal domain of the SLR Y component in Figure 2.1b is similarly reflected in Figure 2.2b where the Y component of the SLR origin series shows high power at low frequencies.

The time-variable rate within each data series is shown in Figure 2.4d, e, f, for each of the four-year segments discussed previously. Similarly to the annual amplitude, the largest temporal variability in the short-term rate is found in the SLR Y and Z components (Figure 2.4e, f), with a number of short-term rates significantly different to the rate determined over the full record (grey line, Figure 2.4d, e, f). The section of the SLR X and Z components before 1997.0 are distinctly different from the long-term average, with the Z component almost a factor of three larger than the long-term mean in this period. Segments in the Y component have differences from the mean ranging from +0.8 mm/yr to -0.9 mm/yr, and the two segments covering 2005.0 – 2012.0 are statistically significant from the long-term average. R15 contains contributions from ocean mass and ice sheets mass that are indirectly affected by the GIA model used, which are not included in MSM and could explain some of the offset between the rates derived from the two models.

2.4 Discussion

Our comparison of the SLR translations with respect to the ITRF2014 origin with network translations derived from equivalently sampled geophysical models shows that it is likely that signals of non-geophysical origin, with a range of frequencies (monthly to inter-annual) are insufficiently accounted for in the stochastic model of the ITRF2014 origin. Altamimi et al. (2016) suggested to add annual corrections to the station positions (Equations 2 and 3 in their paper) in order to bring the network origin closer to the instantaneous CM, as sensed by SLR. However, if the annual estimates are partly affected by systematic errors in SLR it remains unclear how these errors will propagate into station positions (and satellite orbits) if the published annual and semi-annual geocentre terms derived from SLR are applied.

Several studies have examined potential systematic error in SLR, in particular the influence of the time-variable ground network distribution (Collilieux et al., 2009; Collilieux and Wöppelmann, 2011), and satellite observation geometry (Spatar et al., 2015) in order to assess uncertainty. Collilieux et al. (2009) found that the SLR network effect could affect the amplitude of the annual geocentre motion in the Z direction at approximately 1-mm, depending on the simulated observing network geometry. We found that the network effect was dominated by the geophysical models' annual signal, rather than the network geometry and account for the SLR network effect by deriving network translations from geophysical models, using only the surface deformation at those active SLR stations for each epoch.

Previous studies have explored uncertainty in the data series submitted to the previous ITRF, ITRF2008 (Altamimi et al., 2011), and found substantial non-linear variation around the origin (Métivier et al., 2010; Argus, 2012). Dong et al. (2014) notes an acceleration in the Z geocentre component of the ITRF2008 origin after 1998, and attributes this to terrestrial water mass redistribution, including mass loss from continental ice sheets and glaciers. We note the same feature in our analysis with a clear change in the short-term rate of the SLR Z component (Figure 2.4f), but note this is not replicated by MSM, even though MSM and Dong et al. (2014) both use the GLDAS terrestrial water storage model. We note there are differences in the glacier and ice sheet mass terms which could explain why the deviation is not present in MSM; the reason for this discrepancy requires further consideration.

Both the land glacier and dam retention components of the MSM surface mass transport model have insufficient temporal resolution to capture the annual component of these constituents. The resolution of surface displacements due to terrestrial water storage changes remains challenging due to deficiencies in hydrologic models, in particular the long-term trends and accurate representation of groundwater use. The missing annual hydrologic signal could explain some of the gap between SLR and MSM, but we note that this signal is included in R15 which also does not agree with SLR in amplitude over a short period.

Others have evaluated the stability of the ITRF2008 origin using statistical and spectral analysis (Collilieux and Altamimi, 2013; Argus, 2012). These analyses show that a coloured noise model is more appropriate than a white noise-only model, an outcome that we find remains robust for the ITRF2014 origin. Argus (2012) demonstrated time-variability in both the annual amplitude and short-term rates of geocentre motion and that the linear CM velocity uncertainties are ± 0.4 mm/yr for X and Y and ± 0.9 mm/yr for the Z component (95% confidence limit). Our findings confirm that a simple linear regression using a white noise-only model will poorly reflect the true uncertainty of the estimated parameters, with the uncertainty for the linear rate typically a factor of five smaller than estimates using a PLW noise model (see Table 2.1 and Table 2.2). Our analysis of the SLR translations relative to the ITRF2014 origin suggests improvement of the CM velocity compared with those from Argus (2012) for ITRF2008. Simply scaling our rate uncertainties to 2 sigma, the PLW noise model results in a 27% improvement of the SLR Z component, reducing from ± 0.9 mm/yr (95% confidence limit) (Argus, 2012) to ± 0.66 mm/yr (95% confidence limit).

The future improvement of the precision and accuracy of the ITRF origin will depend on advances in analysis of SLR data and improved network geometry. Indeed, the present SLR station geometry is sub-optimal, with a concentration of SLR stations in the northern hemisphere decreasing the precision of the Z component compared to the equatorial components (Bouillé et al., 2000; Collilieux and Wöppelmann, 2011; Wu et al., 2012). Otsubo et al. (2016) confirmed this finding with a simulation study indicating that the addition of a station at low latitudes (15°S-30°S)

would improve the precision of the Z component of the geocentre, and that additional sites at high latitudes, particularly in the south, would provide an important improvement in the X and Y geocentre components.

2.5 Conclusion

We assess the temporal variability of the latest SLR translations with respect to the International Terrestrial Reference Frame (ITRF2014) origin, and find significant differences when compared to modelled network translations from two independent surface mass transport models. The proportion of variance explained in the SLR origin time series by geophysical models is on average less than 10% in each component. We identified coloured noise in both observed and modelled network translation time series, but substantial coloured noise remains after subtraction of the model based translations, with notable signal remaining at annual and longer periods. Consideration of power-law noise when estimating the rate in the origin components yields an upper bound five-fold increase in rate uncertainty, compared to the white noise-only case. When using a power-law and white model the uncertainty of the SLR Z component ($\pm$0.33 mm/yr; 1 sigma) is twice as large as that of the X and Y components ($\pm$0.13 and $\pm$0.17 mm/yr respectively). This represents a 27% improvement for the Z component of the results in comparison to those from Argus (2012) for ITRF2008.

Over shorter time-periods, the temporal variability of linear rates computed over four years suggests that the SLR translations with respect to the long-term ITRF2014 origin cannot be rigorously represented by a simple linear model over longer periods. For the annual signal, model based network translations, particularly in the Z component, do not represent the variability in the annual amplitude of the SLR translations with respect to the ITRF2014 origin. This indicates that a significant component of the signal is due to other processes, including likely large systematic error.

Positioning uncertainty for geophysical applications is likely to be impacted by non-linear geophysical signals of the kind we identify in the SLR translation time series with respect to the ITRF2014 origin, and may be further impacted when non-geophysical signals exist. Space geodetic analyses that require an instantaneous CM frame (precise orbit determination for example) will also likely be affected given the annual geocentre motion model used is derived from the same SLR data that is used to define the long-term origin of ITRF2014. Further improvements in SLR data analysis and network geometry are likely required to address this issue. The demonstration of other geodetic techniques to contribute to the Earth's centre of mass determination would also be of great benefit.

2.6 Thesis Context

The study described in this chapter has progressed our understanding of the degree to which geodetic observations can be used to study long term geophysical signals globally, including Australia. Understanding the noise characteristics of the geocentre has fundamental importance for the realisation of the reference frame and surface motion estimates from geodetic techniques such as GNSS. Using a coloured noise stochastic model is a novel method to describe the uncertainty of the centre of mass of the ITRF. Vertical land motion estimates from GNSS are sensitive to uncertainty in the reference frame which impacts any application of derived quantities of interest. This Chapter demonstrates the importance of accounting for coloured noise and non-linear motion of the centre of mass of the Earth when realising the reference frame to ensure that reliable and robust estimates of motion can be inferred from GNSS position and velocities. This Chapter highlights that there is an opportunity for the global community to consider an alternative stochastic model for the realisation of the origin of the International Terrestrial Reference Frame to improve the accuracy and reliability. With an improved understanding of noise and the influence of the chosen stochastic model, this thesis will now focus on the noise present in derived GPS coordinate time series.

Chapter 3

Present-day vertical land motion of Australia from GPS observations and geophysical models

Summary

The secular rate of Australia's vertical surface deformation due to past ice-ocean loading changes is not consistent with present vertical velocities observed by a previously sparse network of Global Positioning System (GPS) sites. Current understanding of the Earth's rheology suggests that the expected vertical motion of the crust should be close to zero given that Australia is located in the far-field of past ice sheet loading. Recent GPS measurements suggest that the vertical motion of the Australian continent at permanent sites is between 0 and -2 mm/yr. Here we investigate if vertical deformation due to previous ice sheet loading can be recovered in the time series of Australian GPS sites through enlarging the number of sites compared to previous studies from 20 to more than 100 and through the application of improved data filtering. We apply forward geophysical models of elastic surface displacement induced by atmospheric, hydrologic, non-tidal ocean, and ice loading and use Independent Component Analysis as a spatiotemporal filter that includes multivariate regression to consider temporally correlated noise in GPS. Using this approach, the common mode error is identified, and subsequent multivariate regression leads to an average reduction in trend uncertainty of 35%. The average vertical subsidence of the Australian continent is substantially different to vertical motion predicted by glacial isostatic adjustment and surface mass transport models.

This chapter has been published as: Riddell, A. R., King, M. A. & Watson, C. S. 2020. Present-Day Vertical Land Motion of Australia From GPS Observations and Geophysical Models. Journal of Geophysical Research: Solid Earth, 125. Minor changes have been made to the original published article for consistency in this thesis. This includes general terminology and grammar.

3.1 Introduction

Accurate knowledge of vertical land motion is key to understanding sea level change and variability in both regional and global contexts (Wöppelmann and Marcos, 2016). To be able to determine regional and global patterns of absolute sea level change, corrections for vertical land motion need to be made to relative sea level estimates from tide gauges (Bouin and Wöppelmann, 2010; King et al., 2012; Pfeffer and Allemand, 2016; Wöppelmann and Marcos, 2016). Vertical land motion originates from both geophysical and anthropogenic sources and is an important factor to consider when inferring global changes from local observations (Dangendorf et al., 2017; Frederikse et al., 2018), and for predicting future sea level changes (Kopp et al., 2014). In the current Intergovernmental Panel for Climate Change (IPCC) Fifth Assessment Report (AR5) (Church et al., 2013), only vertical land motion due to Glacial Isostatic Adjustment (GIA), the solid Earth's response to ice-ocean loading changes (Mitrovica and Milne, 2002; Tamisiea and Mitrovica, 2011), is accounted for in the regional and coastal mean sea level rise projections. Neglecting non-GIA related sources of vertical land motion is likely to bias interpretation of projections in some areas (Dangendorf et al., 2017; Han et al., 2015).

The main geophysical process driving spatially coherent vertical velocities above 0.1 mm/yr globally is GIA. Current geodetic estimates of Australian vertical land motion do not agree with the motion predicted by earlier models of GIA, such as ICE-5G (VM2) (Peltier, 2004), with a discrepancy at the level of a few millimetres per year (e.g. Ostanciaux et al., 2012). Across Australia, recent model predictions of GIA are ambiguous as to the sign of vertical land motion (Figure 3.1), although predictions have values of less than ± 0.5 mm/yr over the Australian landmass (Table 3.1). The differences between GIA models are partly due to their process of construction and theoretical differences in their computation (Whitehouse, 2018).

Whitehouse (2018) provide a comprehensive overview of the response of the solid Earth to past ice loading, commonly represented by various GIA models. Recent advances have led to a better understanding of the components of GIA models, such as the history and construction of ice sheets, the changes to the global ocean and the rheology of the solid Earth, and there will inevitably be differences between GIA models. The main difference between ICE-5G and ICE-6G_C is that the newer model (ICE-6G_C) contains updates in the loading history over Northern America (Toscano et al., 2011). The ANU computation based on ICE-6G provides alternative Stokes coefficients that improve the estimated radial uplift rates in Antarctica (Purcell et al., 2016). Recent sparsely distributed Global Positioning System (GPS) measurements suggest that the vertical motion of the Australian continent at a dozen well distributed permanent sites is between 0 and -1 mm/yr (Altamimi et al., 2016; Burgette et al., 2013; King et al., 2012; Santamaría-Gómez et al., 2012). Here we investigate vertical land motion at more than 100 sites across the Australian continent.

TABLE 3.1: GIA velocity values over the Australian landmass. GIA model descriptions in 3.2.1.4. Statistics computed from gridded data. Caron et al., (2018) 0.4° grid, ICE-6G_C 0.2° grid, ICE6G_C_ANU 1° grid, ICE-5G 1° grid

	Caron et al., (2018)	ICE-6G_C	ICE6G_C_ANU	ICE-5G
Minimum (mm/yr)	-0.47	-0.49	-0.46	-0.43
Maximum (mm/yr)	0.28	0.08	0.01	0.04
Median (mm/yr)	0.11	-0.11	-0.21	-0.15

The present-day vertical velocity field from GPS demonstrates spatial coherency across the Australian continent. If the GPS velocities are correct, this suggests the non-negligible influence of other large-scale geophysical phenomena, for example far-field deformation due to present-day ice unloading and postseismic deformation. If the derived quantities of land motion are biased, they will in turn bias GPS-corrected tide gauge estimates of sea level rise or adversely affect other geophysical interpretation (e.g. surface mass transport, ice loading, postseismic deformation, thermal expansion, groundwater and oil pumping). If biases in vertical land motion estimates are coherent over large spatial scales and sustained over significant time periods, reference frame accuracy is also likely to be affected. Given that GIA models and vertical land motion observations are used to correct tide gauge measurements of relative sea level (White et al., 2014), resolving this discrepancy is important for both regional and global sea level change studies as well as for improving our understanding of crustal deformation and dynamics. The reduction of uncertainty achieved here allows a clearer understanding of spatial and temporal solid earth deformation patterns in Australia.

Systematic error or drift in the GPS reference frame could be an important and widespread source of velocity bias (Argus, 2012; Wu et al., 2011). The Earth's centre of mass (geocentre) is not stationary and its secular and seasonal motion is driven primarily by changes in mass on the Earth's surface and within the interior of the Earth's crust and mantle. GPS station height time series are inherently sensitive to the stability and accuracy of a global reference frame, especially the variations of the origin with respect to the Earth's surface (Serpelloni et al., 2013). The secular origin of the International Terrestrial Reference Frame (ITRF) approximates the centre of mass (CM) of the total Earth system, including the fluid envelope. However, various ITRFs are not perfect realisations of CM even at secular timescales. Argus (2012) found the uncertainty of the ITRF2008 origin translation parameters to be $\pm$0.4 mm/yr for X and Y and $\pm$0.9 mm/yr for the Z component (95% confidence limit). ITRF2014 shows a modest reduction in uncertainty compared with ITRF2008 where the uncertainty of the X and Y components was found to be $\pm$0.3 mm/yr, and a reduction in the Z component uncertainty to $\pm$0.7 mm/yr (95% confidence limit) (Riddell et al., 2017).

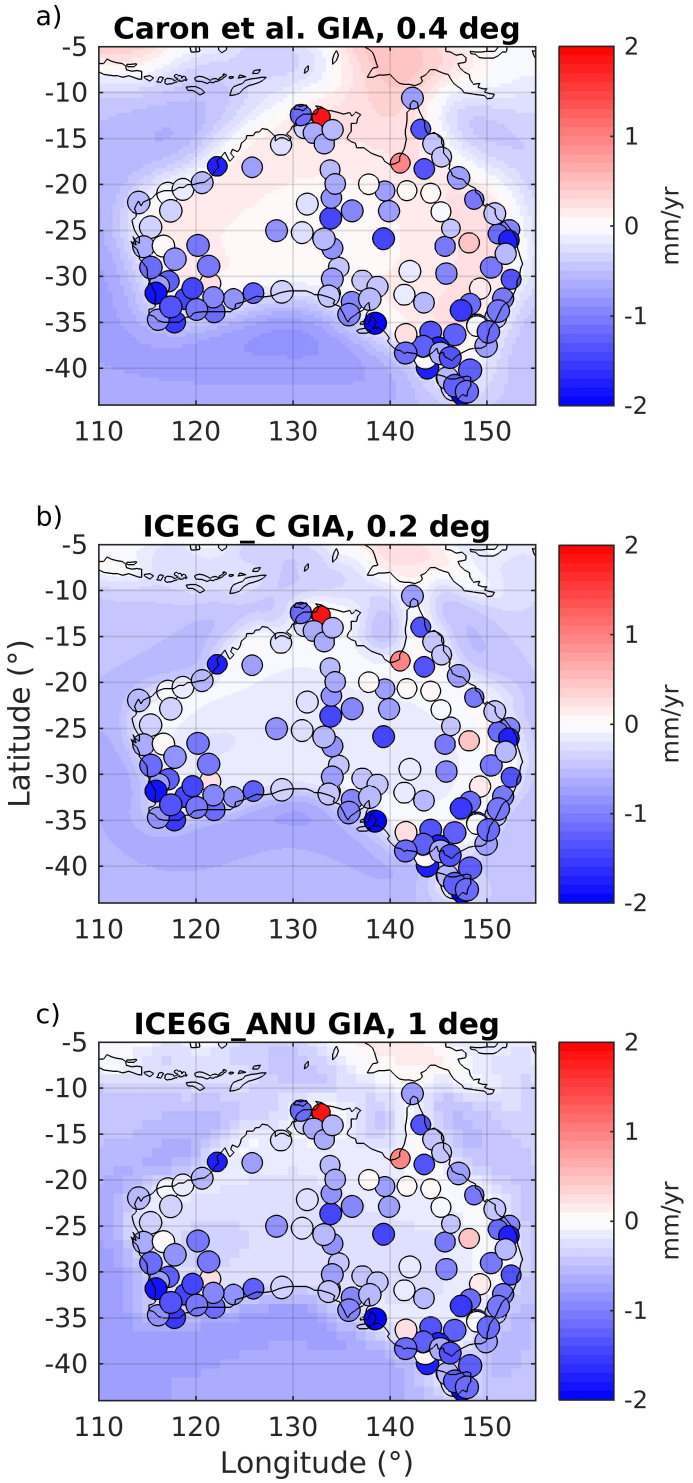

FIGURE 3.1: Present-day GIA (background continuous field) and GPS vertical velocities (dots). a) Caron et al. (2018) GIA on a 0.4° grid; b) ICE-6G_C GIA (VM5a) on 0.2° grid; c) ICE6G_C_ANU on 1° grid. Section 3.2.1.4 provides details of the GIA models. GPS velocities are the same for each panel and computed from our analysis presented here. Dot size is inversely proportional to velocity uncertainty.

Velocities from GPS in an ITRF and from forward GIA models are not strictly directly comparable due to differences in frame origin. Forward GIA models are computed in the centre of mass of the solid Earth (CE) frame which is not accessible by observation (Blewitt, 2003). Over seasonal and shorter time scales the ITRF reflects a centre of figure frame (CF) (Blewitt, 2003; Collilieux et al., 2009; Dong et al., 2003). Jiang et al. (2013) found that the majority (90%) of root mean square variations between loading models computed on a grid in CE and CF frames were below 1%. There are multiple reasons for differences in the uncertainty of the velocity of the centre of the Earth (i.e. the velocity between CM and CE). These include the implicit sources of error in Satellite Laser Ranging (SLR), which is the only geodetic technique currently used to define the Earth's centre of mass. The SLR Z translation rate uncertainty is ± 0.7 mm/yr with a 95% confidence interval (Riddell et al., 2017). By minimising the differences in geodetic observations of vertical land motion rates from GPS and radial land motion rate predictions from a post glacial rebound model, the velocity of CE can be estimated (Argus, 2007; Argus et al., 2010). There is ambiguity as to the magnitude of the absolute motion of the geocentre. Argus (2012) estimated that the CE was moving relative to the Z translation component of CM in ITRF2008 at 0.5 mm/yr over the period 1993.0-2009.0, whereas Schumacher et al. (2018) estimate CE to be moving relative to CM (in ITRF2008) at less than or equal to 0.2 mm/yr in all three translational components (X, Y, Z) over the period 2005.0-2015.0. We also note that other estimates based on analysis of Gravity Recovery and Climate Experiment (GRACE) data over the period January 2003 to August 2016 (Sun et al., 2019), suggest a slightly higher value of 0.5 mm/yr and that this is an area of ongoing investigation. A recent study by (Métivier et al., 2020), has obtained a geocentre velocity reaching 0.9 ± 0.5 mm/yr in 2013 with a Z-component of 0.8 ± 0.4 mm/yr from spherical harmonic coefficients estimated from ITRF2014 Global Navigation Satellite System (GNSS) velocities, over the period 1994.0-2015.1, which is larger than previous estimates and attributed to accelerations of recent global ice melting as a purely elastic response. We consider this further below and note that accurately determining small rates of change from GPS coordinate time series is complicated by reference frame errors and inconsistencies.

Other geophysical phenomena and measurement noise introduces short-term variability in the GPS time series which can bias velocity estimates and/or increase velocity uncertainties. Spatially-correlated noise is the largest source of error in a regional network, and this is also commonly referred to as "common mode error" (e.g. Dong et al., 2006; Liu et al., 2018). To our knowledge, common mode error across a spatially dense field of Australian GPS sites has not previously been investigated. Common mode error within a network of GPS stations can be associated with non-tectonically induced deformation from uncorrected or mis-modelled surface mass transport, including atmospheric, hydrologic and non-tidal loading; tectonic-related crustal deformations; reference frame realisation bias and mis-modelled effects of

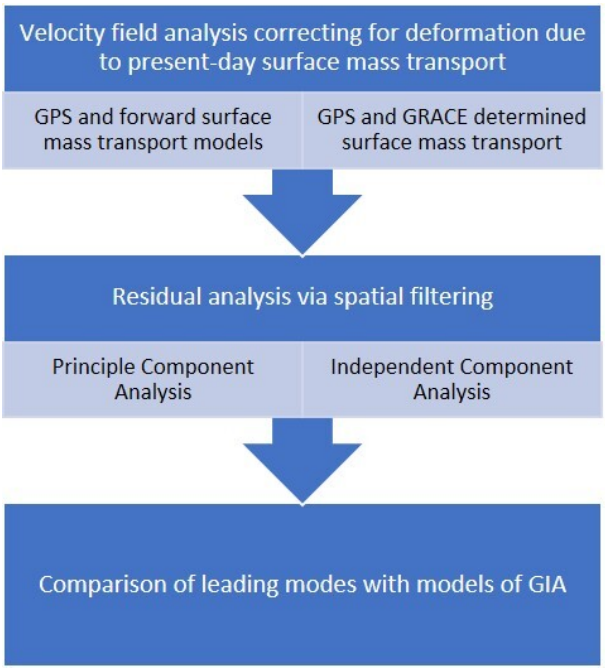

FIGURE 3.2: Process flow and chapter structure

polar motion; satellite errors related to clock, orbit and antenna phase centre variations; and systematic errors caused by software and data processing strategies.

In this Chapter, we seek to identify whether GPS estimates of GIA in Australia are robust and if using decomposition techniques allows the identification or isolation of GIA as a common cause of vertical land motion. To do this, we first remove the short-term variability from GPS time series at Australian sites to avoid biasing trend estimates computed from the vertical component. We then compare our observed velocities of vertical land motion to predicted GIA radial rates. By attempting to obtain present-day velocities reflective of long-term processes, we aim to elucidate signal with geophysical origin above the inherent noise. In the context of this study, "noise" refers to those quantities that are not of geophysical origin. The methodological advances in this research include the use of multivariate regression with powerlaw noise; a unified approach to vertical velocity and uncertainty estimation at Australian sites (including common mode error); and the quantification of the discrepancy between observed and modelled vertical rates of solid Earth motion.

Figure 3.2 shows the processing flow and structure of this Chapter. Section 3.2 presents the data used for the comparison of the GPS vertical velocities with forward surface mass transport models. The models are then subtracted from the GPS to remove short-term variability from the time series. Section 3.3 describes the use of spatiotemporal filtering methods to further filter common mode error. Finally, we compare the final GPS vertical velocities and GIA followed by a discussion of the data, models, assumptions and conclusions.

3.2 GPS data and geophysical models

3.2.1 Data

3.2.1.1 GPS

GPS data from sites in the Australian regional GNSS and AuScope networks (Ruddick and Dawson, 1990) listed in Table B.1, were processed as daily precise point position solutions using GIPSY v6.3 combined with the Jet Propulsion Laboratory (JPL) clock and orbit products (Bertiger et al., 2010; Zumberge et al., 1997). A more thorough description of the parameters, constraints and models are detailed in Appendix B.2. Times of offsets in the resultant time series were identified by considering site log file entries, supplemented by visual identification (Gazeaux et al., 2013). The daily non-fiducial position time series were transformed to ITRF2014 (Altamimi et al., 2016).

Some sites in the Australian network have been operational for more than 22 years, with time series beginning in 1995, but the majority were installed in the period 2010-2013. To maximise the number of sites with a common data period we only used data from 2013 onwards, giving a total of 113 sites. This presents a significant increase in the number of sites used in previous studies, where four sites were used by King et al. (2012) to investigate vertical land motion at tide gauge stations; 12 sites were used in Burgette et al. (2013), with a focus on GPS sites near Australian tide gauges; 13 sites were used by Santamaría-Gómez et al. (2012), again with a focus on GPS sites located near the coast; and 36 Australian sites were used in Altamimi et al. (2016) for the realisation of ITRF2014.

The data used in this analysis spans from 2013.0 to 2019.0 (six years). Data spans of three years or greater are sufficient to determine a horizontal or vertical velocity with realistic uncertainty (Blewitt and Lavallée, 2002; Bos et al., 2010). Bos et al. (2010) took into consideration the effect of coloured noise and found that 4.5 years of daily GPS data is sufficient to reduce the trend uncertainty to below 1 mm/yr (estimated with an annual signal). Consequently, a six-year data span is considered sufficient to determine a robust linear trend and uncertainty in the presence of powerlaw and white noise where the spectral index (κ) is also estimated (that is, not fixed to $\kappa = -1$ (flicker noise), or $\kappa = -2$ (random walk noise)). To estimate velocities from the GPS data we use the maximum likelihood estimator in Hector v1.6 software (Bos et al., 2013), with a powerlaw plus white noise model, simultaneously estimating annual and semi-annual signals as well as offsets with times as predetermined.

Before GPS velocities are compared to GIA, the GPS velocities need to be transformed into reference frames with compatible origins (Argus, 2012). To correct GPS vertical velocities for the CM drift, we use a range of forward models of surface mass transport as an approximation of CE-CM corrections, including those from GRACE with elastic loading due to present day ice mass loss, ideally achieving vertical land

motion values in a secular CF frame. The CF frame can be considered as closely approximating a CE frame (Dong et al., 1997), and is theoretically realised by an infinitely dense and uniformly distributed network of station positions (and velocities) on Earth's surface. The difference between CM and CE is predominantly due to present day mass distributions from ice, terrestrial water storage and the atmosphere.

It is important that all geophysical corrections made to GPS data are also consistent with the geophysical timescale of interest. Changes in the motion of the Earth's rotation pole will change geodetic vertical velocities (King and Watson, 2014). Conventionally the "pole tide correction" (Petit and Luzum, 2010) only removes deformation associated with periods of less than a few years. Longer-term deviations in the data are neglected whereas for comparison to GIA models, for instance, they need to be referred to a reference polar motion compatible with millennial timescales. We discuss our treatment of this bias below.

3.2.1.2 Forward mass transport models

We use two alternative combinations of geophysical forward models to remove the effects of present-day surface loading changes, with the aim to reconcile GPS observations of vertical land motion and motion predicted by GIA models. The first combined forward model accounts for atmospheric, hydrologic and non-tidal ocean loading. The second approach uses surface mass loading determined from the GRACE mission. We assess both to determine the optimal approach and then adopt the time series corrected using the preferred approach in subsequent analysis.

Subtracting models of surface deformation due to surface mass transport is commonly used to reduce time series variance (evidenced by a reduction in root mean square (RMS) error) (e.g. Li et al., 2017). This technique aims to reduce uncertainty and improve accuracy but using RMS as an indicator of reduced variance is not particularly effective at enabling the refinement of secular velocities (Santamaría-Gómez and Mémin, 2015). With a focus on the vertical component, other studies have shown that the impact of mass surface transport caused by continental water (Fritsche et al., 2012), atmospheric pressure (Dach et al., 2011), and non-tidal oceanic loading (van Dam et al., 2012) can bias geodetic velocity estimates depending on the time series length. Reduction of the temporal variability is beneficial for isolating transient signals in the time series and so we use this approach to start our investigation of vertical land motion at Australian GPS sites.

Atmospheric loading displacements were estimated at each site across the Australian AuScope network using the International Mass Loading Service (Petrov, 2015) MERRA_2 products (Gelaro et al., 2017). Terrestrial land water storage was computed using land water storage pressure from the numerical weather model MERRA2 (Reichle et al., 2017). Non-tidal ocean loading, based on the spherical

harmonic transformation of the ocean bottom pressure, were computed with the OMCT05 model (Dobslaw and Thomas, 2007). The atmospheric, land water storage and non-tidal ocean loading surface displacements were downloaded from the International Mass Loading Service (Petrov, 2015) at http://massloading.net/ using Stokes coefficients of the harmonic expansion of the contribution of the atmosphere to the geopotential and Load Love numbers derived on the basis of the Preliminary Reference Earth Model (PREM, Dziewonski and Anderson, 1981). All surface loading products are downloaded with reference to the centre of solid mass of the Earth (CF), which is appropriate for comparison with GPS time series in an ITRF that contain non-linear motion (Dong et al., 2003).

3.2.1.3 GRACE determined surface mass loading

As an alternative approach, we considered surface displacements based on GRACE data. The redistribution of surface mass causing vertical displacement can be well predicted by the GRACE mission (Davis et al., 2004; Wang et al., 2017). Surface loading deformations at Australian GPS sites were extracted from monthly GRACE data and background models where the surface displacement solution is Release-06 from CSR (Center for Space Research at University of Texas, Austin), up to degree 96 using degree-one values from Swenson et al. (2008). The selection of the CSR solution is arbitrary, with differences between alternative solutions from JPL and the German Research Centre for Geosciences (GFZ), being small and within the error bounds of the GRACE solution itself; for further information see Sakumura et al. (2014). The degree-2,0 values were replaced following Cheng and Ries (2017), and spatial filtering following Kusche (2007) (the DDK7 model) was applied. A GIA model is not applied in the CSR spherical harmonic solution.

The surface loading contributions were split up into components from glaciers and ice sheets, and a hydrological module, each of which is accompanied by a self-consistent ocean response to conserve mass at a global scale. The deformations are provided in the CF frame, and represent the elastic response of PREM to the estimated surface loads. The secular linear trend was estimated over 2002-2016 and removed from the modelled surface deformation.

3.2.1.4 GIA

Three GIA forward models are used for comparison to the GPS vertical velocities. Rates of radial displacement on a 0.2 x 0.2-degree grid were downloaded from http://www.atmosp.physics.utoronto.ca/~peltier/data.php (last accessed 7 May 2018) based on the ICE-6G_C ice history model with VM5a Earth model (Argus et al., 2014; Peltier et al., 2015). The model of Purcell et al. (2016) provides an alternative realisation of this model using the same ice and Earth models but a different computational framework, with results provided on a 1-degree grid of GIA

rates that have been modelled with alternative Stokes coefficients, and is hereafter called ICE6G_C_ANU.

We supplement these two conventional forward GIA models with a more recent model determined using a Bayesian framework to generate expected GIA estimates and formal uncertainties globally (Caron et al., 2018). This model is based on 128,000 forward models of varying ice history and 1-D Earth structure constrained by moraine positions, dating history of the ice sheet collapse, tide gauge relative sea level measurements and vertical land motion trends derived from GPS. There are minimal data constraints in Australia. The model output is on a 0.4-degree grid. The uncertainties from this model over the Australian continent are relatively consistent at $\sim$0.12 mm/yr.

3.2.2 Mass loading comparison

The GPS time series are 'corrected' with the modelled surface deformation data to account for inter-annual variability and to obtain a vertical velocity that is not predominantly induced by terrestrial water storage. Table 3.2 shows the median values over the Australian AuScope network where the mass transport models have been removed from the GPS time series. We found that truncating the time series to the time span 2013.0-2019.0, to maximise the number of sites with co-temporal data, does not degrade or significantly change the noise characteristics or velocity estimated from the individual site time series as shown in Appendix Table B.2.

Coloured noise is known to yield quasi-periodic patterns and variations within time series, interfering with the real periodic terms making the detection of signals with small amplitude and power difficult to isolate (Amiri-Simkooei, 2007; Amiri-Simkooei, 2013). Using the maximum likelihood estimator in Hector software, we assess the geophysical models (i. forward surface mass transport models and ii. GRACE derived mass transport) against the GPS time series to attenuate the influence of mass surface loading. The combination of powerlaw and white noise was chosen as the representative noise model for GPS time series (Bos et al., 2007; Santamaría-Gómez et al., 2011; Williams, 2003b), based on both the Akaike information criterion (AIC) and Bayesian information criterion (BIC) (He et al., 2019).

When the respective surface mass transport loading models are removed from the GPS series (GPS minus SMT), the median unfiltered GPS trend shows a reduction of the trend by 0.6 mm/yr (with median uncertainty $\pm$0.5 mm/yr) (Table 3.2). Removal of surface mass transport does not substantially change trend uncertainties, with the exception of when surface displacement from GRACE is removed and the median uncertainty increases from 0.4 to 0.9 mm/yr (1-sigma). The dominant negative trends across the network suggest subsidence is the dominant signal even after consideration of present-day mass loading signals.

TABLE 3.2: Network-wide median values of estimated trends, annual amplitudes and noise parameters, from different treatments of GPS height time series across the Australian network. Different treatments include time series being regressed against mass loading series (REG), or had the surface mass transport (SMT) series removed (RM). Subscript RM is for when the mass loading series have been removed from the GPS time series; Subscript REG for when the mass loading series have been regressed against the GPS time series. κ is the spectral index. A powerlaw plus white (PLW) noise model was used throughout. Uncertainties (one sigma) are shown in brackets, derived by computing the median uncertainty across all sites, along with the first and third quartiles (median uncertainty, first quartile, third quartile).

	Unfiltered GPS	ATM_{RM}	ATM_{REG}	LWS_{RM}	LWS_{REG}	NTO_{RM}	NTO_{REG}	SMT_{RM}	SMT_{REG}	$GRACE_{RM}$	$GRACE_{REG}$
Trend (mm/yr)	-0.8 (0.4, -1.2, -0.4)	-0.2 (0.6, -0.8, 0.0)	-0.4 (0.5, -1.0, 0.0)	-0.3 (0.5, -0.8, 0.1)	-0.4 (0.4, -0.9, 0.0)	-0.3 (0.5, -0.8, 0.0)	-0.5 (0.4, -0.9, 0.0)	-0.2 (0.5, -0.8, 0.1)	-0.4 (0.4, -0.9, 0.1)	-0.4 (0.9, -1.0, 0.1)	-0.5 (0.4-0.9, 0.0)
PLW amplitude (mm/yr$^{-\kappa/4}$)	8.5 (0.2, 7.8, 9.2)	7.6 (0.2, 6.8, 8.3)	7.7 (0.2, 6.9,8.4)	8.8 (0.1, 8.0, 9.5)	8.8 (0.1, 8.0, 9.5)	9.0 (0.2, 8.2, 9.7)	9.1 (0.2, 8.3, 9.7)	7.0 (0.2, 6.4, 8.1)	7.1 (0.2, 6.5, 8.1)	11.3 (0.2, 10.3, 12.0)	9.0 (0.2, 8.3, 9.7)
Spectral Index (κ)	-0.6 (0.1, -0.7, -0.5)	-0.8 (0.1, -0.9, -0.7)	-0.9 (0.1, -0.9, -0.7)	-0.6 (0.1, -0.7, -0.5)	-0.6 (0.1, -0.6, -0.5)	-0.6 (0.1, -0.7, -0.5)	-0.6 (0.1, -0.7, -0.5)	-0.8 (0.1, -0.9, -0.5)	-0.8 (0.1, -0.9, -0.6)	-0.9 (0.1, -1.0, -0.7)	-0.6 (0.1, -0.7, -0.5)
Annual Amplitude (mm)	4.1 (0.4, 3.3, 4.6)	2.3 (0.4, 1.6, 2.9)	2.1 (0.5, 1.6, 2.9)	3.3 (0.5, 2.6, 4.4)	3.4 (0.6, 2.7, 4.3)	4.0 (0.5, 3.1, 4.8)	4.0 (0.5, 3.2, 4.9)	1.5 (0.4, 1.1, 1.9)	1.5 (0.4, 1.2, 2.0)	1.7 (0.6, 1.3, 2.5)	4.0 (0.6, 3.2, 4.9)

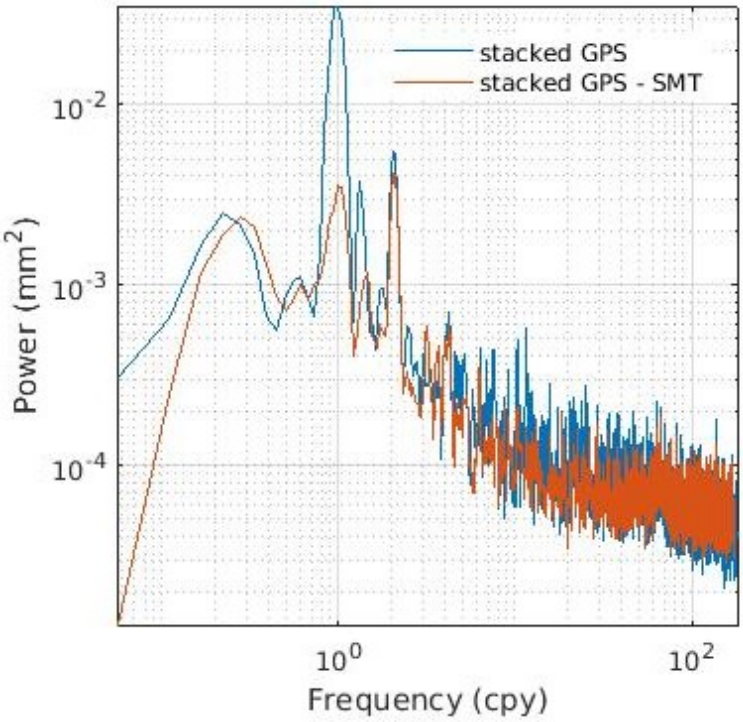

FIGURE 3.3: Power spectral density of unfiltered stacked AuScope GPS sites (blue), and residual stacked GPS after surface mass transport (SMT) models have been removed (red).

The amplitude of powerlaw and white noise is reduced when mass loading series are removed from the GPS time series, an example being the median reduction from 8.5 (with median uncertainty 0.2) mm/yr$^{-\kappa/4}$ to 7.0 (0.2) mm/yr$^{-\kappa/4}$, when the combined surface mass transport loading displacement product is removed from the GPS series. The largest change in spectral index is an increase from a median value of -0.6 (0.1) for the GPS series to -0.9 (0.1) when the GRACE series are removed from the GPS time series, representing a colouring of the noise. It is also interesting to note that removing the atmospheric loading displacement increases the spectral index to -0.9 (0.1).

After following the standard approach of removing mass loading from the GPS time series, we note there is remaining residual signal with some power at annual and semi-annual frequencies (Figure 3.3). We test an idea that the loading models are mis-scaled, due to for example, GRACE or forward model resolution issues meaning the mass change is not sufficiently localised. Consequently, as a variation on the standard removal approach we choose to regress the mass loading time series against the unfiltered GPS time series within Hector while estimating the other parameters and noise model as usual. The multivariate regression considers the relationship between the surface mass transport and the GPS time series in the presence of noise other than white (as would be the case for simply removing the surface mass transport series from the GPS time series).

Regression of each of the forward mass loading models against the GPS time series

results in a larger reduction of the trend uncertainty than simply removing the forward model from the GPS time series (Table 3.2). Regardless of removal (RM) or regression (REG), the trend does not show a statistically significant change from the median original GPS series trend from -0.8 mm/yr for the unfiltered GPS time series to 0.4 mm/yr when the surface mass transport regressed against the GPS series (noting a median uncertainty of 0.4 mm/yr). The median trend across all approaches (summarised in Table 3.2) is negative suggesting that even after the consideration of modelled surface mass transport subsidence is the dominant present-day land motion across the Australian continent.

The median GIA velocity over the Australian landmass for each respective model is -0.1 mm/yr for ICE 6G_C, -0.2 mm/yr for ICE6G_C_ANU, and 0.1 mm/yr for the model from Caron et al. (2018) (Table 3.1). The median GIA velocities over the Australian landmass are substantially different to the median velocity of the GIA models calculated at the GPS sites (Table 3.4), but the level of noise remains too high to identify if GIA is a contributing factor to the distinct pattern of subsidence. The velocity of vertical motion after the respective surface mass transport forward models have been regressed against the GPS height series provides an improvement in the match between GPS and GIA, but the GPS velocities are biased towards the GIA models. This comparison does not account for differences in reference frame between GPS and GIA. Significant residual noise remains in the time series which may mask the geophysical signal of interest (Figure 3.3). To address this potential affect, in the next section a common mode filtering approach is investigated.

3.3 Residual analysis

Using a spatiotemporal filter, we now assess the residuals remaining after including the combined surface mass transport (SMT_{REG} from Table 3.2) as a dependent variable in the regression, with regression parameters estimated in the presence of powerlaw and white noise. Spatiotemporal filtering is an effective method of assessing the relative error contribution of various geodetic datasets and testing if the scaling of the variates is appropriate. We seek to identify and reduce residual common mode error in the Australian AuScope network.

3.3.1 Spatiotemporal filtering

Using the surface mass transport loading deformation at each site within the regression provides a reduction of the powerlaw and white noise and trend uncertainty but substantial noise remains in the solution (Figure 3.3). We therefore attempt to further reduce the noise through empirical filtering. In this section we investigate spatially correlated common mode error using Principal and Independent Component Analysis (PCA and ICA) methods for decomposing GPS time series into temporal

components and their associated spatial responses. PCA methods are well-known and are described, for instance, in He et al. (2015).

Improving the signal-to-noise ratio of geodetic coordinate time series by separating and removing the source signals that contribute to the reduction of precision is an effective way of identifying small or weak deformation signals. Two commonly used matrix factorisation methods for reducing dimensionality in data are PCA and ICA (Hyvärinen and Oja, 2000). Component analysis approaches have been used to identify and remove common mode error in GPS networks for both the spatial and temporal domains (e.g. Dong et al., 2006; Gruszczynski et al., 2016; He et al., 2015; Li et al., 2015; Liu et al., 2015; Liu et al., 2018; Ming et al., 2017; Serpelloni et al., 2013; Shen et al., 2014; Zerbini et al., 2013).

By applying spatiotemporal filtering using the PCA and Karhunen-Loeve Expansion algorithms, the primary objective of Dong et al. (2006) was to identify local site effects within a network of stations. Liu et al. (2015) and Liu et al. (2017) focused on investigating if ICA could be used to identify signals with geophysical meaning related to surface mass loading.

For ICA computations, we use the FastICA fixed-point optimisation algorithm (Hyvärinen, 1999a) to maximise computational efficiency with the pow3 approach, where the derivative function $g = G'$ is termed the non-linearity. Using the classical kurtosis optimisation approach gives the non-linearity $g(u) = u3(pow3)$. The implementation of ICA follows the description in Hyvärinen (1999b) and (Comon, 1994):

$$x = As$$

Where x is an observed m-dimensional vector, s is an x-dimensional random vector whose components are mutually independent (the sources), and A is a constant $m \times n$ matrix to be estimated (mixing matrix). The original sources (s) can be recovered by multiplying the observed signals (x) with the inverse of the mixing matrix $(W = A^{-1})$, also known as the un-mixing matrix.

The separation of independent components from multidimensional data is the objective of ICA, but a well-known issue is that because both the separation matrix and independent components are estimated simultaneously, neither the amplitudes nor the ordering of the components can be established. Hendrikse and Spreeuwers (2007) consider ordering the components based on the power of each component as a contribution to the independent components. Strong sources are those that provide a larger contribution, and weaker sources are those that present a smaller contribution to the overall signal. Selection of the components with the highest power mimics the ordering of eigenvectors in PCA, which provides the best selection of independent components in the realm of least squares. We apply this pseudo-ordering of ICA components to identify the largest contributors. Gaps in the time series of individual

sites were initially infilled with a spatial mean, and then updated with reconstructed series from the six leading PCA modes.

Each GPS position component (north, east, up) is assessed individually considering that spatial cross correlations between components are not likely to be significant (Amiri-Simkooei, 2013). Cross correlations between the position components of the Australian AuScope GPS network were confirmed as insignificant and only the results of the vertical time series are presented here.

3.3.2 Results

We find that the leading six modes of PCA are representative of the common mode error in the GPS time series noting the common spatial pattern and proportion of variance explained. For ICA the appropriate number of principal components used needs to be resolved. Here, the number of principal components used in ICA was determined using a trial and error approach (Barnie and Oppenheimer, 2015). Careful consideration needs to be given using this approach as too many principal components retained can result in overfitting sources as isolated spikes, and too few can result in discarding useful information (Hyvärinen et al., 1999).

The temporal and spatial representations of the leading modes are shown in Figure 3.4 following principal and independent component analysis of the AuScope GPS vertical time series. We normalise each time series to allow the comparison of PCA and ICA time series. Each spatial response is normalised by the maximum absolute value to enable comparison and are scaled to lie between -100% and +100%.

For large networks, common mode error is generally represented by smooth transitional patterning of the spatial response (Serpelloni et al., 2013). The common sign of the spatial eigenvector in Figure 3.4 provides a strong indication that the modes from each analysis demonstrate a coherent and common spatial pattern that can be interpreted as a signal above the noise floor. The temporal series of the leading principal component (PC1) and the first independent component (IC1) show a quasi-periodic signal with similar amplitude that is prevalent in the series even after removing modelled deformation due to atmospheric, land water storage and non-tidal ocean surface mass transport. This suggests short term quasi-periodic signals remain in the GPS height series are spatially coherent over length scales more than 4000 km; whether these are due to surface loading model deficiencies or other affects requires further investigation.

We removed the leading modes from the GPS time series and examined its effect on temporal and spatial variability. We found that this approach did not substantially improve the time series and note that this approach of simply subtracting common modes from time series neglects the temporal correlation of noise and uncertainty propagation. To improve on this, we took the approach of regressing the principal

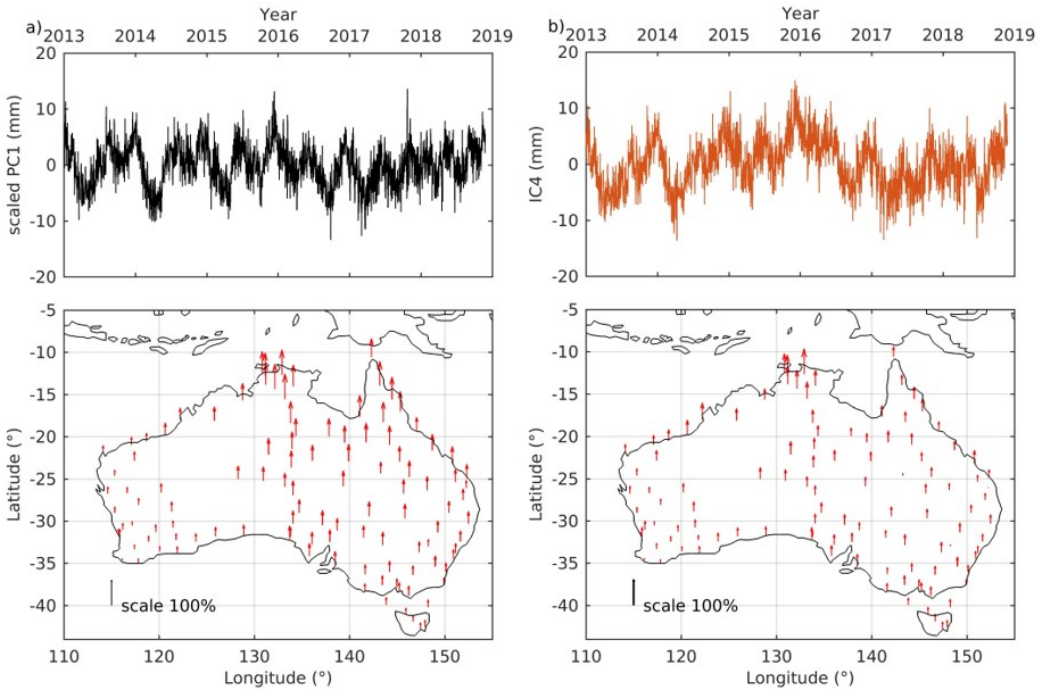

FIGURE 3.4: Temporal and spatial response of the leading modes from a) PCA and b) ICA, where for both the loading due to surface mass transport (atmosphere, land water storage, non-tidal ocean) at each site has been removed prior to analysis. Top is the scaled leading component time series and below is the normalised spatial eigenvector (not displacement direction). The vertically upwards arrows represent a positive spatial response, and down arrows represent a negative spatial response.

modes against the original GPS time series while also co-estimating other parameters and noise models as above.

The leading modes from both PCA and ICA were detrended then regressed individually and collectively (PC1-2, PC1-3, PC1-4 etc.) to assess the change in noise characteristics and to determine which component analysis method is more effective at reducing noise and trend uncertainty. The regression coefficients are generally less than one with a median value of 0.8 for PCA components and 0.7 for the ICA components (Table B.1). The modes can also be used to make downstream determinations of individual site anomalies and regional deformation patterns.

We compared the estimated noise characteristics for the time series after removing regressed leading modes, PC1 and IC1, against those for the unfiltered GPS time series. The results in Table 3.3 show the larger reduction of powerlaw noise amplitude, spectral index and trend uncertainty for the PC1 regression, where the powerlaw noise amplitude of the unfiltered GPS series are changed from 8.5 (0.2) $\mathrm{mm/yr}^{-\kappa/4}$ to 8.7 (0.2) $\mathrm{mm/yr}^{-\kappa/4}$ and 7.8 (0.2) $\mathrm{mm/yr}^{-\kappa/4}$ after the leading modes from ICA and PCA have been removed and regressed respectively. As more of the leading modes are included in the regression, (e.g. top 4 components, 1:4), the difference in powerlaw noise amplitude and trend between PCA and ICA is reduced from a 10% difference to a 5% difference.

A general concern with PCA is the orthogonality constraint imposed by the statistical definition of the method. By defining that the primary and secondary axes of the maximum variation must be orthogonal, a constraint is placed on analysis that can result in over, or under, interpretation of real spatial and temporal variability. We address this by providing results from ICA as a comparison and noting that they are similar. The combination of the top 4 independent components (Table 3.3) demonstrated a larger relative reduction of powerlaw amplitude, reducing the median powerlaw and white noise from 8.7 (0.2) $\mathrm{mm/yr}^{-\kappa/4}$ of the first independent component to 7.2 (0.2) $\mathrm{mm/yr}^{-\kappa/4}$ for the leading four independent components combined.

The regression coefficient from the multivariate regression analysis demonstrates a similar scaled magnitude and spatial pattern as the spatial eigenvectors from each PCA and ICA analysis, providing confidence in the regression technique. A check of the independent component ordering also showed that the regression of the first independent component against the individual GPS time series showed the largest reduction in powerlaw noise amplitude, the smallest trend uncertainty, and the lowest spectral index when compared to the other independent components, providing validation that the pseudo-ordering of the independent components is reasonable.

The median value of the GPS vertical velocities with the common mode error removed (the top 4 modes from ICA) is -0.5 mm/yr with a median uncertainty of 0.4 mm/yr compared with the same statistic computed from the unfiltered velocity

field of -0.8 (0.4) mm/yr (Table 3.3). Independent and principal component analysis provided similar velocities when the residual time series were regressed against the original GPS time series over the period 2013.0-2019.0 and so we compare only the GPS velocities computed after removal of regressed ICA to GIA. By reducing common mode error in GPS time series, we can better isolate the remaining signal with the assumption that this represents underlying vertical land motion and compare the velocities with those predicted from GIA models.

3.3.2.1 GIA velocity comparison

The median uplift velocities from the three GIA models are shown in Table 3.4, after interpolation of the GIA grids to the GPS site locations. The GPS and GIA models all agree within one-sigma, but this assumes that the uncertainties are robust. In fact, the median residual trend after filtering remains as subsidence within the network. The mean trend of GIA radial displacement from the ICE6G_C model, interpolated at each of the GPS sites is -0.12 mm/yr (uncertainty is not provided). The remaining signal cannot clearly be attributed to GIA and could be the product of other large-scale geophysical phenomena, reference frame error or systematic error within the GPS series (such as effects related to aliasing at draconitic periods).

To mitigate the effects of reference frame errors, a re-comparison of the GPS and model outputs is completed by considering the spatial covariance of the estimated trends. The empirical semi-variogram for the GPS shown in Appendix B, Figure B.1a suggests the correlation length for GPS to be around 500 km, while this is larger than 2000 km for the GIA models (Figure B.1b and Figure B.2).

3.4 Discussion

The contribution of GIA to vertical land motion velocities in Australia is expected to be relatively small considering that Australia lies in the far-field of the past major ice sheets (i.e. North America, Northern Europe, Greenland). However, as the different contributions of surface mass loading's improve, the discrepancy between GPS and GIA velocities is worthy of investigation noting the importance of both in sea level studies. GIA models are commonly used as a correction in both altimetry and tide gauge studies (Tamisiea, 2011), and so the validity of the modelled deformation is paramount for reliable sea level estimates. In Australia, previous studies have noted that GIA is close to zero, whereas the GPS observations show a general rate of subsidence that is currently unexplained.

We have demonstrated that the noise level in residual time series from Australian GPS sites, combined with reference frame uncertainty remains too high to confidently separate competing GIA models even after cleaning and filtering. Mismatches between the decomposed and filtered GPS observations and GIA models could result from other sources of uncertainty in GPS such as draconitic aliasing

TABLE 3.3: As for Table 3.2, but from both unfiltered and filtered GPS time series following the regression of the leading components from PCA and ICA of the GPS network where the combined surface mass transport loading has been removed from the GPS series prior to spatiotemporal filtering (see Section 3.2.2).

	Unfiltered GPS	PC1	IC1	PC1:2	IC1:2	PC1:3	IC1:3	PC1:4	IC1:4
Trend (mm/yr)	-0.8 (0.4, -1.2, -0.4)	-0.4 (0.4, -0.9, 0.0)	-0.7 (0.5, -1.1, -0.2)	-0.4 (0.4, -0.8, 0.0)	-0.7 (0.5, -1.1, -0.2)	-0.4 (0.3, -0.8, 0.0)	-0.6 (0.4, -1.1, -0.1)	-0.5 (0.3, -0.7, 0.0)	-0.5 (0.4, -0.9, 0.0)
PLW Amplitude (mm/yr$^{-\kappa/4}$)	8.5 (0.2, 7.8, 9.2)	7.8 (0.2, 7.3, 8.8)	8.7 (0.2, 8.0, 9.6)	7.3 (0.2, 6.5, 8.4)	8.2 (0.2, 7.5, 9.2)	6.8 (0.1, 6.0, 7.7)	7.7 (0.2, 6.9, 8.7)	6.8 (0.1, 6.0, 7.5)	7.2 (0.2, 6.6, 8.0)
Spectral Index (κ)	-0.6 (0.1, -0.7, -0.5)	-0.6 (0.0, -0.7, -0.5)	-0.7 (0.1, -0.9, -0.6)	-0.6 (0.0, -0.7, -0.5)	-0.7 (0.1, -0.9, -0.6)	-0.6 (0.0, -0.7, -0.5)	-0.7 (0.1, -0.8, -0.6)	-0.6 (0.0, -0.7, -0.5)	-0.6 (0.1, -0.7, -0.5)
Annual Amplitude (mm)	4.1 (0.4, 3.3, 4.6)	4.0 (0.4, 3.3, 4.9)	3.2 (0.5, 2.5, 4.0)	3.9 (0.4, 3.3, 4.6)	3.7 (0.5, 3.2, 4.3)	3.6 (0.4, 3.1, 4.3)	3.6 (0.4, 3.1, 4.2)	3.6 (0.4, 3.0, 4.3)	3.7 (0.4, 3.2, 4.3)

TABLE 3.4: Median trend of GIA models interpolated at the GPS sites, and regressed leading modes from PCA and ICA. The trend uncertainty for the GIA model from Caron et al. (2018) is presented as a formal uncertainty assuming no covariance using inverse proportional weighting. Uncertainty values for ICE6G_C and ICE6G_C_ANU are not available.

	ICE6G_C	ICE6G_C_ANU	Caron et al., (2018)
Trend (mm/yr)	-0.12	-0.20	0.03 (0.12)

with seasonal signals (Amiri-Simkooei, 2013; Bogusz and Klos, 2015; Ray et al., 2007); other unconsidered geophysical processes, such as thermal bedrock expansion (Wang et al., 2018; Yan et al., 2009); site-specific effects such as multipath or antenna phase centre corrections (King and Watson, 2010) and reference frame alignment (Argus, 2012; Riddell et al., 2017; Santamaría-Gómez et al., 2017).

Due to the shortness of the time series we are not able to separate the solar seasonal and draconitic signals in a harmonic analysis. We expect that the contribution from draconitic signals would be small. Using an extended set of global sites, yet a comparable GPS analysis strategy to our approach, Amiri-Simkooei et al. (2017) find that the mean amplitude of the first eight draconitic signals have an amplitude of less than 1 mm for the horizontal components and 2 mm for the vertical component. Coloured noise is known alias with periodic patterns and variations (Amiri-Simkooei, 2007; Amiri-Simkooei, 2013), mixing with the real periodic terms in time series, making the detection of signals with small amplitude and power difficult to isolate.

We note that there is a limitation associated with the length of the time series that is related to the installation date of when the majority of the Australian sites were installed. Unfortunately, while there are a small number of sites that have operated for an extended period (eight sites since the mid-1990s), the majority (more than 80%) of the sites were installed after 2012. Klos et al. (2017), demonstrated using a global network of 174 GPS sites processed with GIPSY that 13 years of data was able to attain a trend uncertainty of less than 0.1 mm/yr for the horizontal components and less than 0.15 mm/yr for the vertical components (simultaneously estimating time-variable seasonal signals). Assuming the noise model is time constant and representative, using a simulation of temporally correlated noise in GPS time series with amplitudes ranging from 1 to 25 mm/yr$^{-\kappa/4}$ we find it would take >10 years for the trend uncertainty to reach $\sim$0.1 mm/yr at an individual site. Using the median noise amplitude from our data of 8.5 mm/yr$^{-\kappa/4}$, we find approximately 15 years is required to reach $\pm$0.1 mm/yr. Initial investigations were performed with less sites over longer periods of time, but the spatial resolution of the principal and independent components (common mode error) was compromised by the reduced number of sites and length of separation between the available sites. Here we aim to maximise the number of sites while still robustly estimating the trend uncertainty,

and so use the sites with time series available from 2013.0-2019.0.

GPS reference frame bias will likely contribute to the mismatch of median values between the GPS and GIA models since ITRF does not necessarily accurately represent CM. Past ice loss and present-day ice mass loss are not likely to provide a significant difference in the CE and CM (Argus, 2012), with the assumption that plate interiors are not drifting with respect to CE. However, a drift can exist between the reference frame origin and the true Earth centre of mass which manifests as a bias between measured and modelled vertical velocities (van der Wal et al., 2015). The reference frame uncertainty over Australia is likely larger than the GPS uncertainties, where Argus (2012) estimated the CE velocity from GPS vertical observations to be +0.4 mm/yr for the X and Y components, and +0.8 mm/yr at the upper bound for the Z component for ITRF2008. By comparing estimates from very long baseline interferometry and satellite laser ranging, Wu et al. (2011) found that the uncertainty of the scale drift of ITRF2008 was +0.16 mm/yr, which may also contribute to the observed differences between GPS and GIA. Using the results from Riddell et al. (2017), we calculate the expression of ITRF2014 geocentre drift in the vertical direction at Alice Springs (central Australia) to be $\sim$0.5 mm/yr.

GIA models are computed in a CE system, whereas GPS (referenced to an ITRF) is representative of CM at temporal scales longer than a few seasonal cycles. Although the differences between the reference frames are considered to be small, they may contribute to the discrepancy between GPS trends and GIA velocities. Postglacial rebound models have an implicit assumption that the plate interiors are moving vertically relative to the CE (Argus, 2012). Due to the small ongoing differences in ocean water distribution due to GIA, the difference between GIA predictions in CM and CE is minimal (Argus, 2007; Klemann and Martinec, 2011). Station velocities from GPS are reference frame dependent being affected by both rotation and translation parameters. Uncertainty in the reference frame origin translation parameters will likely contribute to GPS error, and are larger than the bias associated with different CE and CM frames.

Variations in surface mass transport loading due to hydrologic forcing and terrestrial water storage is not well modelled primarily due to the absence of a global monitoring network and a lack of understanding of the temporal and spatial unpredictability (Lettenmaier and Famiglietti, 2006). Terrestrial water storage load is known to deform the Earth's surface and influence the annual signal of GPS time series, particularly the vertical component. Although GRACE is able to provide a global picture of mass redistribution, it is not able to recover variations in the total mass of terrestrial water storage (degree-0 coefficients) (Meyrath et al., 2017). Hydrologic models are also limited by the omission of polar ice sheet contributions and poor representation of groundwater storage. Groundwater has not been considered here despite knowing that extraction and recharge signals can significantly contribute to vertical land motion signals, for example in the Perth basin (Featherstone et al., 2015).

Inter-annual variability of the terrestrial water storage deformation signal in Australia is largely related to the El-Niño Southern Oscillation (ENSO) and the Indian Ocean Dipole (Forootan et al., 2012; García-García et al., 2011). This signal was observed as a spatial pattern in the second principal component and independent component (Figure B.3), where the spatial eigenvectors of sites towards northern Australia focused around the Gulf of Carpentaria are flipped in sign, compared to other sites. Forootan et al. (2012) were able to demonstrate that climate teleconnections, such as the El Niño-Southern Oscillation, and independent components of GRACE in northern Australia were significantly correlated. In Australia, the apparent vertical land motion due to Neogene tilting as a N-down, SSW up differential reflects contributions from both dynamic topography and the geoid evidenced by paleo-shorelines (Sandiford, 2007).

Each of the GIA models will also contain levels of uncertainty due to discrepancies in approach and assumptions made during computation. Uncertainties from the definition of the spatial and temporal variations in the ice load and uncertainties in the viscoelastic rheology of the solid earth will propagate into the GIA modelled radial rate (Martín-Español et al., 2016). Unlike the Caron et al. (2018) model, the ICE-6G_C (VM5a) and ICE6G_C_ANU forward GIA models are not provided with uncertainty estimates which makes it difficult to determine if the radial velocities in Australia are considered statistically significant from that model. Assumptions made about the viscosity of the mantle will propagate as differences between the respective GIA models and each models' respective difference from the median GPS velocity. Uncertainties for GIA models are difficult to compute given the unknown unknowns and while Caron et al. (2018) are able to provide uncertainty estimates, it is unclear whether these are realistic and representative of the fit between GPS data and the GIA model in regions such as Australia where minimal GPS data is used to constrain the model.

Using a median value as the primary metric of comparison between rates of land motion presents some limitations over an irregularly distributed and sparse network. This assumes that there is minimal spatial autocorrelation which we know is not the case over the Australian continent but is sufficient here as we are conducting a first order comparison. A more complex comparison accounting for spatial autocorrelation is planned for future research.

The improved techniques (multivariate regression to account for variation and trend estimation in the presence of coloured noise) yield improved geophysical interpretation given a reduction in uncertainty in long term rates of vertical land motion. Our work provides an improved quantification of these land motions, highlighting that the observed land motion cannot be explained by GIA or other elastic modelling over shorter time scales – we contend this is an important incremental advance in understanding land motion in Australia, yet also provides insight in the techniques also applicable elsewhere.

Improved trend estimates of vertical land motion directly improves our understanding and interpretation of the velocity field dynamics in Australia. We were able to achieve a reduction of the variability in the Australia GPS series providing a refined estimate of trend and uncertainty following spatiotemporal filtering. A comparison of the traditional practice of removing the common mode error with the novel approach taken in this Chapter by regressing the common mode error demonstrates that including the leading modes in the regression analysis as dependent variables further reduces the noise. Providing realistic uncertainty estimates of height changes is paramount for downstream geophysical interpretation and allows an improvement of the signal-to-noise ratio to isolate small deformation signals.

The installation date and location of the Australian AuScope sites has an influence on the application of spatial filtering methods. The AuScope GNSS network was designed and installed with the intent of 200 km nominal spacing between stations (Johnston et al., 2008). This has been achieved in some areas, but there remain large portions of the continent where there is noticeably sparse coverage (i.e. Western Australia). Amiri-Simkooei (2013) demonstrated that spatial correlations of individual components (north, east, up) between stations are significant over angular distances of 30° (∼3000 km) and that maximum spatial correlations are found between the nearest sites, suggesting that noise in GPS time series has a physical basis. Gruszczynski et al. (2016) looked for common spatial response of 87 GPS sites in central Europe using PCA where maximum site separation was less than 1900 km. The maximum distance between any two sites in the AuScope network is < 1000 km [WLAL to WARA is approximately 995 km]. There is presently a trade-off between using longer time series to improve the signal-to-noise ratio of the vertical time series and the spatial density of sites given the number available.

Considering that GPS is a point source measurement and only representative of the change at a single location, it would be relevant to investigate the use of other space geodetic techniques in the future that are capable of continental-wide motion, such as Interferometric Synthetic Aperture Radar (InSAR).

3.5 Conclusions

This Chapter investigates the present-day velocity and spatial variability of GPS-derived vertical land motion across Australia and finds distinct patterns that can be only partially explained by GIA. These are compared with models of GIA in an attempt to separate competing GIA models which show either subsidence or uplift across Australia. Time series of 113 Australian GPS sites are analysed to quantify the residual noise magnitude after removing geophysical models of surface mass transport from atmospheric, water and non-tidal ocean influences, as well as mass loss from past ice sheets and glaciers. Previous studies of Australian vertical land motion have relied on less than 20 GPS sites.

By using multivariate regression of surface mass transport in the presence of powerlaw noise, we reduce the temporal variability of the GPS series and then test the impact of regressing the leading ICA mode against the residuals from the GPS analysis. Simply removing the leading mode from the time series and then comparing the noise properties of the resulting time series does not consider the aliasing of coloured noise with periodic patterns. In our analysis, once the common mode error has been identified the leading modes are regressed against the original GPS time series. Spatiotemporal filtering provides a methodology for reducing correlated errors between stations within a regional network allowing for the suppression of noise. This results in better estimates of solid earth deformation in the Australian region and evidence of common mode error.

The technique of multivariate regression is advanced by the use of coloured noise to account for variation and trend estimation. We regress the determined component time series against the GPS time series as a method of detecting change in the noise properties in the presence of powerlaw and white noise. We then compare the noise characteristics of the original time series with the multivariate regressed time series and note a substantial reduction of powerlaw and white noise amplitude from 8.5 (0.2) $\mathrm{mm/yr}^{-\kappa/4}$ to 7.0 (0.2) $\mathrm{mm/yr}^{-\kappa/4}$.

The average vertical subsidence of the Australian continent is substantially different to vertical motion predicted by postglacial rebound models. This is based on the evidence that the median vertical trend of land motion across the Australian continent is -0.8 mm/yr with a median uncertainty of 0.4 mm/yr, and first and third quartile values of -1.2 and -0.4 mm respectively. The background rates of motion from postglacial models across Australia range between -0.20 – 0.03 mm/yr. We note that it is challenging to have a statistically significant difference given the irregular spatial distribution of sites across the continent, the non-gaussian distribution of rates and their associated uncertainties, and unknown uncertainty of the ICE 6G/VM5a vertical rate predictions.

We note that uncertainty in the absolute reference frame is likely at the level of 0.5 mm/yr and will likely contribute to the discrepancy between GPS and GIA vertical velocities. Here we have considered that the reference frame errors would express in a spatially coherent way across the spatial scale of the Australian continent. Spatiotemporal filtering is an effective method of assessing the relative error contribution of various geodetic datasets to geophysical interpretation. This leads to a more rigorous determination of vertical land motion, which is particularly important for sea level estimation at tide gauge sites along the Australian coastline.

3.6 Thesis Context

By publishing the first vertical land motion estimates using a Precise Point Positioning approach exploiting the entire Australian AuScope GNSS array, the study

presented in this chapter advances our understanding of broad scale continental deformation across the Australian continent. Understanding uncertainty sources and applying multivariate regression have allowed more robust position and velocity estimates leading to a better understanding of surface motion of the Australian continent. These vertical land motion estimates can then be applied to a range of applications, such as at tide gauge sites to assist with the determination of absolute sea level change. GPS site velocities are also fundamental to the realisation of the ITRF and other national datums, particularly at the geodetic observatories where multiple observing techniques are co-located. Improved GPS site velocities as produced here are required to drive improvement in the ITRF in the Australian region. With the aid of the improved coordinate time series and noise analysis, improved geophysical interpretation is now possible. By the end of this Chapter this thesis described research that has developed an understanding of the uncertainty in the reference frame, removed much of the local to regional common mode error and explored the secular velocity of Australia within the context of ITRF2014. This progresses in the next chapter to explore non-linear large-scale geophysical signals across the Australian continent.

Chapter 4

Ongoing postseismic deformation of the Australian continent from far-field earthquakes

Summary

We use Global Positioning System (GPS) observations to investigate the magnitude and spatial distribution of vertical coseismic and postseismic deformation of the Australian continent and compare these with elastic and viscoelastic model outputs. We observe and model surface deformation in Australia caused by six recent large far-field events: 2004 M_W 8.1 Macquarie Ridge, 2004 M_W 9.3 Sumatra-Anderman, 2005 M_W 8.6 in northern Sumatra, the 2007 series of M_W 8.5 and 7.9 in southern Sumatra, two events in 2012 of M_W 8.6 and 8.2 in northern Sumatra, and the 2009 M_W 7.8 south of New Zealand. Observed vertical coseismic deformation reaches 3 mm, with the magnitude varying spatially and by earthquake in broad agreement with modelling of coseismic deformation. Postseismic deformation is observed in all three coordinate components at Australian GPS sites nearest to these earthquakes, with deformations reaching several mm/yr in the vertical over multiple years. In particular, the Sumatran sequence produces observed subsidence in north-western Australia of up to 4 mm/yr over 2004.9-2010.0 where predictions based on one-dimensional viscoelastic Earth models replicate the subsidence but underpredict the vertical rate by a factor of two. Across all earthquakes, the models often fit one or two coordinate components of the observations, but rarely all three. Unmodelled lateral rheological structure likely contributes to this given the difference between the oceanic location of the earthquakes and the Australian continental setting of the GPS sites. The magnitude and spatial extent of these coseismic and postseismic deformations warrant their consideration in future updates of the geodetic terrestrial reference frame.

4.1 Introduction

The conventional theory of plate tectonics suggests that earthquakes in their most simple form are a result of the interaction between "rigid plates" (Müller and Seton, 2015). Being located far from active plate boundaries, continental Australia experiences very infrequent large-magnitude seismicity, and hence intraplate crustal deformation, aside from instantaneous deformation due to large and far-field plate-boundary earthquakes. However, the complex stress fields at plate boundaries results in far-field deformations that have been observed across Australia in the horizontal coordinate component (e.g. Burbidge, 2004; Kennett and Blewett, 2012; Tregoning et al., 2013). Recent geodetic evidence has shown that plate interiors globally are deforming horizontally due to near and far-field earthquakes, both co-seismically and post-seismically, including Australia (e.g. King and Santamaría-Gómez, 2016; Tregoning et al., 2013)

The Australian continent is located entirely within the Indo-Australian Plate (Figure 4.1), which has been formerly labelled as a 'plate of extremes' (Keep and Schellart, 2012) due to the complex plate boundary interactions. The plate boundary includes the large converging mountain range on the north-western margin (the Himalayas); one of the largest convergent subduction zones (Sunda megathrust) located along the north-eastern boundary (Yong et al., 2017); and the inclusion of one of the fastest subduction zones on Earth (the Tonga-Kermadec-Hikurangi zone) along the eastern boundary (Bevis et al., 1995). The variety of plate boundary interactions provides various mechanisms for significant numbers of earthquakes, some with very large magnitudes.

Geodetic studies have shown non-negligible horizontal coseismic and postseismic deformation of Australia (Tregoning et al., 2013) but these have not yet been extended to consider the vertical component of coseismic and postseismic deformation. The theoretical potential for cumulative horizontal coseismic deformation in Australia was highlighted by Métivier et al. (2014) to be $\sim$1 cm over the period 1991.0-2011.0, but there are no observational studies that have focused on vertical coseismic deformation in Australia. As a result of mega-earthquakes, Trubienko et al. (2014) showed that the accumulated postseismic deformation values in the far-field (500-1500 km) of the Sumatra 2004, Chile 2010 and Japan 2011 earthquakes could be as large as the coseismic offsets after 3-4 years of deformation with a tendency towards subsidence, but did not investigate sites in Australia.

The deformation of the Earth's crust and mantle after an earthquake is a function of the earthquake magnitude, the rheological structure of the solid Earth, and the

This chapter has been submitted to Geophysical Journal International, June 2020. Minor changes have been made to the article, as submitted, for consistency in this thesis.

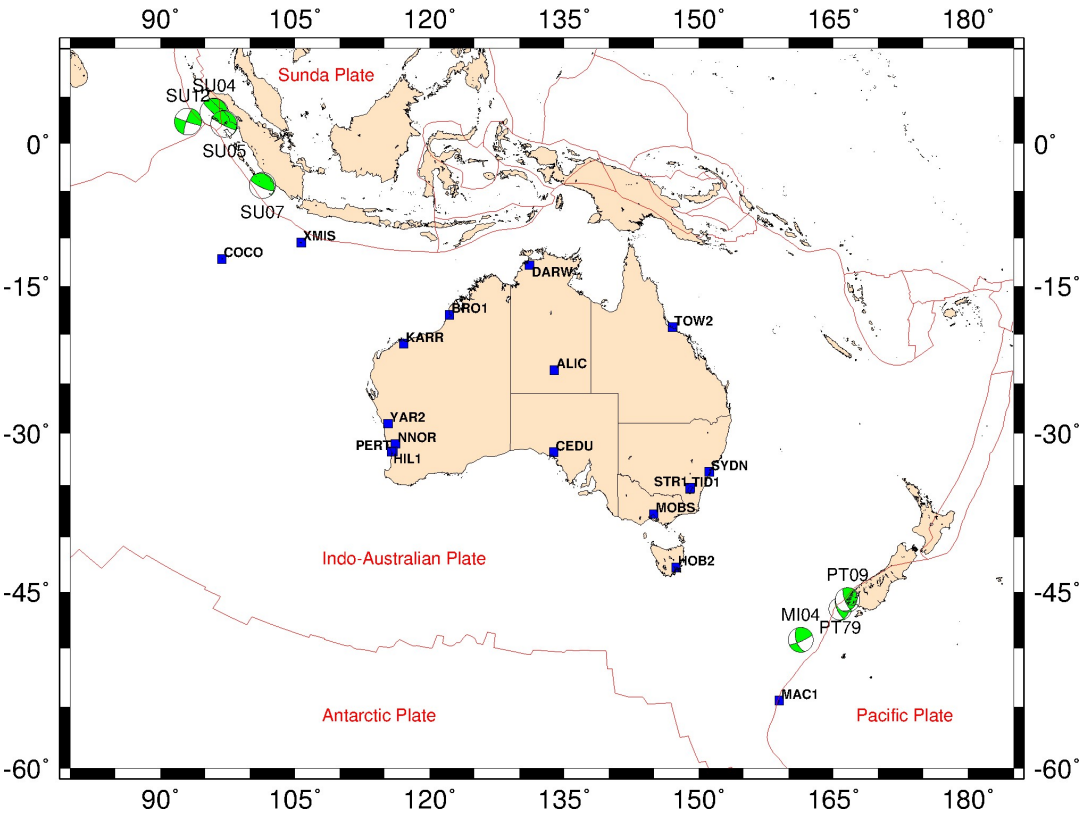

FIGURE 4.1: Indo-Australian tectonic plate setting including the focal mechanisms of the earthquakes investigated in this study (the two digits in the EQ label reflect the year of occurrence), Australian GPS sites are shown as blue squares. Plate boundaries are in red (Bird, 2003).

geometry and mechanism of the fault failure (strike direction, dip, rake, length, location). Geodetic point positioning systems, such as GPS, can provide time series of site locations suitable to monitor crustal dynamics in space and time (Bock and Melgar, 2016). Combined with geodetic observations, viscoelastic modelling of postseismic deformation provided insights into the rheological structure of the mantle and asthenosphere. Tregoning et al. (2013) assessed the global horizontal deformation field of 15 great earthquakes ($M_W > 8.0$) over the period 2000.0-2011.0 and the postseismic deformation observed in a subset of Australian GPS time series, but only presented results for the horizontal coordinate components. Watson et al. (2010) studied the vertical deformation of the 2004 Macquarie Island event at the MAC1 site, showing substantial vertical deformation at this near-field site, but did not consider vertical deformation at other locations further north.

Postseismic surface deformation changes the surface trajectory of a site relative to its pre-earthquake velocity, which if un-modelled in the GPS time series can bias geophysical interpretation that otherwise assumes secular motions (Altamimi et al., 2016; Hearn, 2003). In the realisation of geodetic reference frames, like the International Terrestrial Reference Frame (ITRF), the GPS time series are considered representative of observed surface motion and reflecting that motion in models can

be challenging given often poorly constrained fault parameters (Hearn et al., 2013). Poorly constrained fault parameters are sometimes caused by the complexity of the fault geometry or the remote location (and limited observation) of the earthquake event. Here we define transient motion as a residual signal which is non-periodic and non-secular (e.g. Bedford and Bevis, 2018; Walwer et al., 2016). Un-modelled deformations affect the accuracy of the terrestrial reference frame, which is constructed from Very Long Baseline Interferometry (VLBI), Satellite Laser Ranging (SLR), Global Navigation Satellite Systems (GNSS) and Doppler Orbitography and Radiopositioning Integrated by Satellite (DORIS) observations. Vertical postseismic deformations, if identified, would need to be considered to meet the Global Geodetic Observing System requirements of an accurate and reliable reference frame at the 1-millimetre level with the desired goal of stability of 0.1 millimetres per year (Blewitt, 2015; Gross et al., 2009).

Globally, the dominant driver of vertical land motion over centuries to millennia is glacial isostatic adjustment (GIA). Predictions of GIA-induced vertical land motion from different GIA models show discrepancies at the level of up to a few millimetres per year globally (e.g. Ostanciaux et al., 2012), but the magnitude of the signal across the Australian landmass is in the range of ± 0.5 mm/yr (Riddell et al., 2020). In contrast, current GPS observations, spanning 15 years at a dozen permanently operating sites in Australia suggest that the continent is subsiding at the rate of ~ 1.0 mm/yr (Altamimi et al., 2016; Burgette et al., 2013; King et al., 2012; Santamaría-Gómez et al., 2012; Schumacher et al., 2018). Pfeffer et al. (2017) compared land motion measured as a difference between altimetry and tide gauge observations with predicted land motion from surface mass loading and present day ice-mass changes showing significant disagreement at the level of 1-2 mm/yr, again suggesting increased subsidence around the Australian coastline from observations compared to models. Pfeffer et al. (2017) attributed the difference between observed and predicted rates of land motion to be linked to an assumption of continental tilt and dynamic topography (e.g. Heine et al., 2010; Sandiford, 2007), which supports their finding of greater uplift rates in southeast Australia. These differences between geodetic measurements and GIA models have, thus far, not been clearly attributed to a geophysical origin or systematic error (Riddell et al., 2020), but broad-wavelength deformation, such as far-field postseismic motion could be a contributor.

In this chapter, we investigate non-linear deformation induced by a selection of recent and historic earthquakes, taking into consideration far-field effects from large plate boundary earthquake events in the Australian region. Our focus is on the thus-unexplored vertical component but we also consider the horizontal components of deformation. In this Chapter we consider a representative selection of recent large earthquakes in various locations in the Australian region (northwest and southeast of Australia). Time series from GNSS sites in the Australian AuScope network over the period 2000.0-2019.0 are used (Figure 4.1, see also Table C.1). We further extend

the study backward in time to consider the effects of large earthquakes pre-GPS on present-day deformation, based on two events south of New Zealand.

4.2 Recent earthquakes and observed deformation in the Australian region

To address the question of deformation of the Australian continent from far-field events we select seven representative events, detailed in Table 4.1 and their locations shown in Figure 4.1. We do not attempt to consider all events that have occurred in the geodetic period, rather we consider some of the most significant plate boundary earthquakes over the time period 2004.0 – 2013.0. This time period allows us enough data span and spatial density of GPS observations before and after each earthquake to define changes in surface velocity associated with each earthquake. In the following sections, we briefly detail each earthquake.

TABLE 4.1: Details and references for earthquake parameters

Earthquake	Name	Latitude	Longitude	Date	Magnitude (M_W)	Source of earthquake fault slip information
Puysegur Trench, New Zealand	PT79	46.57°S	165.73°E	12 Oct 1979	7.4	(Anderson et al., 1993)
Macquarie Ridge	MI04	49.84°S	161.38°E	23 Dec 2004	8.1	(Watson et al., 2010)
Sumatra-Anderman	SU04	3.29°N	95.98°E	26 Dec 2004	9.3	(Banerjee et al., 2007)
Northern Sumatra	SU05	2.08°N	99.11°E	28 Mar 2005	8.6	(Banerjee et al., 2007)
Southern Sumatra	SU07	4.44°S	101.37°E	12 Sep 2007	8.5,7.9	(Konca et al., 2008)
Puysegur Trench, NZ (Dusky Sound)	PT09	45.76°S	166.56°E	15 Jul 2009	7.8	(Beavan et al., 2010b)
Northern Sumatra	SU12	2.31°N	93.06°E	11 Apr 2012	8.6,8.2	(Duputel et al., 2012; Yue et al., 2012)

4.2.1 Puysegur Trench 1979 & 2009 (PT79, PT09)

The M_W 7.8 2009 event occurred off the west coast of the South Island of New Zealand (Figure 4.1) on 15 July at a depth of 12 km. The earthquake occurred along the boundary of the Indo-Australian and Pacific plates and was the result of shallow thrust faulting. Faulting along this margin is accommodated by oblique convergence at the Puysegur Trench as the Indo-Australian Plate subducts beneath the Pacific plate (Beavan et al., 2010b; Hayes et al., 2009; Hayes et al., 2017). Estimates of fault depth, orientation and location suggested that the slip occurred on the subduction thrust interface between the Indo-Australian and Pacific plates (Hayes et al., 2017). Maximum slip estimates are 5-6 m over a subduction interface patch of 80 by 50 km (Beavan et al., 2010b).

On 12 October 1979 a M_W 7.4 event (Webb and Lowry, 1982) occurred in a similar location under similar subduction circumstances to the 2009 event (Figure 4.1), showing active subduction on an east-dipping thrust with a reverse faulting mechanism (Anderson et al., 1993). Approximately 110 km separates the surface location of the 2009 and 1979 epicentres. The 1979 event predates the commencement of

the continuous GPS record in Australia (in 1995) by approximately 17 years and the VLBI record by three years.

4.2.2 Macquarie Ridge 2004 (MI04)

On 23 December 2004, a M_W 8.1 earthquake occurred within the Indo-Australian Plate on the Macquarie Ridge (Figure 4.1). This event was the result of a rupture along a shallow left-lateral south-southeast strike-slip fault with approximate dimensions of 140 km x 20 km (length x width) (Hayes et al., 2017). Watson et al. (2010) provide a set of fault parameters derived using coseismic estimates from GPS and seismic locations. These were then refined by Tregoning et al. (2013) using an updated slip inversion and then further refined by King and Santamaría-Gómez (2016).

4.2.3 Sumatra-Anderman 2004 (SU04)

Three days after the MI04 event, on 26 December 2004, one of the largest earthquakes on record (M_W 9.3) occurred along the intersection of the India plate and the Burma microplate, rupturing along a zone 1300 km in length. The event was as a result of thrust faulting (Hayes et al., 2017). Fault rupture parameters are used from Banerjee et al. (2007) in a multi-block rupture model.

4.2.4 Northern Sumatra 2005 (SU05)

On 28 March 2005, a M_W 8.6 earthquake occurred 160 km to the south of the SU04 epicentre (Figure 4.1) as a result of thrust faulting along the interface of the Australian and Sunda plates (Hayes et al., 2017). The event had a maximum slip of $\sim$12 m along a 360 km by 200 km (length x width) fault patch (Banerjee et al., 2007). This earthquake is likely to have been the result of stress changes following the SU04 event (Hayes et al., 2017).

4.2.5 Southern Sumatra 2007 (SU07)

The M_W 8.5 event on 12 September 2007 occurred along the offshore plate boundary of the Australian and Sunda plates as a result of shallow thrust faulting (Hayes et al., 2017). Twelve hours later a M_W 7.9 event followed in the same area with similar mechanism. Maximum slip of $\sim$8 m was modelled on a fault patch of 250 km by 170 km (length x width) (Konca et al., 2008) for the combined event. These events occurred further south east along the Australian and Sunda plate boundary, closer to the Australian mainland compared to the other Sumatran events considered in Figure 4.1 and are considered in a combined fault model.

4.2.6 Northern Sumatra 2012 (SU12)

Two large strike-slip intraplate earthquakes, separated by 200 km, occurred as a sequence on 11 April 2012 with moment magnitudes M_W 8.6 and 8.2 in the oceanic

lithosphere of the Cocos Basin (Duputel et al., 2012). The location is represented as a single event (SU12) in Figure 4.1. The initial M_W 8.6 mainshock represents a complex four-fault structure with large slip (20-30 m) (Yue et al., 2012). Focal mechanism solutions are consistent in indicating that each of these events could have occurred as the result of left-lateral slip on a north-northeast striking fault or right-lateral slip on a west-northwest-striking fault (Hayes et al., 2017), and are considered here as a combined fault model.

4.2.7 Australian intraplate earthquakes

The seismic cycle and strain rates provide important information regarding the implications for intraplate seismicity and stresses (Trubienko et al., 2013).

The data used to infer neotectonic structures presented in Clark et al. (2014) suggests that the primary cause for ongoing deformation of the Indo-Australian Plate is an active response to distant plate boundary interactions. With ongoing changes at the plate margins, the Australian continent will continue to deform at some level in response to plate boundary forces (Hillis et al., 2008; Sandiford et al., 2004; Tregoning et al., 2013), also with series of intraplate events occurring in specified seismic zones (e.g. Dentith and Featherstone, 2003; Revets et al., 2009; Sandiford and Egholm, 2008). An understanding of the plate boundary events is therefore critical for interpreting transient present-day surface deformation as observed by GPS. We now investigate these events using the geodetic record as well as co- and postseismic modelling with a simplistic one-dimensional earth structure to assess ongoing deformation.

4.3 Data & Methods

4.3.1 GPS time series

Following the methods outlined in Riddell et al. (2020), the GPS data over the period 2000.0-2019.0 was sourced from the Geoscience Australia GNSS data archive (`https://gnss.ga.gov.au/`), and daily point positions were estimated using GIPSY v6.3 software with clock and orbit products (repro2) from the Jet Propulsion Laboratory (JPL) (Bertiger et al., 2010; Zumberge et al., 1997). Further details describing the processing, including outlier and offset detection and removal is described in Riddell et al. (2020). The daily GPS series were aligned to ITRF2014 (Altamimi et al., 2016).

Elastic deformations due to atmospheric loading were removed from the time series using the Modern-Era Retrospective analysis for Research and Applications, Version 2 (MERRA2) gridded products (Gelaro et al., 2017), as well as deformations due to terrestrial land water storage, computed using land water storage pressure from the

numerical weather model MERRA2 (Reichle et al., 2017), and non-tidal ocean loading from ocean bottom pressure fields of the Max-Planck-Institute for Meteorology Ocean Model (MPIM; Jungclaus et al., 2013). These estimates of elastic deformation were downloaded from the International Mass Loading Service (Petrov, 2015) in the Centre of Figure frame (Blewitt, 2003), which is appropriate for correcting non-secular changes in coordinate time series in the ITRF (Dong et al., 2003). We note that the earlier segments of the GPS time series (prior to 2005) are especially sensitive to receiver changes. Offsets due to equipment and firmware changes are estimated and removed simultaneously with a linear and seasonal (solar annual and semi-annual) model. The estimated offset times and magnitudes are provided in the Supporting Information (Table C.2).

4.3.2 Coseismic modelling

The expected elastic coseismic deformation for each earthquake is computed on a spherically layered Earth with STATIC1D (Pollitz, 1996). An Earth model with 69 layers defined by the Preliminary Earth Reference Model (PREM) (Dziewonski and Anderson, 1981) was used with a maximum spherical harmonic degree of 1500, sufficient to resolve deformation with a spatial scale of approximately 13 km. Regions radially deeper than 3300 km were considered as an incompressible fluid and the ocean in PREM was replaced by crust. Fault slip parameters from the references given in Table 4.1 are used to derive estimates of coseismic slip.

Modelled coseismic slip displacements were compared to coseismic offsets (in 3D) computed using daily GPS data. The instantaneous coseismic offset magnitude is calculated using two weeks of GPS data either side of the time of the earthquake, fitting a linear trend with a Heaviside jump using ordinary least squares. Recognising that white noise dominates over short periods in GPS time series we take the formal uncertainties to represent the offset uncertainty. We use two weeks of data to calculate the coseismic offset magnitude as a compromise between biases caused by postseismic relaxation, daily variability and noise correlation (e.g. King and Santamaría-Gómez, 2016; Watson et al., 2010). Similar results are found with estimating the coseismic offset using only one week either side of the event. Where the modelled coseismic displacements disagree with the computed offsets, we scale the slip model accordingly by adopting the modified result that retains agreement with the seismic location and fault geometry of the event, while most closely fitting the GPS (e.g. Jiang et al., 2018; King and Santamaría-Gómez, 2016). An arbitrary value of 1.5 for the weighted root mean square (WRMS) is chosen as acceptable. The site selection for constraining the coseismic model was based on data availability, data quality and distance from the earthquake epicentre.

4.3.3 Postseismic modelling

Near-field deformation after an earthquake is a response to the combination of co-seismic displacement followed by viscoelastic relaxation and fault after-slip which can be difficult to separate (Bedford et al., 2016; Wang et al., 2012). Afterslip is motion at depth along the fault face causing local deformation, approximately within 200 km of the earthquake epicentre (Klein et al., 2016; Wang et al., 2012) and is theoretically small outside this distance (Hearn, 2003). We assume that far-field deformation does not contain a signal from after-slip, given most of our GPS locations are more than 500 km from the earthquake epicentres. Evidence of minimal afterslip within the far-field for an earthquake event of M_W 7 is provided by Freed et al. (2007) and for events of magnitude M_W 8 and greater by Klein et al. (2016). We therefore only model viscoelastic postseismic processes.

We make use of the VISCO1D (Pollitz, 1992; Pollitz, 1997) code to compute the viscoelastic deformation with a linear bi-viscous (Burgers) rheology. VISCO1D computes surface displacements generated by an earthquake using a symmetric spherically layered elastic-viscoelastic Earth model. The surface displacements are controlled by fault parameters (latitude and longitude of lower fault corner, strike, rake, dip, slip, length, and the depth of the upper and lower fault edges); as well as the relative thicknesses and rheological properties of the chosen layers. Following King and Santamaría-Gómez (2016), multiple versions of the model were run with varying thickness of an elastic lithosphere ranging from 30-130 km, asthenosphere thickness and effective viscosity (0-190 km; $1x10^{17}$ - $5x10^{21}$ Pa s), and upper mantle thickness and effective viscosity (320-670 km; $2x10^{18}$ - $5x10^{21}$ Pa s). Predictions from VISCO1D can be sensitive the layers of the lower mantle (pers. comm. G. Nield February 2020). We include a lower mantle with 30 layers with bulk and shear modulus values of 44 x 10^{10} Pa and 22 x 10^{10} Pa respectively. This difference in handling the lower mantle did produce different results to those without a detailed lower mantle such as were published by Tregoning et al. (2013). An example earth model (readable by VISCO1D v3) is provided in Appendix C.2. The values of density, bulk modulus and shear modulus were taken from PREM and depth-averaged for each layer in our model. Gravity was taken into consideration during the computations.

We use GPS daily time series to assess the predicted surface deformation from VISCO1D and select the best fit model based on the chi-square per degree of freedom statistic and the lowest value of the standard deviation from an ordinary least squares fit. The best fit model is chosen independently for the horizontal (east and north combined) and vertical components per site.

4.4 Results

Here we present results of the computed coseismic offsets for the earthquakes in Table 4.1, followed by the postseismic deformation. The Sumatran events that occurred in 2004, 2005, 2007 and 2012 are presented as a compilation of observed and modelled deformation, whereas all other events are presented singularly.

4.4.1 Macquarie Ridge 2004

4.4.1.1 Coseismic displacements

Site selection is limited by the availability of GPS data before 2004, with eight far-field sites in southeast Australia with data available from 2000.0 onwards (Table 4.2). The largest coseismic offset of 5.98 ± 1.33 mm is in the east component of HOB2 (Hobart), which is the closest site on the Australian continent that sits in the far-field of the MI04 event (Figure 4.1; Table 4.2). Offsets in the vertical components of sites in southeast mainland Australia range from -3.49 ± 2.42 mm to 1.89 ± 2.65mm. The uncertainties for the up-component offsets are large for the majority of sites, where only three of the vertical offsets are significant at one-sigma (Table 4.2). Both the horizontal and vertical offsets are comparable to those calculated by STATIC1D, which provides confidence that the fault geometry parameters taken from Watson et al. (2010) (Table 4.1) are sufficient and that the model does not require scaling for this study. The WRMS value of the modelled coseismic offsets are comparable to those from Tregoning et al. (2013) and King and Santamaría-Gómez (2016). Our coseismic estimates compare well with those of Watson et al. (2010), with HOB2 being displaced by ∼5 mm to the east.

TABLE 4.2: Macquarie Island 2004 (MI04) earthquake coseismic offsets at GPS sites ordered by distance, uncertainties are one-sigma. Bold values are statistically significant at one-sigma.

Site	Distance from MI04 eq (km)	N offset (mm)	E offset (mm)	U offset (mm)
MAC1	544	**4.01 ± 0.99**	0.74 ± 1.48	**2.80 ± 1.86**
HOB2	1322	0.20 ± 1.40	**5.98 ± 1.33**	-1.08 ± 1.95
MOBS	1861	1.35 ± 1.51	**4.20 ± 1.38**	**-2.18 ± 1.68**
TID1	1887	**1.10 ± 0.77**	**2.95 ± 2.01**	1.58 ± 2.12
TIDB	1887	**1.11 ± 0.59**	**3.90 ± 3.41**	1.89 ± 2.65
STR1	1893	**1.53 ± 0.71**	**3.95 ± 1.04**	-0.42 ± 1.85
SYDN	1963	0.60 ± 2.69	**3.17 ± 2.26**	3.38 ± 3.60
CEDU	3004	**1.45 ± 0.79**	**1.75 ± 0.93**	**-3.49 ± 2.42**

4.4.1.2 Postseismic displacements

We build on the investigation by Tregoning et al. (2013) of viscoelastic postseismic relaxation occurring after the MI04 earthquake. Our GPS time series adds eight years

to those analysed by Tregoning et al. (2013) (end date of 2019.0 compared to 2011.0), we make use of a precise point positioning approach rather than a double differenced solution, and our solutions are aligned to the ITRF2014 reference frame rather than ITRF2008. We also attempt to account for short-term temporal variability by removing surface mass loading caused by atmospheric, hydrologic and non-tidal sources.

Figure 4.2 shows the coordinate time series for three sites in SE Australia over the period 2000.0–2019.0, encompassing the MI04 event. The velocity for the period prior to the earthquake (2000.0–2004.9) was removed from the entire time series to highlight any postseismic change in velocity. The velocity prior-to and following the earthquake are calculated using Hector software (Bos et al., 2013), adopting a power-law plus white (PLW) noise model including estimates of linear, annual and semi-annual terms and coseismic offset. The linear velocity post-earthquake is plotted in Figure 4.2 as a blue dashed line.

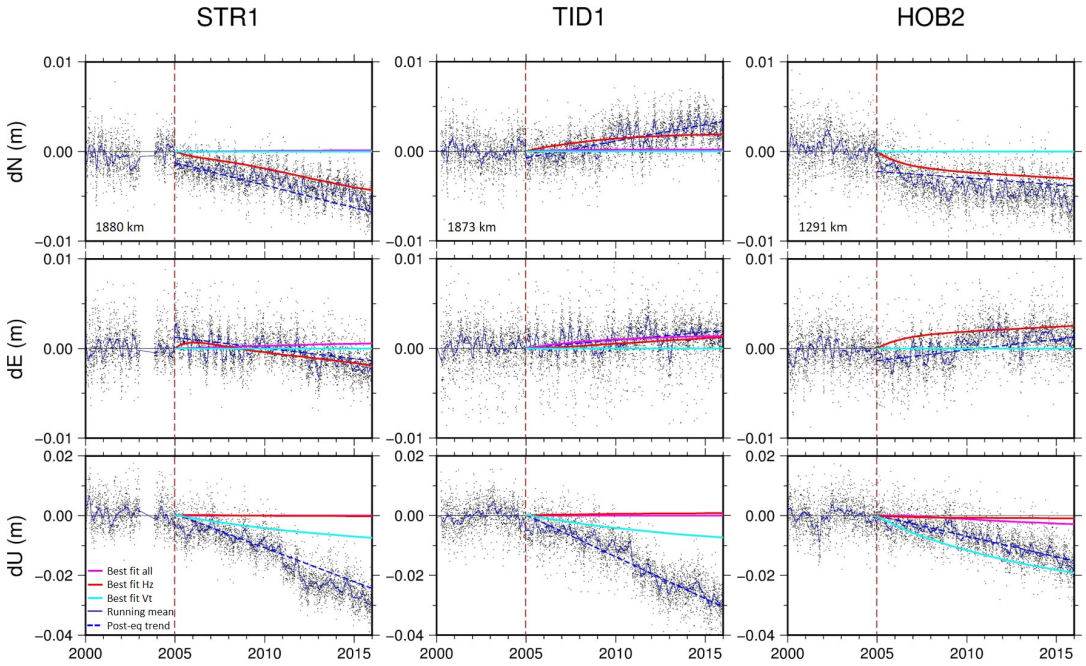

FIGURE 4.2: GPS time series at Mt Stromlo (STR1), Tidbinbilla (TID1), and Hobart (HOB2) after removing the trend computed over the pre-earthquake period 2000.0-2004.9. A 100-day running mean is shown in solid blue. Blue dashed line is the estimated linear velocity post-earthquake. Red is the best fitting viscoelastic model for the horizontal components, cyan is the best fitting visco model for the vertical component and magenta is the best fitting visco model for all components. The dashed vertical line indicates the date of the Macquarie Island earthquake (23 December 2004). The value in the bottom left of the upper panels is the distance of each site from the earthquake surface epicentre. Coseismic offsets have been removed.

The site time series in Figure 4.2 are shown as they experienced the largest change in velocity following the MI04 event based on our analysis. We have chosen to use TID1 instead of TIDB as the time series is of slightly better quality (smaller scatter

and the difference between the time series shows no distinct trends). We distrust the Melbourne (MOBS) time series over this time period as it shows substantially different behaviour compared to the other sites (Figure C.1), presumably due to the short pre-MI04 time series making the pre-MI04 velocity unreliable and/or being affected by substantial near-field multipath (Moore et al., 2014). Tregoning et al. (2013) also cover this event and we return to this in the discussion.

We compared model predictions from VISCO1D with the time series/velocities for each of the GPS sites. The coloured lines in Figure 4.2 represent the optimal models where red is the best fitting viscoelastic model for the horizontal components, cyan is the best fitting viscoelastic model for the vertical component, and magenta is the best fitting viscoelastic model that is a compromise between the fit to each component (north, east, up). Table 4.3 contains the parameters of the viscoelastic models that best fit the GPS results for each of the earthquakes considered in Table 4.1.

TABLE 4.3: Parameters of best fitting viscoelastic models for horizontal and vertical components of the sites for each earthquake. [horizontal | vertical]

Site	Elastic thickness (km)	Asthenosphere depth (km)	Asthenosphere viscosity (10_{19} Pa s)	Upper mantle viscosity (10_{19} Pa s)
		MI04		
STR1	50 | 70	80 | 220	0.01 | 0.05	5 | 1
TID1	50 | 70	80 | 220	0.05 | 0.05	50 | 1
HOB2	50 | 90	60 | 220	5 | 0.5	4 | 1
		SU04		
KARR	50 | 70	80 | 220	0.1 | 0.05	50 | 1
YAR2	90 | 70	220 | 220	0.5 | 0.05	30 | 1
DARW	50 | 50	220 | 80	0.5 | 0.01	100 | 500
		PT09		
SYDN	50 | 70	80 | 220	0.01 | 0.5	10 | 1
TID1	90 | 50	100 | 220	5 | 0.05	4 | 1
MOBS	110 | 110	140 | 220	0.01 | 0.01	100 | 500
HOB2	90 | 90	220 | 120	1.2 | 0.01	1.4 | 10

4.4.1.2.1 Horizontal

Table 4.4 shows the change in velocity of sites in Australia, noting that the northern sites are likely to also contain a postseismic signal from the SU04 event that occurred 3 days after the MI04 event. The decay function in Hector can be set separately and so we look at the full time series (up to 2019.0) following each event. The changes in velocity of the north and east components for the sites in SE Australia (HOB2, MOBS, TIDB, TID1, STR1, CEDU) following the MI04 earthquake are less than 0.5 mm/yr (Table 4.4) with the exclusion of the site on Macquarie Island (MAC1). Our time series analysis for HOB2 agrees with that of Tregoning et al. (2013) with a reduced

TABLE 4.4: Difference in GPS site velocities calculated before and after the Macquarie Island 2004 earthquake. Uncertainties are one-sigma. Pre-earthquake trend calculated over the period 2000.0 – 2004.9, and post-earthquake trend calculated over the period 2004.9 – 2019.0. Sites are ordered by distance from the earthquake. Bold values are statistically significant at one-sigma.

Site	Distance from MI04 eq (km)	ΔN trend (mm/yr)	ΔE trend (mm/yr)	ΔU trend (mm/yr)
MAC1	544	**-2.45 ± 0.21**	**-1.77 ± 0.18**	**1.66 ± 0.49**
HOB2	1322	**-0.37 ± 0.23**	**0.23 ± 0.15**	**-1.87 ± 0.48**
MOBS	1861	-0.21 ± 0.38	**-0.34 ± 0.28**	**0.57 ± 0.48**
TID1	1887	**0.33 ± 0.23**	0.07 ± 0.15	**-2.40 ± 0.42**
TIDB	1887	0.21 ± 0.23	0.13 ± 0.16	**-2.08 ± 0.44**
STR1	1893	**-0.38 ± 0.36**	**-0.28 ± 0.26**	**-2.55 ± 0.48**
CEDU	3004	0.18 ± 0.23	**-0.20 ± 0.20**	**-0.96 ± 0.71**
TOW2	3574	**1.51 ± 0.21**	**0.61 ± 0.21**	**-1.62 ± 0.53**
PERT*	4166	0.05 ± 0.36	**-0.90 ± 0.34**	**2.27 ± 0.76**
NNOR*	4198	**0.30 ± 0.26**	**-0.40 ± 0.22**	-0.02 ± 0.80
YAR2*	4397	**0.70 ± 0.29**	-0.16 ± 0.23	**-3.15 ± 1.06**
DARW*	4820	0.49 ± 0.50	-0.13 ± 0.50	**2.77 ± 1.61**
KARR*	4898	**0.58 ± 0.28**	**-0.36 ± 0.19**	**-2.82 ± 0.65**
COCO*	6791	**3.17 ± 0.38**	**-3.29 ± 0.31**	**-3.99 ± 0.70**
*these results may be confounded by the SU04 event				

northward trend. Figure 3 of Tregoning et al. (2013) shows a southerly postseismic velocity relative to the inter-seismic movement in the north component at TIDB, whereas our series for TID1 show northerly motion (as does our series for TIDB). The difference between our TID1 time series at the TIDB time series of Tregoning et al. (2013) may be explained by changes in equipment hardware and firmware. TIDB and TID1 share the same antenna but have different receivers that have been changed and updated at different times. Our velocity estimates for TIDB and TID1 differ by less than 0.1 mm/yr, which provides confidence in our analysis.

4.4.1.2.2 Vertical

From Table 4.4, the observed change in the vertical component is larger than ±1 mm/yr for most sites over the period 2004.9 – 2019.0. STR1, TIB1, and HOB2 all show uplift in the 4.5 years prior to the MI04 earthquake, but following the event, the series each shows subsidence over the next 14.5 years. The postseismic change in vertical velocity is 1.5-3.5 mm/yr for the sites with a consistent shift towards subsidence after the MI04 earthquake. The largest change in vertical velocity (-3.24 mm/yr) is observed at STR1 where the pre-earthquake velocity changes from 1.97 ± 0.50 mm/yr to 1.27 ± 0.21 mm/yr post-earthquake. No postseismic deformation model fits the GPS well in the vertical and we return to this in the discussion.

4.4.2 Sumatran events

Given that the Sumatran events cluster closely together in time and space it is not possible to independently analyse postseismic deformation due to each earthquake. Instead, we present the combined results of the events that occurred in northern and southern Sumatra over the period 2004 – 2012. Following the previous methodology, the coseismic offsets are calculated with STATIC1D for each earthquake and then compared to the observed offset in the GPS time series. Then the postseismic deformation is modelled for each earthquake individually (SU04, SU05, SU07, SU12), with the total accumulated displacement for each model setup compared to the GPS time series to identify the best-fit viscoelastic postseismic model.

4.4.2.1 Coseismic displacements

We show the estimated coseismic displacements in Table 4.5 at the Australian GPS sites located on islands off the NW shelf, Cocos Island (COCO) and Christmas Island (XMIS), as well as sites on mainland Australia (Figure 4.1). The only available GPS data in the NW Australian region, following the 2004/2005 earthquakes in the Sumatran region, are from COCO and Karratha (KARR, see Table C.2 and Figure 4.1). For the modelling of the coseismic displacements of the SU04 event we used the total slip displacement of five sub-sources over ten rupture planes from Banerjee et al. (2007) obtaining an WRMS of 0.62 mm. We also explored using instead a scaled version of the USGS solution but the smallest WRMS derived was 1.13 mm and so we adopted the Banerjee et al. (2007) solution. The large uncertainties on the coseismic offsets are due to noisy time series in the mid-2000's due to receiver tracking and scintillation issues (e.g. Conker et al., 2003), and we return to this in the discussion. Coseismic offsets at the available sites across Australia are shown in Table 4.5 for each of the Sumatran earthquakes considered.

TABLE 4.5: Coseismic offsets at GPS sites for the 2004 Sumatra-Anderman, 2005 northern Sumatra, 2007 southern Sumatran and 2012 northern Sumatran events. Uncertainties are one-sigma. Bold values are statistically significant at one-sigma.

Site	Distance from eq (km)	N offset (mm)	E offset (mm)	U offset (mm)
		SU04		
COCO	1709	1.96 ± 2.12	**1.54 ± 1.30**	0.71 ± 1.72
KARR	3492	1.35 ± 2.05	0.67 ± 0.76	1.16 ± 2.44
YAR2	4061	**1.39 ± 1.02**	**2.25 ± 0.06**	-0.24 ± 2.11
DARW	4196	3.04 ± 3.95	0.70 ± 1.76	**-3.43 ± 3.14**
HIL1	4325	**2.42 ± 1.78**	**2.41 ± 2.15**	-0.24 ± 2.38
PERT	4330	**1.34 ± 1.07**	**2.00 ± 0.87**	**-3.66 ± 1.94**
CEDU*	5402	**1.02 ± 0.74**	**1.33 ± 0.41**	-5.97 ± 2.37

TOW2	5887	**3.01 ± 2.06**	**2.59 ± 2.10**	0.54 ± 1.89
STR1*	6636	**1.16 ± 0.82**	**3.53 ± 1.56**	-1.72 ± 1.92
TID1*	6637	**0.78 ± 0.70**	**3.19 ± 1.95**	0.89 ± 2.03
HOB2*	6869	1.54 ± 1.83	1.09 ± 2.00	1.05 ± 1.95
*these results may be confounded by the MI04 event				
		SU05		
COCO	1575	0.98 ± 3.13	**1.99 ± 1.24**	**2.59 ± 2.50**
KARR	3316	**4.27 ± 1.51**	0.01 ± 0.35	**-2.71 ± 1.56**
YAR2	3893	**3.04 ± 1.78**	0.99 ± 1.07	**-5.63 ± 2.63**
DARW	4035	**1.68 ± 1.08**	-1.12 ± 1.26	0.26 ± 2.30
NNOR	4112	**3.36 ± 0.99**	**0.87 ± 0.81**	**-3.56 ± 1.45**
HIL1	4160	**3.90 ± 1.34**	**2.43 ± 1.42**	-1.94 ± 2.65
PERT	4164	**3.54 ± 0.99**	**0.81 ± 0.44**	**-3.00 ± 0.98**
CEDU	5236	**2.59 ± 0.64**	**-1.23 ± 0.68**	**-2.90 ± 1.14**
TOW2	5735	1.37 ± 4.32	-0.89 ± 1.43	-0.92 ± 2.65
STR1	6479	**2.23 ± 0.42**	-0.53 ± 0.94	0.02 ± 1.66
TID1	6481	**2.57 ± 0.82**	**-1.92 ± 0.62**	**-3.17 ± 1.52**
HOB2	6714	**2.80 ± 1.09**	-0.47 ± 2.31	-0.37 ± 1.24
		SU07		
XMIS	810	**2.51 ± 1.79**	**3.72 ± 3.45**	-0.13 ± 1.7
COCO	984	**2.94 ± 1.52**	**2.28 ± 0.79**	-0.85 1.84
KARR	2475	**3.72 ± 0.88**	**1.94 ± 1.03**	**0.84 ± 0.81**
DARW	3357	**3.52 ± 0.50**	0.26 ± 0.51	**2.45 ± 1.83**
YAR2	3059	**3.45 ± 0.67**	**1.77 ± 1.42**	0.26 ± 0.99
NNOR	3284	**3.49 ± 0.74**	**1.37 ± 1.29**	-1.04 ± 1.32
HIL1	3335	**4.22 ± 0.66**	**2.25 ± 0.95**	**3.02 ± 1.55**
PERT	3339	**3.83 ± 0.97**	**1.99 ± 1.23**	0.58 ± 1.70
CEDU	4443	**3.18 ± 0.71**	**0.88 ± 0.47**	0.36 ± 0.65
TOW2	5072	**2.85 ± 0.54**	**-0.86 ± 0.65**	0.44 ± 1.33
STR1	5741	**2.86 ± 0.79**	0.17 ± 0.70	-0.74 ± 1.47
TID1	5742	**2.93 ± 0.96**	1.57 ± 1.75	0.38 ± 1.31
HOB2	5967	**2.56 ± 1.35**	0.57 ± 1.38	1.28 ± 1.65
		SU12		
COCO	1654	2.07 ± 3.95	**0.76 ± 0.76**	-0.70 ± 2.90
XMIS	1980	3.50 ± 3.67	-0.78 ± 3.67	0.81 ± 3.04
BRO1	3625	**2.75 ± 1.54**	**0.97 ± 0.74**	**-1.04 ± 1.37**
KARR	3847	**3.54 ± 0.98**	0.26 ± 0.83	**2.28 ± 1.34**
YAR2	4131	**2.15 ± 1.14**	**2.52 ± 1.65**	-0.39 ± 1.60
NNOR	4343	**3.31 ± 0.61**	0.62 ± 0.63	**2.48 ± 2.15**

HIL1	4383	**3.26 ± 0.53**	**1.08 ± 0.95**	**2.07 ± 0.92**
DARW	4434	-2.52 ± 3.47	-0.34 ± 1.24	0.18 ± 2.53
CEDU	5536	**2.24 ± 0.69**	**0.56 ± 0.52**	0.60 ± 1.01
TOW2	6105	**2.35 ± 0.82**	0.76 ± 1.05	**-2.71 ± 1.35**
STR1	6780	**1.92 ± 0.58**	0.74 ± 0.75	0.27 ± 1.24
TID1	6781	**1.54 ± 0.66**	0.02 ± 1.87	**-1.96 ± 1.59**
HOB2	6975	**0.80 ± 0.74**	0.42 ± 1.57	**2.16 ± 1.04**

Noting that the northern SU05 event occurred three months after the SU04 event, we modelled the event as a separate solution, and remove the estimated coseismic signal of the SU04 event from the GPS series before modelling the 2005 event. The calculated coseismic offsets for the SU05 event have a WRMS of 0.83 mm when compared to the GPS estimates. The coseismic model is used in the viscoelastic modelling without scaling. For this event we only consider the GPS sites at Darwin (DARW) and KARR to constrain the coseismic model. We do not use COCO time series to constrain the model because we are restricting the constraining sites to mainland Australia. Both sites show offsets in the north component, with the KARR offset greater than 4 mm (Table 4.5). KARR has a significant offset in the vertical component of -2.71 ± 1.56 mm.

For the sequence of events in southern Sumatra in 2007, we calculate the coseismic offsets at Australian sites that have available GPS data, again shown in Table 4.5. KARR and DARW are again used to constrain the coseismic model. All offsets for KARR in each of the three components are significant, and DARW has significant offsets in the north and up components. The fault rupture models of the two events from Konca et al. (2008) required a small amount of scaling of the slip magnitude for the WRMS value to be acceptable ($<$ 1.5 mm) and for the modelled coseismic displacement to align with the GPS offsets.

A simple fault rupture model was adopted to model the far-field deformation associated with the SU12 earthquake. As outlined in Section 4.2.6, there were two events within 24 hours separated by approximately 200 km. The fault rupture model is that from Yue et al. (2012) with five blocks, the first four blocks are for the earlier MW 8.6 event and the fifth block for the M_W 8.2 event that occurred 12 hours later. DARW and KARR are used to constrain the slip, without scaling and a resulting WRMS of 1.48 mm. The coseismic offsets at sites on the Australian plate, associated with the SU12 earthquake are given in Table 4.5. Most sites on mainland Australia, aside from DARW, show significant offsets in the north and up components.

4.4.2.2 Postseismic displacements

We plot the GPS time series and modelled viscoelastic postseismic deformation of the Sumatran events in Figure 4.3. All four events are combined in an attempt to

understand the long-term cumulative effects of postseismic deformation from multiple events that have occurred in the same region. The time series in Figure 4.3 is detrended relative to the pre-SU04 rate. The GPS velocities for the period prior to 2004, and the Sumatran earthquakes considered here are in Table C.4.

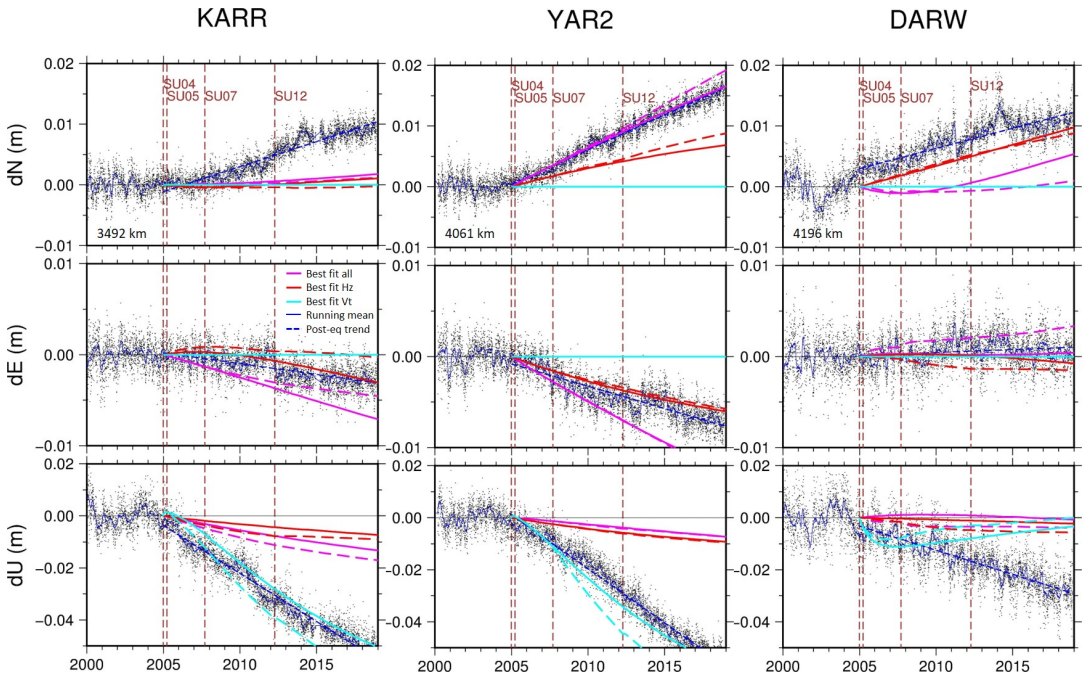

FIGURE 4.3: GPS time series at Karratha (KARR), Yarragadee (YAR2), and Darwin (DARW) after removing the trend computed over the pre-earthquake period for SU04 (2000.0–2004.9). A 100-day running mean is shown in blue. Blue dashed line is the estimated linear velocity post-earthquake. The solid lines of the viscoelastic models are for SU04 only, the dashed lines incorporate the combined response of all four Sumatran earthquakes. The brown dashed vertical line indicates the date of the earthquakes. Coseismic offsets have been removed.

Only three GPS sites on the Australian mainland have robust data available from 2000 onwards to enable the investigation of postseismic deformation following the SU04 event (Figure 4.3). We focus on those sites mainland Australia that are closest to the Sumatran events (and have available data), KARR, YAR2 and DARW. Even though these sites are located in the very far-field of the earthquake deformation field, changes in velocity at KARR, YAR2 and DARW are visible as a subsidence signal in Figure 4.3 (values in Table 4.6); we take these sites as being representative of the motion across NW Australia. The optimal model for all components is represented by a magenta line in Figure 4.3 where the solid line is the modelled postseismic deformation for SU04 only and the dashed line is the cumulative deformation from each of the four Sumatran events. Other than SU04, the remaining events have a subtle effect on the observed long-term deformation at each site (dashed line in Figure 4.3).

TABLE 4.6: Difference in GPS site velocities calculated before and after the Sumatra Anderman 2004 earthquake. Uncertainties are one-sigma. Pre-earthquake trend calculated over the period 2000.0 – 2004.9, and post-earthquake trend calculated over the period 2004.9 – 2019. Bold values are statistically significant at one-sigma.

Site	Distance from SU04 (km)	ΔN trend (mm/yr)	ΔE trend (mm/yr)	ΔU trend (mm/yr)
COCO	1709	**3.23 ± 0.75**	**-2.64 ± 0.39**	**-3.98 ± 0.94**
KARR	3492	**0.93 ± 0.42**	-0.33 ± 0.34	**-2.34 ± 0.84**
YAR2	4061	0.59 ± 1.25	**-0.33 ± 0.28**	**-2.53 ± 1.75**
DARW	4196	0.13 ± 0.52	-0.24 ± 0.51	**-2.14 ± 1.66**
HIL1	4325	**0.86 ± 0.52**	**-2.62 ± 0.67**	**5.37 ± 1.58**
PERT	4330	0.03 ± 0.36	**-0.92 ± 0.35**	**-2.57 ± 0.77**
CEDU*	5402	**0.50 ± 0.25**	-0.14 ± 0.23	-0.56 ± 0.79
TOW2	5887	**1.35 ± 0.31**	**0.72 ± 0.29**	**-1.46 ± 0.68**
STR1*	6636	0.31 ± 0.39	**-0.28 ± 0.26**	**-2.55 ± 0.48**
TID1*	6637	0.18 ± 0.25	0.11 ± 0.20	**-1.97 ± 0.52**
HOB2*	6869	**-0.59 ± 0.36**	**0.26 ± 0.25**	**-0.76 ± 0.57**
*these results may be confounded by the MI04 event				

4.4.2.2.1 Horizontal

The changes in velocity following the SU04 event are shown in Table 4.6 for each of the Australian GPS sites that have data from 2000 onwards to ensure that we capture the full extent of the cumulative postseismic displacement from each of the four Sumatran events across the Australian continent. The observed postseismic deformation of the east component is well matched by the modelled viscoelastic relaxation for each of the sites in Figure 4.3, and the observed deformation in the northern components is well represented at YAR2 and DARW, but not at KARR. The time series at KARR is subject to many hardware changes in the early part of the series which introduces uncertainty in the velocity estimation, suggesting that the change in trend pre- and post-earthquake could be unrealistic, with large uncertainty.

4.4.2.2.2 Vertical

The velocity changes in the vertical component following the Sumatran events are in Table 4.6 for each of the Australian GPS. The dominant change in velocity is subsidence following the SU04 event with the sites in NW Australia showing a change in trend for the vertical component ranging between -2 to -2.5 mm/yr (Table 4.6), which is also visible in Figure 4.3. The observed postseismic deformation at KARR and YAR2 is well modelled by the viscoelastic response, whereas DARW is not. The DARW postseismic model suggests a gradual return to pre-SU04 trend which is not replicated by the GPS observations.

4.4.3 Puysegur Trench 2009 (PT09)

4.4.3.1 Coseismic displacements

The coseismic offsets estimated at nearby Australian GPS sites due to the 2009 M_W 7.8 Puysegur event are listed in Table 4.7. Significant offsets are observed in sites for the north and up components for some sites, although the magnitude of the offset does not show a clear linear relationship with distance from the location of the earthquake. This implies that the axis of the lobes of the deformation are oblique to a transect taken from south to north through the sites.

TABLE 4.7: Puysegur Trench 2009 earthquake coseismic offsets at GPS sites, uncertainties are one-sigma. Bold values are statistically significant at one-sigma.

Site	Distance from PT09 (km)	N offset (mm)	E offset (mm)	U offset (mm)
MOBS	1553	**0.98 ± 0.66**	**0.96 ± 0.69**	**1.54 ± 1.33**
STR1	1861	**1.74 ± 0.56**	0.42 ± 4.83	0.19 ± 2.85
SYDN	1868	0.33 ± 2.15	2.78 ± 5.13	0.50 ± 2.85
HOB2	1868	1.21 ± 1.79	1.73 ± 2.94	**-3.13 ± 2.53**
TID1	1982	**2.73 ± 0.79**	3.89 ± 5.00	**3.26 ± 2.30**

The coseismic offsets in the horizontal component are all positive, indicating a shift of the sites north-east, whereas the vertical coseismic offsets are mixed with significant displacements (at one-sigma) at HOB2 with a subsidence of -3.13 ± 2.53 mm, and the remainder of the sites suggesting uplift of 1.54 ± 1.33 mm at MOBS and 3.26 ± 2.30 mm at Tidbinbilla (TID1) (Table 4.7). Insignificant coseismic offsets in the east component are observed at the majority of GPS sites on the Australian continent as a result of the PT09 event, where the uncertainty of the east component is large ($>$ 2 mm) due to noisy time series at this time. The offsets observed in the GPS series for all components are comparable to those calculated with STATIC1D, with a WRMS of 1.17 mm. Out of interest, we also compared the coseismic offsets for several sites in New Zealand and these are detailed in Appendix C.1.

4.4.3.2 Postseismic displacements

Time series of the Australian GPS sites after the M_W 7.8 Puysegur event are shown in Figure 4.4, where the estimated pre-earthquake velocity (2006.0-2009.5) is removed from the full time series. There magnitude of the changes does not vary simply with distance from the rupture. The sites are ordered in Figure 4.4 from north (left) to south (right) and the coloured lines match the previous description of the optimal models for the components and combined results. We note that there is some residual MI04 deformation present in the time series, but it is largely linear and hence

removed when we subtract pre-earthquake velocity from our time series. The rheological structure of the optimal model for the PT09 event is similar to that for the MI04 optimal model (Table 4.3).

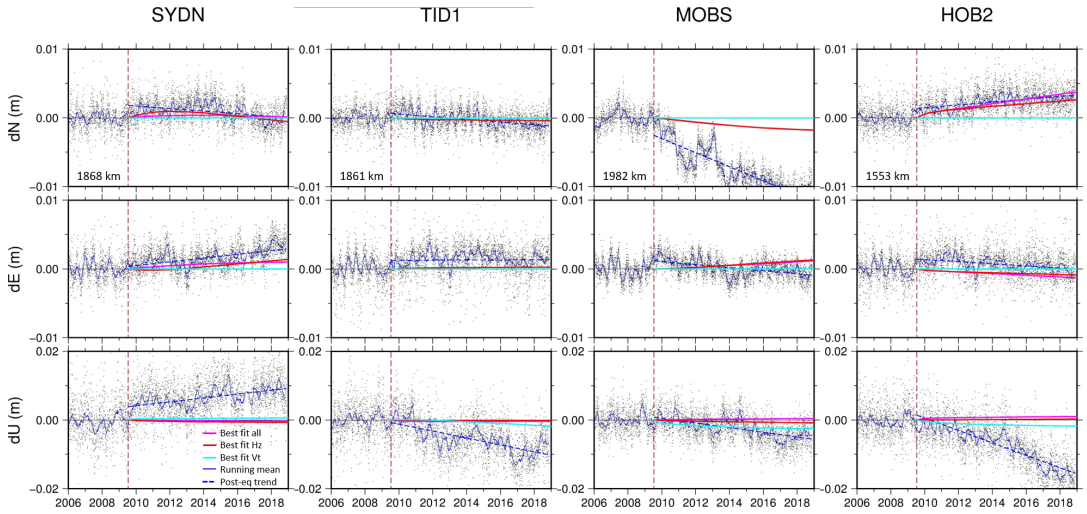

FIGURE 4.4: GPS time series at Sydney (SYDN), Tidbinbilla (TID1), Melbourne (MOBS), and Hobart (HOB2), detrended over the pre-earthquake period (2006.0-2009.5). 100 day running mean is plotted in blue. Blue dashed line is the estimated linear velocity post-earthquake. Red is the best fitting viscoelastic model for the horizontal components, cyan is the best fitting visco model for the vertical component and magenta is the best fitting visco model for all components. Dashed vertical line indicates the date of the Puysegur earthquake (15 July 2009). The value in the bottom left of the upper panels is the distance of each site from the earthquake surface epicentre. Coseismic offsets have been removed.

4.4.3.2.1 Horizontal

The change in horizontal velocity for HOB2 and MOBS show statistically significant changes in the north component, and SYDN and MOBS showing statistically significant (but opposite) changes in the east velocity (Table 4.8). There appears to a visible offset at HOB2, TID1 and MOBS in the east component in 2009, but our method does not see it as significant due to high frequency noise. In Figure 4.4, MOBS show a noticeably high temporal variability over the period 2011-2014 in the north component, which remains unexplained. The difference may be due to sites in the south east of Australia still undergoing a small amount of postseismic deformation following the MI04 event, which is most significant in the north component (Tregoning et al., 2013; Watson et al., 2010).

4.4.3.2.2 Vertical

TABLE 4.8: Difference in GPS site velocities calculated before and after the Puysegur Trench 2009 earthquake. Uncertainty is one-sigma. Pre-earthquake trend calculated over the period 2006.0 – 2009.5, and post-earthquake trend calculated over the period 2009.5 – 2019.0. Bold values are statistically significant at one-sigma.

Site	Distance from PT09 (km)	ΔN trend (mm/yr)	ΔE trend (mm/yr)	ΔU trend (mm/yr)
HOB2	1553	**0.31 ± 0.19**	-0.13 ± 0.17	**-1.69 ± 0.40**
TID1	1861	-0.11 ± 0.23	0.08 ± 0.26	-0.57 ± 0.69
SYDN	1868	-0.06 ± 0.22	**0.38 ± 0.20**	**0.87 ± 0.65**
MOBS	1982	**-1.16 ± 0.34**	**-0.30 ± 0.24**	-0.28 ± 0.60

The velocity changes following the PT09 event in Figure 4.4 show no specific spatial pattern, with the largest change in the vertical component. The HOB2 site shows a velocity change larger than 1 mm/yr in the vertical component (Figure 4.4, Table 4.8) following the earthquake. The sites at TID1, MOBS and HOB2 demonstrate an increase in the rate of subsidence following the PT09 event (Figure 4.4), but Sydney (SYDN), with a lower latitude, shows positive change in trend.

4.5 Discussion

Our observational dataset (2000.0-2019.0) shows that not only has Australia deformed co-seismically and post-seismically in the horizontal component, it has (and continues to) deform in the vertical component since a series of events in 2004. Given the large earthquakes considered here occur close in time to the deployment of much of Australia's geodetic GNSS infrastructure, most Australian coordinate time series are affected by coseismic and postseismic deformation and therefore should not be considered as entirely consistent with longer-term inter-seismic velocities. The period 2000.0-2004.9 represents the longest period in our dataset with GPS data unaffected by significant earthquake activity (i.e., over this period there are no events > M_W 7.5 within subduction zones around the Australian plate boundary). While data exists before 2000 at about 12 sites, we note that the time series up to around the mid-2000s are complicated by frequent equipment changes (both antenna/receiver hardware and firmware) which increases the time series variability and the estimated velocity uncertainties. Nevertheless, we consider these velocities to be our most reliable estimate of the inter-seismic vertical velocity as we take into consideration the most up-to-date PPP processing strategy and models and simultaneously estimate seasonal signals, contributions from surface mass loading and identified offsets from equipment and firmware changes.

The inter-seismic velocities for the sites considered in this Chapter are given in Table 10 (2000.0-2004.9) and demonstrate a range in the vertical component from -3.95 ± 1.59 to 1.76 ± 0.61 mm/yr with an average magnitude and average sigma of -0.52

TABLE 4.9: Velocities of Australian GPS sites over the period 2000.0-2004.9, uncertainties are one-sigma. NB: MOBS and NNOR only have data from 2002.8 and 2002.5 respectively; PERT is likely undergoing increased subsidence due to local groundwater extraction (Featherstone et al., 2012). COCO and MAC1 are island sites and not included in the average values reported in the text.

Site	N (mm/yr)	E (mm/yr)	U (mm/yr)
CEDU	59.08 ± 0.21	28.98 ± 0.18	0.29 ± 0.64
COCO	50.15 ± 0.36	47.33 ± 0.30	2.20 ± 0.64
DARW	59.74 ± 0.48	36.15 ± 0.49	-3.95 ± 1.59
HOB2	55.93 ± 0.22	13.75 ± 0.14	-1.09 ± 0.52
KARR	58.28 ± 0.26	39.08 ± 0.18	1.76 ± 0.61
MAC1	33.03 ± 0.17	-10.91 ± 0.16	-3.04 ± 0.43
MOBS	57.41 ± 0.36	19.52 ± 0.27	-2.16 ± 0.46
NNOR	57.96 ± 0.24	38.51 ± 0.20	-1.12 ± 0.78
PERT	57.98 ± 0.34	39.10 ± 0.32	-5.08 ± 0.68
STR1	55.96 ± 0.35	18.51 ± 0.25	1.20 ± 0.44
TID1	55.23 ± 0.22	18.04 ± 0.13	1.07 ± 0.36
TIDB	55.35 ± 0.22	17.98 ± 0.14	0.64 ± 0.38
TOW2	55.35 ± 0.20	28.68 ± 0.20	0.66 ± 0.50
YAR2	57.36 ± 0.29	38.95 ± 0.21	1.55 ± 0.70

± 0.64 mm/yr (excluding island sites COCO and MAC1). The pre-2004 signals are mixed in sign, with sites at Darwin (DARW), Hobart (HOB2), Melbourne (MOBS) and New Norfolk (NNOR) indicating subsidence ranging from -3.95 ± 1.59 to -1.09 ± 0.52 mm/yr. The remaining mainland Australia sites at Ceduna (CEDU), Karratha (KARR), Mt Stromlo (STR1), Tidbinbilla (TID1, TIDB), Townsville (TOW2) demonstrate uplift ranging from 0.29 ± 0.64 to 1.76 ± 0.61 mm/yr. We note that MOBS and NNOR only have data from 2002.8 and 2002.5 respectively while PERT is likely undergoing subsidence due to local groundwater extraction (e.g. Featherstone et al., 2012; Featherstone et al., 2015). Note that these rates do not consider the effects of inter-decadal surface mass transport (largely driven by ice mass change) on vertical land motion, which would shift the estimates in Australia by -0.4 mm/yr in a centre of mass frame (Riva et al., 2017), or ∼0.2 mm/yr in a centre of figure frame. Nor does it consider the potential biases due to errors in reference frame origin (Riddell et al., 2017) or in the scale rate.

The series of large earthquakes in the Sumatra region over the period 2004 – 2012 caused significant changes in GPS vertical velocity estimates at Australian island territories and surface deformation at sites on the Australian mainland. Cocos (COCO) and Christmas Island (XMIS) are located on small islands in the Indian Ocean, whereas Karratha (KARR) and Broome (BRO1) are on the Australian mainland (Figure 4.1). Distant sites from the Sumatran events, such as Darwin, observe postseismic deformation in the horizontal and vertical components ongoing to at least 2010. Large subsidence (up to 4 mm/yr) is evident, particularly due to the

2004 Sumatran event, and observable deformation is seen to extend as far south as Karratha (KARR, 3500 km) and as far east as Darwin (DARW, 4200 km). While the changes in velocities, in all three components, are smaller following the SU12 earthquake, they are still evident in the time series at these very distant sites.

We find coseismic displacements of up to 3 mm at distances more than 5000 km from the earthquake event, highlighting that coseismic deformation can be far reaching across the Australian continent. For the Sumatran events (Table 6) we find the largest coseismic displacements in the vertical component after SU05 of -5.63 $\pm$ 2.63 mm at Yarragadee (YAR2), 3890 km from the event. The coseismic displacements for the MI04 event are shown in Table 3 and range, over distances of up to 3000 km, from insignificantly different from zero to 4.01 $\pm$ 0.99 mm in the northern component, up to 5.98 $\pm$ 1.33 mm in the eastern component and -3.49 $\pm$ 2.42 mm to 2.80 $\pm$ 1.86 mm in the vertical component. At the time of the PT09 event, we find coseismic displacements (Table 4.7) that reach 2.73 $\pm$ 0.79 mm in the northern component, 3.89 $\pm$ 5.00 mm in the eastern component (noting the large uncertainty) and -3.13 $\pm$ 2.53 mm to 3.26 $\pm$ 2.30 mm in the vertical component over distances of up to 2000 km. The coseismic estimates that are statistically significant (one-sigma) are highlighted in each of the tables using bold text, and we note an increased uncertainty on the vertical estimates.

Our preferred viscoelastic Earth model for MI04 is different to that identified by Tregoning et al. (2013). There are several reasons that are likely to contribute to this. First, our time series are computed differently to those used by Tregoning et al. (2013), although our modelling approach is broadly similar. In particular, the data period used to estimate the postseismic velocities is 8 years longer than used in Tregoning et al. (2013). Further, To determine if the additional length of the series affected the velocities pre- and post-earthquake, velocities were recomputed for the period 2004.9-2011.0 (Table C.3), matching the time period in Tregoning et al. (2013). The postseismic velocity estimates for the shorter period showed insignificant differences for the north and east components. The postseismic velocity uncertainties for HOB2, MOBS, STR1 and TID1 from the shorter series are about half that of those from the longer series.

Compared to Tregoning et al. (2013), we also use a different earth model as input into VISCO1D. We explicitly model the lower mantle in VISCO1D which made important differences to the model outputs. The template Earth model in VISCO1D is explicitly specified down to 670 km, with the lowest layer representing everything that sits below it. Adding explicit lower mantle layers both changes the predictions and improves agreement with an independent model (Grace Nield, pers. comm. February 2020). In our case, the fit of the viscoelastic models to the post-earthquake GPS velocity estimate was dramatically improved with the addition of an explicit lower mantle.

Of the earthquakes considered here, none of the postseismic deformation model predictions reproduce the observations in all three components. Earth models inferred from seismic tomography over Australia and its region provide evidence of substantial lateral variations at different depths (e.g. Debayle et al., 2005; Lekić and Romanowicz, 2011). These variations may be sufficiently large to mean that a 1D rheological model may not be appropriate for modelling post-seismic deformation of Australia and a 3D rheological model could be required to explain the observations. King and Santamaría-Gómez (2016) also suggested this to be the case for postseismic deformation of East Antarctica caused by far field earthquakes occurring in an oceanic setting.

In our analysis, we have assumed all deformation beyond ∼500 km from the earthquake event is in the far-field and can be attributed to viscoelastic postseismic deformation and not afterslip. The frictional response of the fault interface causes the near-field postseismic deformation to be dominated by afterslip (e.g. Marone, 1998). The implication for assuming no, or minimal, contribution from early afterslip behaviour is that the coseismic estimates can be biased by up to 10% (Twardzik et al., 2019). This has a small effect given the limitations of the 1D viscoelastic model.

Previously it has been suggested that while horizontal deformations are important for the accuracy of the reference frame in Australia, vertical deformations have a negligible effect (e.g. Tregoning et al., 2013). Our results suggest that this is not correct and failure to consider deformation in the vertical component will have implications for the realisation of the terrestrial reference frame. The current realisation of the frame (ITRF2014) does not consider the effects of the earthquakes we study on most Australian sites. Despite the demonstration of postseismic horizontal deformation of continental Australia by Tregoning et al. (2013) (e.g., HOB2, MOBS figure 1), Altamimi et al. (2016) only considered postseismic deformation at COCO and MAC1 (both island sites) during the construction of ITRF2014.

In this study we find substantial coseismic and postseismic deformations from several other earthquakes not considered in ITRF2014. For instance, we find significant coseismic offsets also occurred at several Australian sites as a result of the 2009 Puysegur Trench earthquake. This earthquake is not listed as having observable coseismic or postseismic deformation at Australian sites in publicly available offset files, such as those used in the realisation of ITRF2014, available at `ftp://ftp.iers.org/products/reference-systems/terrestrial/itrf/itrf2014/ITRF2014-soln-gnss.snx` (Altamimi et al., 2016), or for open access GPS time series, such as those in the Nevada Geodetic Laboratory "steps.txt" file, that is available at `http://geodesy.unr.edu/NGLStationPages/steps.txt`. Blewitt et al. (2018) use a threshold based on the distance of the GPS site from the earthquake to determine if there is possible expected seismic transient deformation at a site. The threshold ($r0$) is calculated as a simple function of the

earthquake magnitude:

$$r0 = 10^{(M_W * 0.5 - 0.8)} \tag{4.1}$$

In this instance the Australian GPS sites are beyond the distance threshold for the M_W 7.8 PT09 earthquake, and so would not be recognised in an automated procedure based purely on distance from the earthquake.

In some cases, present-day deformation at GNSS sites is still occurring in response to earthquake events that occurred prior to the commencement of the GNSS instrumental record. In these cases, modelling the event assists to understand the spatial variation in postseismic relaxation that cannot be detected from geodetic time series. We explored the effect of the 1979 M_W 7.8 Puysegur Trench earthquake on the present-day deformation of Australia. The 1979 event was in a similar location to the 2009 event, approximately 110 km separating the two surface epicentres. We considered the ongoing effects of that earthquake using a method similar to that detailed in Watson et al. (2010) where they investigated the deformation of Macquarie Island due to historic earthquakes. Using the range of Earth models adopted in the previous section relating to the Puysegur Trench earthquake in 2009, we can predict the surface deformation of the event in 1979 that may cause ongoing surface changes observed at Australian sites. Model outputs suggest that the south east of Australia (HOB2, SYDN, MOBS) may have been still experiencing subsidence of approximately 0.1–0.4 mm/yr during 2000.0-2010.0. There is no horizontal deformation (Figure C.2) indicated by our modelling over the period 1979-2010. While these deformations are small and maybe considered unreliable given the presence of unmodelled lateral variations in Earth properties, this finding highlights the need to consider postseismic signals from prior to the commencement of the GNSS record, with important impact on our determination of intra-seismic crustal velocities and potentially interpretation of long sea level records from tide gauges.

4.6 Conclusion

Using geodetic data, we have identified three dimensional coseismic and postseismic deformation of Australia occurring as a result of several large ($M_W > 7.5$) offshore plate boundary earthquakes since 2000. Our work extends the previous identification of horizontal deformation of Australia due to far-field offshore earthquakes by identifying substantial and sustained vertical deformation of Australia. We also study the effects of earthquakes not previously considered.

In the vertical component, we find coseismic offsets of up to 3 mm more than 5000 km from the earthquake event, and postseismic signals reaching several mm/yr sustained over several years. While viscoelastic models of postseismic deformation can explain the observed changes in velocity in one or two coordinate components, we were not able to reproduce them in all three coordinate components with a single

model. We suggest that this is due to limitations in using viscoelastic deformation models with a 1D (radially varying) Earth model, whereas the Earth rheological structure between the offshore earthquakes and continental Australia is complex.

As the demand for an accurate and stable geodetic reference frame increases toward stated international goals, we suggest that the earthquakes discussed here, and the deformation induced in all coordinate components, need to be considered. Given that ITRF2014 did not parameterise postseismic deformation at the sites studied on mainland Australia, there is scope for improvement in future realisations of the frame across this region.

There are limitations to this research based on the GPS time series length and the availability of high quality data, as well as limitations of the 1D viscoelastic modelling that does not consider lateral heterogeneities in rheology. These considerations offer scope for future research to improve observed and modelled postseismic deformation of the Australian continent, and advocates for improvements to available postseismic models. Improvements are required in reducing the number of offsets in time series due to, for example, equipment changes at GNSS sites. Although these are documented and can be applied as an offset in time series analysis, the introduction of offsets weakens the velocity and coseismic estimates at these sites, and potentially changes the noise characteristics (Williams, 2003a).

Although the effect of vertical land motion due to coseismic and postseismic deformation in Australia is small, it will influence estimates of absolute sea level from tide gauges along the Australian coast. Conversely, the use of satellite altimetry to derive estimates of relative sea level change also requires understanding of vertical land motion. This also has direct relevance to those in the altimetry community who seek to understand systematic error in altimeter records through comparison of altimetry and tide gauges corrected for land motion (e.g. Watson et al., 2015). This work underscores the inadequacy of assumptions of linear land motion, even in regions previously thought to be relatively immune from anthropogenic influences on crustal displacement.

4.7 Thesis Context

The research in this Chapter has used the improved coordinate time series from Chapter 3 to progress our understanding of the surface deformation occurring across Australia due to large earthquakes that occur on the plate boundary. Here, GPS observations of earthquake deformation from historic and present-day events are compared with forward predictive models or earthquake motion. Previously unidentified coseismic and postseismic deformation signals are identified in Australian GPS records. By the end of this Chapter this thesis has provided evidence and research that more robustly defines the uncertainty in the reference frame, recognised and

removed much of the local to regional common mode error, explored the secular velocity of Australia within the context of ITRF2014 and identified deformation caused by large plate-boundary earthquakes. These deformations are important for maintaining the integrity of the ITRF and understanding the cause of vertical land motion across the Australian plate. These newly identified deformations can be used to improve the vertical land motion estimates across Australia, as well as the determination and realisation of the ITRF. These improvements in understanding the deformation associated with earthquakes are particularly important at co-located geodetic observatories where the GNSS sites are fundamental to the reference frame realisation. Opportunities for future work exist using these series for understanding earth structure.

Chapter 5

Conclusions, Contributions and Future Research

5.1 General Conclusions

This thesis sets out to improve the determination and understanding of vertical land motion in Australia. It does this by first assessing the accuracy and stability of the International Terrestrial Reference Frame 2014 (ITRF2014) which underpins present-day geodetic positioning, and then investigates geophysical and systematic sources of temporal and spatial variability within Australian GPS time series. Present-day vertical surface deformation is shown to be measurable across Australia.

Accurately quantifying vertical land motion from GPS requires attention to the frame as well as to the analysis and interpretation of the derived coordinate time series. For this reason, the thesis first focused on understanding the influence of noise on the centre of mass definition of the ITRF. The thesis was then able to advance to identifying patterns of vertical land motion before finally addressing geophysical drivers of surface deformation across Australia in the final analysis chapter. Collectively this thesis explores the full set of uncertainties, signal and noise within GPS time series and velocities associated with the vertical motion of Australia. While further work remains, this thesis has substantially advanced our knowledge of both the vertical motion of Australia and uncertainty in geodetic measurements within Australia and indeed globally.

Prior to this thesis, significant progress was made in terms of understanding the broad geophysical processes driving vertical land motion, developing geodetic tools and techniques that were used to observe and monitor crustal deformation generally, but a gap remained in the detailed geodetic observation and interpretation of vertical land motion of the Australian continent. The identified knowledge gaps were addressed and answered by the three research questions (RQs):

1. What is the nature of the uncertainty in the current definition (ITRF2014) of the centre of the mass of the Earth and how does this effect GNSS height estimates in Australia?

2. To what level is vertical land motion across Australia spatially coherent, over what timescales, and what are the dominant driving mechanisms?

3. What is the magnitude, extent and duration of plausible far-field postseismic deformation in the vertical direction across the Indo-Australian Plate as a result of great earthquakes?

To address these questions, a series of objectives were defined:

1. Characterise the noise processes in the Satellite Laser Ranging (SLR) geocentre time series to better determine the uncertainty in the centre of mass of the Earth as used in the current realisation of the International Terrestrial Reference Frame (ITRF2014).

   (a) Investigate the occurrence of coloured noise in the geocentre time series as observed by SLR.

   (b) Compare geocentre motion as measured by SLR with geocentre motion from surface mass loading models.

2. Consistently process the entire Australian AuScope GNSS network of $\sim$120 sites with advanced precise point processing techniques, producing a database of time series that are robust.

3. Develop a spatiotemporal model of vertical land motion in Australia from GNSS stations for comparison with global and regional geophysical models (e.g. GIA ICE-6G model, hydrological surface mass loading from GRACE).

   (a) Spatiotemporal analysis (such as empirical orthogonal functions) will be used to decompose GPS time series to determine the dominant modes of deformation that are expressed in vertical land motion time series across Australia.

   (b) Simultaneously estimate temporally correlated noise models to determine an Australian vertical velocity field using multivariate regression.

4. Model coseismic and postseismic deformation of the Indo-Australian Plate after the occurrence of large earthquakes and compare with GPS observations.

   (a) Conduct modelling of large plate boundary earthquakes in the Australian region with elastic and viscoelastic earth models.

   (b) Compare observed crustal deformation from GPS with the modelled deformation.

   (c) Investigate if Australia experiences ongoing deformation due to historic earthquake events that occurred prior to the geodetic record.

The key results chapters of this thesis focus on reaching these objectives.

This chapter presents reflections on the work undertaken, identifies limitations, and proposes future research opportunities. The research findings of this thesis combine to present novel advances in geodetic analysis and contributes to the current understanding of present-day solid earth deformation of the Australian continent. Some of the identified limitations in this research are expanded upon in suggestions for future research in Section 5.3.

Chapter 2 describes work that contributes to answering RQ1 through addressing objective 1. In that Chapter, assumptions are challenged about the realisation of the ITRF, where currently a linear and white noise-only model is used. Reference frame errors not only propagate through station coordinates but will also affect downstream analysis products such as site velocities. In this thesis, it is revealed that geocentre motion time series relative to the ITRF2014, as determined using SLR data, contain errors that are temporally correlated. It is shown that if a non-temporally correlated model (white noise-only) is used the uncertainty on the motion of the origin translation rates (representing geocentre motion) can be underestimated by a factor of five. This equates to almost 0.5 mm/yr of uncertainty at the Earth's surface in central Australia (Alice Springs). This thesis demonstrates that a powerlaw and white noise model more realistically describes the temporally correlated noise of the origin translations with respect to ITRF2014 where the translation uncertainties (one-sigma) for X, Y, and Z are $\pm$0.13, $\pm$0.17 and $\pm$0.33 mm/yr. This finding is significant given that a goal of the international community is to have a reference frame that is stable and accurate to within 0.1 mm/yr (Gross et al., 2009). These targets are not currently met, and the use of a realistic stochastic model is required to understand if this goal is met. Ultimately, because of long-term surface mass redistribution, the ITRF will need to be realised considering non-linear parametric models or time-varying (e.g., Kalman Filter) models for geocentre motion. Some of the present limitations in geocentre motion determination could be overcome by the inclusion of other geodetic observations, such as GNSS.

Having understood further the uncertainty of the underlying reference frame, Chapters 3 and 4 then focus on the observation and interpretation of vertical land motion of Australia using GPS to answer RQ2. Previously published geodetic observations of vertical land motion for Australia have thus far suggested substantial subsidence across the continent and this is not in agreement with models of Glacial Isostatic Adjustment (GIA) or plate tectonic theory. Viewed alternatively, geodetic estimates of vertical motion of the Australian continent are yet to be fully explained by a combination of GIA, tectonic and surface mass transport models. The second objective of this thesis is to consistently process the entire Australian AuScope GNSS network of $\sim$120 sites to produce a robust database of time series. Under objective three, these time series were then used to build a spatiotemporal model of short-period noise as described in Chapter 3, with a focus on spatially coherent movement to improve the signal-to-noise ratio of GPS time series in Australia. This thesis investigated the

existence of a large-scale geophysical deformation such as due to global far-field earthquake sources or GIA, and surface loading. Reducing the uncertainty of GPS velocity estimation enabled the recognition of crustal deformation signals that are present in Australia spanning years to millennia, such as GIA and postseismic deformation.

In Chapter 3, surface deformation due to global surface mass transport was investigated using forward models and GRACE data and removed from the GPS time series. The El Niño–Southern Oscillation (ENSO) was explored in terms of its correlation with GPS time series. Empirical orthogonal functions were used to decompose the time series into common signals. It was suggested that the GPS velocities, obtained after spatiotemporal filtering and modelling of short-term geophysical effects, are better able to reflect the solid Earth's long-term motion. The refined vertical velocities can be used to improve estimates of sea level change at tide gauge sites around the Australian coastline and will have implications for such measurements globally. The geodetic velocity estimates could also be used to attempt to separate existing or future models of GIA in the Australian region, although the findings here were that GPS velocities even after filtering could not robustly separate different GIA models given their residual uncertainties.

The final objective of this thesis, to answer RQ3, was to determine if the filtered time series could be used to observe non-linear vertical postseismic deformation of the Indo-Australian Plate due to large plate boundary events. In Chapter 4 of this thesis, the filtered GPS time series are examined for evidence of coseismic and postseismic deformation induced by a selection of large ($M_W > 7.5$) offshore earthquakes over 2000.0-2019.0. This thesis finds that Australia is deforming vertically at measurable levels due to past earthquakes. Forward viscoelastic models can reproduce the approximate magnitude and evolution of these signals in one or two coordinate components but not all three components together, possibly due to lateral rheological variations not considered in the one-dimensional models. It is noted that a three-dimensional viscoelastic model may be required to explain the observed postseismic deformation. Modelled postseismic deformation from far-field earthquakes around Australia suggest ongoing deformation up to 5 mm over 20 years (2000.0-2019.0), but larger for the 2004 Sumatra-Anderman earthquake over a shorter period ($\sim$4 mm over 2004.9-2010.0). Both coseismic and postseismic deformations are identified and these have implications for the realisation of reference frames, noting that they were not considered in ITRF2014. Combined with the results of Chapter 3, these results suggest that after filtering, important signals of geodetic and geophysical interest become more evident.

The findings included in these chapters have a series of wider implications for the understanding of the vertical land motion of Australia.

Firstly, with state-of-the-art GPS analysis and filtering, the current vertical rate of

motion of Australia is not able to be determined confidently. The best estimates, from the period before 2004 when recent large earthquakes commenced, are scattered and ambiguous in sign (ranging from -3.95 $\pm$ 1.59 to 1.76 $\pm$ 0.61 mm/yr with an average value and average sigma of -0.52 $\pm$ 0.64 mm/yr). This has important implications for validating geophysical models (e.g., GIA) or correcting tide gauges. Compounding this is the uncertainty of the ITRF, which is determined to have origin uncertainty of $\pm$0.13, $\pm$0.17 and $\pm$0.33 (mm/yr, one sigma) in X, Y, and Z when a powerlaw and white noise model is adopted. Uncertainties in the reference frame scale will add to this.

Therefore, there remains a need for precise and accurate estimates of centennial or longer-term rates of the vertical land motion of Australia which are currently not available. A large fraction of the geodetic GPS stations in Australia have been deployed in a period coinciding with, or shortly after, a series of nearby 'Great Earthquakes' (>M_W 8.0) and the vertical, as well as horizontal, velocities derived using their data are biased from inter-seismic rates. In this dataset, the period 2000.0-2004.9 is the longest period where there is no significant earthquake activity in the Australian region. A small number of sites ($\sim$12) have available data over this period (and back to 1994 in some cases) and analysis of data from these sites represent the best chance of estimating reliable inter-seismic velocities. However, but there are a large number of equipment changes and upgrades in this period and these introduce offsets and variability and increase the uncertainty of the estimated velocities.

Secondly, the movement of the Earth's centre of mass with respect to the surface as a result of coseismic deformation influences the resulting site coordinates because pre- and post-earthquake vectors between the origin and the site are different. This also influences the set of coordinates used to define the ITRF due to the origin shift. Coordinates from sites not located near active seismic regions or in the near-field of earthquake events are also affected as a shift in reference frame origin changes the coordinate definition. This highlights the need for more accurate and complete offset and decay models for robust reference frame construction.

The range of coseismic and postseismic deformations presented in Chapter 4 suggests changes in internal stress which may have consequences for intra-plate earthquakes in Australia. Over geological time scales, within the last $\sim$25 million years, the Indo-Australian Plate has undergone significant deformation that has accumulated internally and can still be observed as motion today (Hayes et al., 2009). The concept that internal strain and external forcing from many years ago can cause present-day deformation has guided this research. Most large-scale stress patterns across Australia are generally attributed to broad plate tectonic interactions (Clark et al., 2014), but the stress pattern in eastern Australia are not easily explained by plate boundary forces and can more likely be attributed to present-day intraplate stress sources such as due to contrasts in elastic rock properties or stress rotations from

geological structures and density changes (Rajabi et al., 2017). The complex geological history of Australia plays an important part in the present-day observations of surface deformation, and the GPS time series produced by this research could help further understand the internal deformation of the Indo-Australian Plate.

To continuously measure how the Earth is changing in order to understand the geophysical processes, we need to continue to improve the measurements and subsequent data analysis. This requires us to understand the systematic bias and sources of error in our observations and modelling. This thesis has highlighted progress in understanding and removing sources of noise, but also the limitations in both observations and geophysical models; these motivate further research.

5.2 Contributions to the body of knowledge

- This thesis contains the first published results from a homogeneous and state-of-the-art processing of the complete the Australian AuScope GNSS array data as an entire network using a Precise Point Processing (PPP) approach. The processing approach uses repro2 orbits and clocks, high-resolution tropospheric modelling with the inclusion of higher order ionospheric terms and improved ocean loading displacement modelling (Chapter 3, Riddell et al. (2020)). The methodology used in this research contributes to the understanding of the signal and noise structure of the current best practice approach for rigorous analysis of GNSS data for the interpretation of natural and anthropogenic geophysical signals.
- This thesis contributes to the understanding of the uncertainty in the ITRF2014 origin (Chapter 2, Riddell et al. (2017)). The findings demonstrate that the current assumption of a white noise-only model significantly underestimates the uncertainty of reference frame origin motion with respect to ITRF2014. This result contributes to the refinement and attainment of a stable and accurate global geodetic reference frame presenting an improvement on current practices.
- This thesis contains the first observation of vertical deformation of the Australian continent caused by viscoelastic postseismic relaxation from far-field plate boundary earthquake events (Chapter 4). This work extends previous research that focused on the horizontal component of accumulated deformation, helping to understand the stress-state of the Australian crust, and can be used to improve the realisation of the ITRF in the Australasian region.
- A novel approach to estimate noise in geodetic time series has been used to realistically characterise uncertainties with the consideration of temporally correlated noise and multivariate regression (Chapter 3, Riddell et al. (2020)). This method can be applied to other geodetic data sets.

- This thesis highlights the value of old data (pre-2004) and how its careful analysis has tremendous geophysical importance in the future.
- Previously unidentified coseismic offsets and postseismic deformation are presented in this thesis (Chapter 4) that are not recorded in publicly available offset or decay models which can be used to improve the reference frame realisation in the Australasian region.

5.3 Recommendations and future research

Recommendations as a result of the research in this thesis are detailed below.

The use of a white noise-only model significantly underestimates the trend uncertainties of the SLR translations with respect to the ITRF2014 origin by a factor of five and could potentially bias applications which are reliant on the stability of the reference frame origin. The recommendation from this work is to highlight the importance of adopting an appropriate stochastic model for geocentre motion, particularly where the focus is on the vertical component. It is recommended that a noise model is used that considers the temporal correlation of the reference frame origin translation parameters in the determination of the next iteration of the ITRF (i.e. ITRF2020), and/or that non-linear parametric or Kalman Filter models (e.g. Abbondanza et al., 2017) are considered.

The spatiotemporal analysis performed in this thesis (Chapter 3, Riddell et al. (2020)) revealed that GPS time series can be used to determine the dominant modes of deformation that are expressed in vertical land motion time series across Australia. Temporally correlated noise, offsets, and transient deformation should be routinely and rigorously considered in future geophysical interpretation of Australian GPS time series. The results presented in this thesis provide evidence that deformation at GPS sites across the Australian continent is partially spatially coherent, but there is also evidence of individual site responses to earthquake events (Chapter 4) and other local site-dependent effects. The Indo-Australian tectonic plate should no longer be considered as a rigid reactive body, but one that undergoes complex deformation as a result of plate boundary forces, and intraplate stress and strain patterns.

During the analysis of individual time series that form the AuScope network the sensitivity of the series to offsets, non-linear signals, and spurious transients became apparent. There is a fine balance between updating firmware and hardware to make use of technological advances and introducing unnecessary sources of error. It is important to reiterate the need for the geodetic community to take care when making equipment changes and upgrades at GNSS stations. Where possible the approach should be to minimise changes and disruptions at fundamental sites.

This thesis fills a research gap in quantifying and further understanding vertical motion of the Indo-Australian Plate. The ability to address this gap has emerged

given the increased availability of computing infrastructure, data accessibility and improvements in data analysis. One major challenge in addressing the questions set out in this thesis is the signal to noise ratio in the context of the generally small geophysical signals of interest. The Australian continent is large, and initially the AuScope GNSS network was designed and installed with the intent of 200 km nominal spacing between stations (Johnston et al., 2008). This has been achieved in some areas, but there remain large portions of remote Australia where there is noticeably sparse coverage (e.g. Western Australia, Figure 1.2). With the announcement of Federal funding support for the National Positioning Infrastructure Capability in the Australian Federal Budget 2018-2019, the existing network will be extended with new GNSS ground stations as well as a new analytical data capabilities (Australia, 2018). High-quality geodetic stations are needed to infill areas that are sparsely observed by GNSS, as well as more focus on the combination of complementary space geodetic techniques such as gravity observations, Interferometric Synthetic Aperture Radar (InSAR) and satellite altimetry.

The new Australian investment in 'Positioning Australia' presents an exciting opportunity for further detailed analysis of surface motion, troposphere delays, and other associated GNSS analysis products and activities. Research opportunities are being explored across government and industry to enable Australians to have access to reliable positioning information. GNSS alone cannot isolate local deformations and this suggests the need for spatially continuous measurements, like those provided by InSAR, to complement the observations of solid-earth deformation. InSAR can be more sensitive to vertical motion than GNSS, and so a complementary study across Australia could demonstrate the occurrence of local or regional deformation caused by anthropogenic effects.

The research in this thesis paves the way for future studies to extend understanding on:

- the application of high-quality GNSS vertical velocities estimates to tide gauge observations of regional sea level change, including research into the spatial relationships between GNSS site and tide gauge locations (i.e. can kriging or regional network solutions be used to transfer GNSS estimates of vertical land motion to tide gauges if they are not in close proximity?). This links to the remit of the new International Association of Geodesy Inter-Commission Committee on "Geodesy for Climate Research" (ICCC) joint working group on sea level and vertical land motion;
- the need for spatially continuous InSAR measurements of vertical land motion to compliment the GNSS observations at tide gauges to improve the understanding of local anthropogenic effects on surface deformation in Australia;
- the consideration of draconitic and chandler periodic aliasing to further improve the signal to noise ratio in Australian GNSS series;

- the adoption of a laterally varying Earth model for far-field postseismic relaxation studies to assess if this could improve surface deformation estimates;
- the use of precise Australian GNSS velocity estimates to constrain future determinations of GIA models, which are used as a correction for satellite altimetry observations or to correct sea level estimates from tide gauges for vertical land motion; and
- an assessment of the benefit of including other GNSS signals (e.g. Galileo, GLONASS, Beidou) for site position and velocity estimates in Australia.

This research could additionally be used to inform future analyses including:

- future analyses of the AuScope GNSS array as the data matures and with the addition of new infrastructure, taking into consideration site-specific effects (equipment changes, monument types, individual antenna calibrations, local surface deformation, thermal expansion);
- investigation of the ongoing effects of firmware and hardware upgrades of a national GNSS network, such as the 'Positioning Australia' National Positioning Infrastructure Capability project that has commenced (2018-2022); and
- inclusion of other geodetic observations in geocentre motion determinations, such as GNSS. The current determination of geocentre motion as realised in ITRF is limited to observations from Satellite Laser Ranging.

5.4 Final remarks

This thesis advances our understanding of the geophysical processes that drive surface deformation, and the space geodetic techniques that are used to quantify them. With a focus on the Australian continent this work has investigated the response of the Earth's surface to a range of geophysical processes that occur over various temporal and spatial scales. The surface deformations modelled and observed in this thesis push the limit of the signal-to-noise ratio present in current space geodetic analyses and the available geophysical models. New insights into the spatial patterns of the surface deformation field informs our understanding of relevant processes and highlights an ever-increasing demand for accurate crustal position and velocity estimates. Having a greater understanding of the motion of the Indo-Australian Plate with rigorously determined uncertainties will allow a more accurate and reliable geophysical interpretation, and the development of a reference frame to support international efforts towards disaster mitigation, sustainable development and data interoperability.

References

Abbondanza, C., T. M. Chin, R. S. Gross, M. B. Heflin, J. W. Parker, B. S. Soja, T. van Dam, and X. Wu (2017). "JTRF2014, the JPL Kalman filter and smoother realization of the International Terrestrial Reference System". *Journal of Geophysical Research: Solid Earth*, 122(10), pp. 8474–8510. DOI: 10.1002/2017jb014360.

Agnew, D. (1997). "NLOADF: A program for computing ocean-tide loading". *Journal of Geophysical Research: Solid Earth*, 102(B3), pp. 5109–5110. DOI: 10.1029/96JB03458.

Akaike, H. (1973). "Information theory and an extension of the maximum likelihood principle". In: *Second International Symposium on Information Theory*. Ed. by B. Petrov and F. Csaki. Akademiai Kiado, pp. 267–281.

Altamimi, Z., X. Collilieux, J. Legrand, B. Garayt, and C. Boucher (2007). "ITRF2005: A new release of the International Terrestrial Reference Frame based on time series of station positions and Earth Orientation Parameters". *Journal of Geophysical Research: Solid Earth*, 112(B9). DOI: 10.1029/2007JB004949.

Altamimi, Z., X. Collilieux, and L. Métivier (2011). "ITRF2008: An improved solution of the international terrestrial reference frame". *Journal of Geodesy*, 85(8), pp. 457–473. DOI: 10.1007/s00190-011-0444-4.

Altamimi, Z., L. Métivier, and X. Collilieux (2012). "ITRF2008 plate motion model". *Journal of Geophysical Research: Solid Earth*, 117(B7), B07402. DOI: 10.1029/2011jb008930.

Altamimi, Z., P. Rebischung, L. Métivier, and X. Collilieux (2016). "ITRF2014: A new release of the International Terrestrial Reference Frame modeling non-linear station motions". *Journal of Geophysical Research: Solid Earth*, 121(8), pp. 6109–6131. DOI: 10.1002/2016JB013098.

Amiri-Simkooei, A. (2007). "Least-squares variance component estimation: theory and GPS applications". Thesis.

Amiri-Simkooei, A. (2009). "Noise in multivariate GPS position time-series". *Journal of Geodesy*, 83(2), pp. 175–187. DOI: 10.1007/s00190-008-0251-8.

Amiri-Simkooei, A. (2013). "On the nature of GPS draconitic year periodic pattern in multivariate position time series". *Journal of Geophysical Research: Solid Earth*, 118(5), pp. 2500–2511. DOI: 10.1002/jgrb.50199.

Amiri-Simkooei, A., T. Mohammadloo, and D. Argus (2017). "Multivariate analysis of GPS position time series of JPL second reprocessing campaign". *Journal of Geodesy*, 91(6), pp. 685–704. DOI: 10.1007/s00190-016-0991-9.

Anderson, H., T. Webb, and J. Jackson (1993). "Focal mechanisms of large earthquakes in the South Island of New Zealand: implications for the accommodation of Pacific-Australia plate motion". *Geophysical Journal International*, 115(3), pp. 1032–1054. DOI: 10.1111/j.1365-246X.1993.tb01508.x.

Appleby, G., J. Rodríguez, and Z. Altamimi (2016). "Assessment of the accuracy of global geodetic satellite laser ranging observations and estimated impact on ITRF scale: estimation of systematic errors in LAGEOS observations 1993–2014". *Journal of Geodesy*, pp. 1–18. DOI: 10.1007/s00190-016-0929-2.

Argus, D. (2007). "Defining the translational velocity of the reference frame of Earth". *Geophysical Journal International*, 169(3), pp. 830–838. DOI: 10.1111/j.1365-246X.2007.03344.x.

Argus, D. (2012). "Uncertainty in the velocity between the mass center and surface of Earth". *Journal of Geophysical Research: Solid Earth*, 117(B10), pp. 1–15. DOI: 10.1029/2012JB009196.

Argus, D., R. Gordon, M. Heflin, C. Ma, R. Eanes, P. Willis, W. Peltier, and S. Owen (2010). "The angular velocities of the plates and the velocity of Earth's centre from space geodesy". *Geophysical Journal International*, 180(3), pp. 913–960. DOI: 10.1111/j.1365-246X.2009.04463.x.

Argus, D. and M. Heflin (1995). "Plate motion and crustal deformation estimated with geodetic data from the Global Positioning System". *Geophysical Research Letters*, 22(15), pp. 1973–1976. DOI: 10.1029/95GL02006.

Argus, D., W. Peltier, R. Drummond, and A. Moore (2014). "The Antarctica component of postglacial rebound model ICE-6G_C (VM5a) based on GPS positioning, exposure age dating of ice thicknesses, and relative sea level histories". *Geophysical Journal International*, 198(1), pp. 537–563. DOI: 10.1093/gji/ggu140.

Australia, G. (2018). *National Positioning Infrastructure*. Web Page. accessed 27 July 2018.

Banerjee, P., F. Pollitz, B. Nagarajan, and R. Burgmann (2007). "Coseismic Slip Distributions of the 26 December 2004 Sumatra–Andaman and 28 March 2005 Nias Earthquakes from gps Static Offsets". *Bulletin of the Seismological Society of America*, 97(1A), S86–S102. DOI: 10.1785/0120050609.

Barnie, T. and C. Oppenheimer (2015). "Extracting High Temperature Event radiance from satellite images and correcting for saturation using Independent Component Analysis". *Remote Sensing of Environment*, 158, pp. 56–68. DOI: https://doi.org/10.1016/j.rse.2014.10.023.

Beavan, J. (2005). "Noise properties of continuous GPS data from concrete pillar geodetic monuments in New Zealand and comparison with data from U.S. deep drilled braced monuments". *Journal of Geophysical Research: Solid Earth*, 110(B8), pp. 1–13. DOI: 10.1029/2005jb003642.

Beavan, J., P. Denys, M. Denham, B. Hager, T. Herring, and P. Molnar (2010a). "Distribution of present-day vertical deformation across the Southern Alps, New

Zealand, from 10 years of GPS data". *Geophysical Research Letters*, 37(16). DOI: 10.1029/2010gl044165.

Beavan, J., S. Samsonov, P. Denys, R. Sutherland, N. Palmer, and M. Denham (2010b). "Oblique slip on the Puysegur subduction interface in the 2009 July MW 7.8 Dusky Sound earthquake from GPS and InSAR observations: implications for the tectonics of southwestern New Zealand". *Geophysical Journal International*, 183(3), pp. 1265–1286. DOI: 10.1111/j.1365-246X.2010.04798.x.

Bedford, J. and M. Bevis (2018). "Greedy Automatic Signal Decomposition and its application to daily GPS time series". *Journal of Geophysical Research: Solid Earth*, 123(8), pp. 6992–7003. DOI: 10.1029/2017JB014765.

Bedford, J., M. Moreno, S. Li, O. Oncken, J. Baez, M. Bevis, O. Heidbach, and D. Lange (2016). "Separating rapid relocking, afterslip, and viscoelastic relaxation: An application of the postseismic straightening method to the Maule 2010 cGPS". *Journal of Geophysical Research: Solid Earth*, 121(10), pp. 7618–7638. DOI: 10.1002/2016JB013093.

Bertiger, W., S. Desai, B. Haines, N. Harvey, A. Moore, S. Owen, and J. Weiss (2010). "Single receiver phase ambiguity resolution with GPS data". *Journal of Geodesy*, 84(5), pp. 327–337. DOI: 10.1007/s00190-010-0371-9.

Bevis, M., F. Taylor, B. Schutz, J. Recy, B. Isacks, S. Helu, R. Singh, E. Kendrick, J. Stowell, B. Taylor, and S. Calmantli (1995). "Geodetic observations of very rapid convergence and back-arc extension at the Tonga arc". *Nature*, 374, p. 249. DOI: 10.1038/374249a0.

Bilitza, D., D. Altadill, V. Truhlik, V. Shubin, I. Galkin, B. Reinisch, and X. Huang (2017). "International Reference Ionosphere 2016: From ionospheric climate to real-time weather predictions". *Space Weather*, 15(2), pp. 418–429. DOI: 10.1002/2016SW001593.

Bird, P. (2003). "An updated digital model of plate boundaries". *Geochemistry, Geophysics, Geosystems*, 4(3). DOI: 10.1029/2001GC000252.

Blewitt, G. (2003). "Self-consistency in reference frames, geocenter definition, and surface loading of the solid Earth". *Journal of Geophysical Research: Solid Earth*, 108(B2). DOI: 10.1029/2002JB002082.

Blewitt, G. (2015). "Terrestrial Reference Frame Requirements for Studies of Geodynamics and Climate Change". In: *REFAG 2014. International Association of Geodesy Symposia, vol 146*. Ed. by T. van Dam. Vol. International Association of Geodesy Symposia, vol 146. Springer International Publishing, pp. 209–216.

Blewitt, G., W. Hammond, and C. Kreemer (2018). "Harnessing the GPS explosion for interdisciplinary science". *Eos, Transactions American Geophysical Union*, 99. DOI: https://doi.org/10.1029/2018EO104623.

Blewitt, G. and D. Lavallée (2002). "Effect of annual signals on geodetic velocity". *Journal of Geophysical Research: Solid Earth*, 107(B7), ETG 9–1–ETG 9–11. DOI: 10.1029/2001jb000570.

Bock, Y. and D. Melgar (2016). "Physical applications of GPS geodesy: a review". *Reports on Progress in Physics*, 79(10), p. 106801.

Boehm, J., A. Niell, H. Schuh, V. Tesmer, and P. Tregoning (2006). "Mapping functions for atmospheric delay modelling in GNSS analysis". In: *Proceedings of the IGS Analysis Workshop, Darmstad*.

Bogusz, J. and A. Klos (2015). "On the significance of periodic signals in noise analysis of GPS station coordinates time series". *GPS Solutions*, pp. 1–10. DOI: 10.1007/s10291-015-0478-9.

Bos, M., L. Bastos, and R. Fernandes (2010). "The influence of seasonal signals on the estimation of the tectonic motion in short continuous GPS time-series". *Journal of Geodynamics*, 49(3–4), pp. 205–209. DOI: http://dx.doi.org/10.1016/j.jog.2009.10.005.

Bos, M., R. Fernandes, S. Williams, and L. Bastos (2007). "Fast error analysis of continuous GPS observations". *Journal of Geodesy*, 82(3), pp. 157–166. DOI: 10.1007/s00190-007-0165-x.

Bos, M., R. Fernandes, S. Williams, and L. Bastos (2013). "Fast error analysis of continuous GNSS observations with missing data". *Journal of Geodesy*, 87(4), pp. 351–360. DOI: 10.1007/s00190-012-0605-0.

Bouillé, F., A. Cazenave, J. Lemoine, and J. Crétaux (2000). "Geocentre motion from the DORIS space system and laser data to the Lageos satellites: comparison with surface loading data". *Geophysical Journal International*, 143(1), pp. 71–82. DOI: 10.1046/j.1365-246x.2000.00196.x.

Bouin, M. and G. Wöppelmann (2010). "Land motion estimates from GPS at tide gauges: a geophysical evaluation". *Geophysical Journal International*, 180(1), pp. 193–209. DOI: 10.1111/j.1365-246X.2009.04411.x.

Bowman, J., G. Gibson, and T. Jones (1990). "Aftershocks of the 1988 January 22 Tennant Creek, Australia Intraplate Earthquakes: Evidence for a Complex Thrust-Fault Geometry". *Geophysical Journal International*, 100(1), pp. 87–97. DOI: 10.1111/j.1365-246X.1990.tb04570.x.

Burbidge, D. (2004). "Thin plate neotectonic models of the Australian plate". *Journal of Geophysical Research: Solid Earth*, 109(B10). DOI: 10.1029/2004jb003156.

Burgette, R., C. Watson, J. Church, J. White N., P. Tregoning, and R. Coleman (2013). "Characterising and minimising the effects of noise in tide gauge time series: relative and geocentric sea level rise around Australia". *Geophys. J. Int.* 194(2), pp. 719–736. DOI: 10.1093/gji/ggt131.

Cardellach, E., P. Elósegui, and J. Davis (2007). "Global distortion of GPS networks associated with satellite antenna model errors". *Journal of Geophysical Research: Solid Earth*, 112(B7), B07405. DOI: 10.1029/2006jb004675.

Caron, L., E. Ivins, E. Larour, S. Adhikari, J. Nilsson, and G. Blewitt (2018). "GIA Model Statistics for GRACE Hydrology, Cryosphere, and Ocean Science". *Geophysical Research Letters*, 45(5), pp. 2203–2212. DOI: 10.1002/2017GL076644.

Chao, B., Y. Wu, and Y. Li (2008). "Impact of Artificial Reservoir Water Impoundment on Global Sea Level". *Science*, 320(5873), pp. 212–214. DOI: 10.1126/science.1154580.

Cheng, M. and J. Ries (2017). "The unexpected signal in GRACE estimates of C20". *Journal of Geodesy*, 91(8), pp. 897–914. DOI: 10.1007/s00190-016-0995-5.

Church, J., P. Clark, A. Cazenave, J. Gregory, S. Jevrejeva, A. Levermann, M. Merrifield, G. Milne, R. Nerem, P. Nunn, A. Payne, W. Pfeffer, D. Stammer, and A. Unnikrishnan (2013). *Sea level change*. Report. IPCC.

Clark, D., A. McPherson, and T. Allen (2014). "Intraplate earthquakes in Australia". In: *Intraplate Earthquakes*. Ed. by P. Talwani. Cambridge: Cambridge University Press, pp. 8–49. DOI: 10.1017/CBO9781139628921.003.

Clark, G. and E. Johnston (2017). *Australia state of the environment 2016: coasts*. Report. Australian Government Department of the Environment and Energy.

Collilieux, X. and Z. Altamimi (2013). "External Evaluation of the Origin and Scale of the International Terrestrial Reference Frame". In: *Reference Frames for Applications in Geosciences*. Ed. by Z. Altamimi and X. Collilieux. Berlin, Heidelberg: Springer Berlin Heidelberg, pp. 27–31. DOI: 10.1007/978-3-642-32998-2_5.

Collilieux, X., Z. Altamimi, J. Ray, T. van Dam, and X. Wu (2009). "Effect of the satellite laser ranging network distribution on geocenter motion estimation". *Journal of Geophysical Research: Solid Earth*, 114(B4). DOI: 10.1029/2008JB005727.

Collilieux, X., T. van Dam, J. Ray, D. Coulot, L. Métivier, and Z. Altamimi (2012). "Strategies to mitigate aliasing of loading signals while estimating GPS frame parameters". *Journal of Geodesy*, 86(1), pp. 1–14. DOI: 10.1007/s00190-011-0487-6.

Collilieux, X. and G. Wöppelmann (2011). "Global sea-level rise and its relation to the terrestrial reference frame". *Journal of Geodesy*, 85(1), pp. 9–22. DOI: 10.1007/s00190-010-0412-4.

Comon, P. (1994). "Independent component analysis, A new concept?" *Signal Processing*, 36(3), pp. 287–314. DOI: https://doi.org/10.1016/0165-1684(94)90029-9.

Conker, R., M. El-Arini, C. Hegarty, and T. Hsiao (2003). "Modeling the effects of ionospheric scintillation on GPS/Satellite-Based Augmentation System availability". *Radio Science*, 38(1), pp. 1–1–1–23. DOI: 10.1029/2000rs002604.

Correa-Mora, F., C. DeMets, D. Alvarado, H. Turner, G. Mattioli, D. Hernandez, C. Pullinger, M. Rodriguez, and C. Tenorio (2009). "GPS-derived coupling estimates for the Central America subduction zone and volcanic arc faults: El Salvador, Honduras and Nicaragua". *Geophysical Journal International*, 179(3), pp. 1279–1291. DOI: 10.1111/j.1365-246X.2009.04371.x.

Crone, A., M. Machette, and J. Bowman (1992). *Geologica investigations of the 1988 Tennant Creek, Australia, earthquakes; implications for paleoseismicity in stable continental regions*. Report 2032A. United States Geological Survey Bulletin 2032-A.

Crone, A., M. Machette, and J. Bowman (1997). "Episodic nature of earthquake activity in stable continental regions revealed by palaeoseismicity studies of Australian

and North American quaternary faults". *Australian Journal of Earth Sciences*, 44(2), pp. 203–214. DOI: 10.1080/08120099708728304.

Dach, R., J. Böhm, S. Lutz, P. Steigenberger, and G. Beutler (2011). "Evaluation of the impact of atmospheric pressure loading modeling on GNSS data analysis". *Journal of Geodesy*, 85(2), pp. 75–91. DOI: 10.1007/s00190-010-0417-z.

Dangendorf, S., M. Marcos, G. Wöppelmann, C. Conrad, T. Frederikse, and R. Riva (2017). "Reassessment of 20th century global mean sea level rise". *Proceedings of the National Academy of Sciences*, 114(23), pp. 5946–5951. DOI: 10.1073/pnas.1616007114.

Davis, J., P. Elósegui, J. Mitrovica, and M. Tamisiea (2004). "Climate-driven deformation of the solid Earth from GRACE and GPS". *Geophysical Research Letters*, 31(24). DOI: 10.1029/2004GL021435.

Davis, J., B. Wernicke, and M. Tamisiea (2012). "On seasonal signals in geodetic time series". *Journal of Geophysical Research: Solid Earth*, 117(B01403). DOI: 10.1029/2011JB008690.

Debayle, E., B. Kennett, and K. Priestley (2005). "Global azimuthal seismic anisotropy and the unique plate-motion deformation of Australia". *Nature*, 433(7025), pp. 509–512. DOI: 10.1038/nature03247.

Denham, D., L. Alexander, I. Everingham, P. Gregson, R. McCaffrey, and J. Enever (1987). "The 1979 Cadoux earthquake and intraplate stress in Western Australia". *Australian Journal of Earth Sciences*, 34(4), pp. 507–521. DOI: 10.1080/08120098708729429.

Dentith, M. C. and W. E. Featherstone (2003). "Controls on intra-plate seismicity in southwestern Australia". *Tectonophysics*, 376(3), pp. 167–184. DOI: https://doi.org/10.1016/j.tecto.2003.10.002.

Desai, S. and R. Ray (2014). "Consideration of tidal variations in the geocenter on satellite altimeter observations of ocean tides". *Geophysical Research Letters*, 41(7), pp. 2454–2459. DOI: 10.1002/2014gl059614.

Dobslaw, H. and M. Thomas (2007). "Simulation and observation of global ocean mass anomalies". *Journal of Geophysical Research: Oceans*, 112(C5). DOI: 10.1029/2006JC004035.

Dong, D., J. Dickey, Y. Chao, and M. Cheng (1997). "Geocenter variations caused by atmosphere, ocean and surface ground water". *Geophysical Research Letters*, 24(15), pp. 1867–1870. DOI: 10.1029/97GL01849.

Dong, D., P. Fang, Y. Bock, F. Webb, L. Prawirodirdjo, S. Kedar, and P. Jamason (2006). "Spatiotemporal filtering using principal component analysis and Karhunen-Loeve expansion approaches for regional GPS network analysis". *Journal of Geophysical Research: Solid Earth*, 111(B3). DOI: 10.1029/2005JB003806.

Dong, D., W. Qu, P. Fang, and D. Peng (2014). "Non-linearity of geocentre motion and its impact on the origin of the terrestrial reference frame". *Geophysical Journal International*, 198(2), pp. 1071–1080. DOI: 10.1093/gji/ggu187.

Dong, D., T. Yunck, and M. Heflin (2003). "Origin of the International Terrestrial Reference Frame". *Journal of Geophysical Research: Solid Earth*, 108(B4). DOI: 10.1029/2002JB002035.

Duputel, Z., H. Kanamori, V. Tsai, L. Rivera, L. Meng, J.-P. Ampuero, and J. Stock (2012). "The 2012 Sumatra great earthquake sequence". *Earth and Planetary Science Letters*, 351, pp. 247–257. DOI: http://dx.doi.org/10.1016/j.epsl.2012.07.017.

Dziewonski, A. and D. Anderson (1981). "Preliminary reference Earth model". *Physics of the Earth and Planetary Interiors*, 25(4), pp. 297–356. DOI: http://dx.doi.org/10.1016/0031-9201(81)90046-7.

Egbert, G., S. Erofeeva, S.-C. Han, S. Luthcke, and R. Ray (2009). "Assimilation of GRACE tide solutions into a numerical hydrodynamic inverse model". *Geophysical Research Letters*, 36(20). DOI: 10.1029/2009GL040376.

Farrell, W. (1972). "Deformation of the Earth by surface loads". *Reviews of Geophysics*, 10(3), pp. 761–797. DOI: 10.1029/RG010i003p00761.

Featherstone, W., M. Filmer, N. Penna, L. Morgan, and A. Schenk (2012). "Anthropogenic land subsidence in the Perth Basin: challenges for its retrospective geodetic detection". *Journal of the Royal Society of Western Australia*, 95, pp. 53–62.

Featherstone, W., N. Penna, M. Filmer, and S. Williams (2015). "Nonlinear subsidence at Fremantle, a long-recording tide gauge in the Southern Hemisphere". *Journal of Geophysical Research: Oceans*, 120(10), pp. 7004–7014. DOI: 10.1002/2015jc011295.

Flechtner, F., H. Dobslaw, and E. Fagiolini (2015). *AOD1B product description document for product release 05 (Rev. 4.3)*. Report. GFZ German Research Center for Geosciences.

Forootan, E., J. Awange, J. Kusche, B. Heck, and A. Eicker (2012). "Independent patterns of water mass anomalies over Australia from satellite data and models". *Remote Sensing of Environment*, 124, pp. 427–443. DOI: https://doi.org/10.1016/j.rse.2012.05.023.

Frederikse, T., S. Jevrejeva, R. Riva, and S. Dangendorf (2018). "A Consistent Sea-Level Reconstruction and Its Budget on Basin and Global Scales over 1958–2014". *Journal of Climate*, 31(3), pp. 1267–1280. DOI: 10.1175/jcli-d-17-0502.1.

Frederikse, T., R. Riva, M. Kleinherenbrink, Y. Wada, M. van den Broeke, and B. Marzeion (2016). "Closing the sea level budget on a regional scale: trends and variability on the Northwestern European continental shelf". *Geophysical Research Letters*, DOI: 10.1002/2016GL070750.

Freed, A. M., R. Bürgmann, and T. Herring (2007). "Far-reaching transient motions after Mojave earthquakes require broad mantle flow beneath a strong crust". *Geophysical Research Letters*, 34(19). DOI: https://doi.org/10.1029/2007GL030959.

Fritsche, M., P. Döll, and R. Dietrich (2012). "Global-scale validation of model-based load deformation of the Earth's crust from continental watermass and atmospheric pressure variations using GPS". *Journal of Geodynamics*, 59–60, pp. 133–142. DOI: http://dx.doi.org/10.1016/j.jog.2011.04.001.

Fu, Y., J. Freymueller, and T. van Dam (2012). "The effect of using inconsistent ocean tidal loading models on GPS coordinate solutions". *Journal of Geodesy*, 86(6), pp. 409–421. DOI: 10.1007/s00190-011-0528-1.

García-García, D., C. Ummenhofer, and V. Zlotnicki (2011). "Australian water mass variations from GRACE data linked to Indo-Pacific climate variability". *Remote Sensing of Environment*, 115(9), pp. 2175–2183. DOI: https://doi.org/10.1016/j.rse.2011.04.007.

Gazeaux, J., S. Williams, M. King, M. Bos, R. Dach, M. Deo, A. Moore, L. Ostini, E. Petrie, M. Roggero, F. Teferle, G. Olivares, and F. Webb (2013). "Detecting offsets in GPS time series: First results from the detection of offsets in GPS experiment". *Journal of Geophysical Research: Solid Earth*, 118(5), pp. 2397–2407. DOI: 10.1002/jgrb.50152.

Ge, M., G. Gendt, G. Dick, F. Zhang, and C. Reigber (2005). "Impact of GPS satellite antenna offsets on scale changes in global network solutions". *Geophysical Research Letters*, 32(6). DOI: 10.1029/2004gl022224.

Gehrels, R. (2016). "Chapter 16 - Rising Sea Levels". In: *Climate Change (Second Edition)*. Ed. by T. Letcher. Boston: Elsevier, pp. 241–252. DOI: https://doi.org/10.1016/B978-0-444-63524-2.00016-6.

Gelaro, R., W. McCarty, M. Suárez, R. Todling, A. Molod, L. Takacs, C. Randles, A. Darmenov, M. Bosilovich, R. Reichle, K. Wargan, L. Coy, R. Cullather, C. Draper, S. Akella, V. Buchard, A. Conaty, A. Silva, W. Gu, G.-K. Kim, R. Koster, R. Lucchesi, D. Merkova, J. Nielsen, G. Partyka, S. Pawson, W. Putman, M. Rienecker, S. Schubert, M. Sienkiewicz, and B. Zhao (2017). "The Modern-Era Retrospective Analysis for Research and Applications, Version 2 (MERRA-2)". *Journal of Climate*, 30(14), pp. 5419–5454. DOI: 10.1175/jcli-d-16-0758.1.

Gordeev, R., B. Kagan, and E. Polyakov (1977). "The Effects of Loading and Self-Attraction on Global Ocean Tides: The Model and the Results of a Numerical Experiment". *Journal of Physical Oceanography*, 7(2), pp. 161–170. DOI: doi:10.1175/1520-0485(1977)007<0161:TEOLAS>2.0.CO;2.

Gordon, F. and J. Lewis (1980). *The Meckering and Calingiri earthquakes October 1968 and March 1970*. Report.

Gross, R., G. Beutler, and H.-P. Plag (2009). "Integrated scientific and societal user requirements and functional specifications for the GGOS". In: *Global Geodetic Observing System: Meeting the Requirements of a Global Society on a Changing Planet in 2020*. Ed. by H.-P. Plag and M. Pearlman. Berlin, Heidelberg: Springer Berlin Heidelberg, pp. 209–224. DOI: 10.1007/978-3-642-02687-4_7.

Gruszczynski, M., A. Klos, and J. Bogusz (2016). "Orthogonal transformation in extracting of common mode error from continuous GPS network". *Acta Geodynamica et Geomaterialia*, 13(3(183)), pp. 291–298. DOI: 10.13168/AGG.2016.0011.

Han, G., Z. Ma, N. Chen, J. Yang, and N. Chen (2015). "Coastal sea level projections with improved accounting for vertical land motion". *Nature Scientific Reports*, 5, p. 16085. DOI: 10.1038/srep16085.

Hayes, G., K. Furlong, and C. Ammon (2009). "Intraplate deformation adjacent to the Macquarie Ridge south of New Zealand—The tectonic evolution of a complex plate boundary". *Tectonophysics*, 463(1), pp. 1–14. DOI: http://dx.doi.org/10.1016/j.tecto.2008.09.024.

Hayes, G., E. Meyers, J. Dewey, R. Briggs, P. Earle, H. Benz, G. Smoczyk, H. Flamme, W. Barnhart, R. Gold, and K. Furlong (2017). *Tectonic summaries of magnitude 7 and greater earthquakes from 2000 to 2015*. Report 2016-1192. DOI: 10.3133/ofr20161192.

He, X., M. Bos, J. Montillet, and R. Fernandes (2019). "Investigation of the noise properties at low frequencies in long GNSS time series". *Journal of Geodesy*, DOI: 10.1007/s00190-019-01244-y.

He, X., X. Hua, K. Yu, W. Xuan, T. Lu, W. Zhang, and X. Chen (2015). "Accuracy enhancement of GPS time series using principal component analysis and block spatial filtering". *Advances in Space Research*, 55(5), pp. 1316–1327. DOI: http://doi.org/10.1016/j.asr.2014.12.016.

Hearn, E. (2003). "What can GPS data tell us about the dynamics of post-seismic deformation?" *Geophysical Journal International*, 155(3), pp. 753–777. DOI: 10.1111/j.1365-246X.2003.02030.x.

Hearn, E., F. Pollitz, W. Thatcher, and C. Onishi (2013). "How do "ghost transients" from past earthquakes affect GPS slip rate estimates on southern California faults?" *Geochemistry, Geophysics, Geosystems*, 14(4), pp. 828–838. DOI: 10.1002/ggge.20080.

Heine, C., R. Müüller, B. Steinberger, and L. DiCaprio (2010). "Integrating deep Earth dynamics in paleogeographic reconstructions of Australia". *Tectonophysics*, 483(1), pp. 135–150. DOI: https://doi.org/10.1016/j.tecto.2009.08.028.

Hejrani, B. and H. Tkalčić (2019). "The 20 May 2016 Petermann Ranges earthquake: centroid location, magnitude and focal mechanism from full waveform modelling". *Australian Journal of Earth Sciences*, 66(1), pp. 37–45. DOI: 10.1080/08120099.2018.1525783.

Hendrikse, A. and L. Spreeuwers (2007). "Component ordering in independent component analysis based on data power". In: *Proceedings of the 28th Symposium on Information Theory in the Benelux*. Ed. by R. Veldhuis and H. Cronie. Netherlands: Werkgemeenschap voor Informatie- en Communicatietheorie (WIC), pp. 211–218.

Hernández-Pajares, M., J. Juan, J. Sanz, and R. Orús (2007). "Second-order ionospheric term in GPS: Implementation and impact on geodetic estimates". *Journal of Geophysical Research: Solid Earth*, 112(B8). DOI: 10.1029/2006jb004707.

Herring, T., M. Floyd, R. King, and S. McClusky (2015). *Globk Reference Manual, Global Kalman filter VLBI and GPS analysis program*. Report. Massachusetts Institute of Technology.

Hillis, R., M. Sandiford, S. Reynolds, and M. Quigley (2008). "Present-day stresses, seismicity and Neogene-to-Recent tectonics of Australia's 'passive' margins: intraplate deformation controlled by plate boundary forces". In: *The Nature and Origin of Compression in Passive Margins*. Ed. by H. Johnson, T. Doré, R. Gatliff, R. Holdsworth, E. Lundin, and J. Ritchie. Geological Society of London.

Hyvärinen, A. (1999a). "Fast and robust fixed-point algorithms for independent component analysis". *IEEE Transactions on Neural Networks*, 10(3), pp. 626–634. DOI: 10.1109/72.761722.

Hyvärinen, A. (1999b). "Survey on independent component analysis". *Neural Computing Surveys*, 2, pp. 94–128.

Hyvärinen, A. and E Oja (2000). "Independent component analysis: algorithms and applications". *Neural Networks*, 13(4–5), pp. 411–430. DOI: http://dx.doi.org/10.1016/S0893-6080(00)00026-5.

Hyvärinen, A., J. Särelä, and R. Vigário (1999). "Bumps and spikes: Artefacts generated by independent component analysis with insufficient sample size". In: *Workshop on Independent Component Analysis and Blind Signal Separation (ICA'99)*, pp. 425–429.

Jiang, W., Z. Li, T. van Dam, and W. Ding (2013). "Comparative analysis of different environmental loading methods and their impacts on the GPS height time series". *Journal of Geodesy*, 87(7), pp. 687–703. DOI: 10.1007/s00190-013-0642-3.

Jiang, Z., D. Huang, L. Yuan, A. Hassan, L. Zhang, and Z. Yang (2018). "Coseismic and postseismic deformation associated with the 2016 M_W 7.8 Kaikoura earthquake, New Zealand: fault movement investigation and seismic hazard analysis". *Earth, Planets and Space*, 70(1), p. 62. DOI: 10.1186/s40623-018-0827-3.

Johnston, G., N. Dando, and O. Titov (2008). *AuScope Geospatial: Towards a high resolution four-dimensional reference frame*. Report. Geoscience Australia.

Jungclaus, J., N. Fischer, H. Haak, K. Lohmann, J. Marotzke, D. Matei, U. Mikolajewicz, D. Notz, and J. von Storch (2013). "Characteristics of the ocean simulations in the Max Planck Institute Ocean Model (MPIOM) the ocean component of the MPI-Earth system model". *Journal of Advances in Modeling Earth Systems*, 5(2), pp. 422–446. DOI: 10.1002/jame.20023.

Karegar, M., T. Dixon, R. Malservisi, J. Kusche, and S. Engelhart (2017). "Nuisance Flooding and Relative Sea-Level Rise: the Importance of Present-Day Land Motion". *Scientific Reports*, 7(1), p. 11197. DOI: 10.1038/s41598-017-11544-y.

Kedar, S., G. Hajj, B. Wilson, and M. Heflin (2003). "The effect of the second order GPS ionospheric correction on receiver positions". *Geophysical Research Letters*, 30(16). DOI: 10.1029/2003gl017639.

Keep, M. and W. Schellart (2012). "Introduction to the thematic issue on the evolution and dynamics of the Indo-Australian plate". *Australian Journal of Earth Sciences*, 59(6), pp. 807–808. DOI: 10.1080/08120099.2012.708360.

Kennett, B. and S. Blewett R. (2012). "Lithospheric Framework of Australia". *Episodes*, 35(9), pp. 9–22.

King, M., M. Keshin, P. Whitehouse, I. Thomas, G. Milne, and R. Riva (2012). "Regional biases in absolute sea-level estimates from tide gauge data due to residual unmodeled vertical land movement". *Geophysical Research Letters*, 39(14). DOI: 10.1029/2012GL052348.

King, M. and A. Santamaría-Gómez (2016). "Ongoing deformation of Antarctica following recent Great Earthquakes". *Geophysical Research Letters*, 43(43), p. 5. DOI: 10.1002/2016GL067773.

King, M. and C. Watson (2010). "Long GPS coordinate time series: Multipath and geometry effects". *Journal of Geophysical Research: Solid Earth*, 115(B4), B04403. DOI: 10.1029/2009jb006543.

King, M. and C. Watson (2014). "Geodetic vertical velocities affected by recent rapid changes in polar motion". *Geophysical Journal International*, 199(2), pp. 1161–1165. DOI: 10.1093/gji/ggu325.

Klein, E., L. Fleitout, C. Vigny, and J. Garaud (2016). "Afterslip and viscoelastic relaxation model inferred from the large-scale post-seismic deformation following the 2010 M_W 8.8 Maule earthquake (Chile)". *Geophysical Journal International*, 205(3), pp. 1455–1472. DOI: 10.1093/gji/ggw086.

Klemann, V. and Z. Martinec (2011). "Contribution of glacial-isostatic adjustment to the geocenter motion". *Tectonophysics*, 511(3–4), pp. 99–108. DOI: http://dx.doi.org/10.1016/j.tecto.2009.08.031.

Klos, A., M. Bos, and J. Bogusz (2017). "Detecting time-varying seasonal signal in GPS position time series with different noise levels". *GPS Solutions*, 22(1), p. 21. DOI: 10.1007/s10291-017-0686-6.

Kogan, M. and G. Steblov (2008). "Current global plate kinematics from GPS (1995–2007) with the plate-consistent reference frame". *Journal of Geophysical Research: Solid Earth*, 113(B4). DOI: 10.1029/2007JB005353.

Konca, A., J.-P. Avouac, A. Sladen, A. Meltzner, K. Sieh, P. Fang, Z. Li, J. Galetzka, J. Genrich, M. Chlieh, D. Natawidjaja, Y. Bock, E. Fielding, C. Ji, and D. Helmberger (2008). "Partial rupture of a locked patch of the Sumatra megathrust during the 2007 earthquake sequence". *Nature*, 456, p. 631. DOI: 10.1038/nature07572https://www.nature.com/articles/nature07572#supplementary-information.

Kopp, R., R. Horton, C. Little, J. Mitrovica, M. Oppenheimer, D. Rasmussen, B. Strauss, and C. Tebaldi (2014). "Probabilistic 21st and 22nd century sea-level projections at a global network of tide-gauge sites". *Earth's Future*, 2(8), pp. 383–406. DOI: 10.1002/2014EF000239.

Kreemer, C., G. Blewitt, W. Hammond, and H.-P. Plag (2006). "Global deformation from the great 2004 Sumatra-Andaman Earthquake observed by GPS: Implications for rupture process and global reference frame". *Earth, Planets and Space*, 58(2), pp. 141–148. DOI: 10.1186/bf03353370.

Kusche, J. (2007). "Approximate decorrelation and non-isotropic smoothing of time-variable GRACE-type gravity field models". *Journal of Geodesy*, 81(11), pp. 733–749. DOI: 10.1007/s00190-007-0143-3.

Langbein, J. (2004). "Noise in two-color electronic distance meter measurements revisited". *Journal of Geophysical Research: Solid Earth*, 109(B4). DOI: 10.1029/2003JB002819.

Langbein, J. (2008). "Noise in GPS displacement measurements from Southern California and Southern Nevada". *Journal of Geophysical Research: Solid Earth*, 113(B5). DOI: 10.1029/2007JB005247.

Langbein, J. (2012). "Estimating rate uncertainty with maximum likelihood: differences between power-law and flicker–random-walk models". *Journal of Geodesy*, 86(9), pp. 775–783. DOI: 10.1007/s00190-012-0556-5.

Larson, K., J. Freymueller, and S. Philipsen (1997). "Global plate velocities from the Global Positioning System". *Journal of Geophysical Research: Solid Earth*, 102(B5), pp. 9961–9981. DOI: 10.1029/97JB00514.

Lehner, B., C. Liermann, C. Revenga, C. Vörösmarty, B. Fekete, P. Crouzet, P. Döll, M. Endejan, K. Frenken, J. Magome, C. Nilsson, J. Robertson, R. Rödel, N. Sindorf, and D. Wisser (2011). "High-resolution mapping of the world's reservoirs and dams for sustainable river-flow management". *Frontiers in Ecology and the Environment*, 9(9), pp. 494–502. DOI: 10.1890/100125.

Lekić, V. and B. Romanowicz (2011). "Inferring upper-mantle structure by full waveform tomography with the spectral element method". *Geophysical Journal International*, 185(2), pp. 799–831. DOI: 10.1111/j.1365-246X.2011.04969.x.

Lettenmaier, D. and J. Famiglietti (2006). "Water from on high". *Nature*, 444, p. 562. DOI: 10.1038/444562a.

Li, W., Y. Shen, and B. Li (2015). "Weighted spatiotemporal filtering using principal component analysis for analyzing regional GNSS position time series". *Acta Geodaetica et Geophysica*, 50(4), pp. 419–436. DOI: 10.1007/s40328-015-0100-1.

Li, Z., J. Yue, W. Li, and D. Lu (2017). "Investigating mass loading contributes of annual GPS observations for the Eurasian plate". *Journal of Geodynamics*, 111, pp. 43–49. DOI: https://doi.org/10.1016/j.jog.2017.07.001.

Liu, B., W. Dai, and N. Liu (2017). "Extracting seasonal deformations of the Nepal Himalaya region from vertical GPS position time series using Independent Component Analysis". *Advances in Space Research*, 60(12), pp. 2910–2917. DOI: https://doi.org/10.1016/j.asr.2017.02.028.

Liu, B., W. Dai, W. Peng, and X. Meng (2015). "Spatiotemporal analysis of GPS time series in vertical direction using independent component analysis". *Earth, Planets and Space*, 67(1), pp. 1–10. DOI: 10.1186/s40623-015-0357-1.

Liu, B., M. King, and W. Dai (2018). "Common mode error in Antarctic GPS coordinate time-series on its effect on bedrock-uplift estimates". *Geophysical Journal International*, 214(3), pp. 1652–1664. DOI: 10.1093/gji/ggy217.

Machette, M., A. Crone, and J. Bowman (1993). *Geologic investigations of the 1986 Marryat Creek, Australia, earthquake — implications for paleoseismicity in stable continental regions*. Report. United States Geological Survey Bulletin 2032-B.

Mahesh, P., B. Kundu, J. Catherine, and V. Gahalaut (2011). "Anatomy of the 2009 Fiordland earthquake (M_W 7.8), South Island, New Zealand". *Geoscience Frontiers*, 2(1), pp. 17–22. DOI: http://dx.doi.org/10.1016/j.gsf.2010.12.002.

Mao, A., C. Harrison, and T. Dixon (1999). "Noise in GPS coordinate time series". *Journal of Geophysical Research: Solid Earth*, 104(B2), pp. 2797–2816. DOI: 10.1029/1998jb900033.

Marone, C. (1998). "Laboratory-derived friction laws and their application to seismic faulting". *Annual Review of Earth and Planetary Sciences*, 26(1), pp. 643–696. DOI: 10.1146/annurev.earth.26.1.643.

Martín-Español, A., M. King, A. Zammit-Mangion, S. Andrews, P. Moore, and J. Bamber (2016). "An assessment of forward and inverse GIA solutions for Antarctica". *Journal of Geophysical Research: Solid Earth*, 121(9), pp. 6947–6965. DOI: 10.1002/2016JB013154.

Marzeion, B., P. Leclercq, J. Cogley, and A. Jarosch (2015). "Brief Communication: Global reconstructions of glacier mass change during the 20th century are consistent". *The Cryosphere*, 9(6), 2399–2404. DOI: 10.5194/tc-9-2399-2015.

McClusky, S., S. Balassanian, A. Barka, C. Demir, S. Ergintav, I. Georgiev, O. Gurkan, M. Hamburger, K. Hurst, H. Kahle, K. Kastens, G. Kekelidze, R. King, V. Kotzev, O. Lenk, S. Mahmoud, A. Mishin, M. Nadariya, A. Ouzounis, D. Paradiddid, Y. Peter, M. Prilepin, R. Reiliinger, I. Sanil, H. Seeger, A. Taeleb, M. Toksoz, and G. Veis (2000). "Global Positioning System constraints on plate kinematics and dynamics in the eastern Mediterranean and Caucasus". *Journal of Geophysical Research: Solid Earth*, 105(B3), pp. 5695–5719. DOI: 10.1029/1999JB900351.

McCue, K., B. Barlow, D. Denham, T. Jones, G. Gibson, and M. Michael-Leiba (1987). "Another chip off the old Australian block". *Eos, Transactions American Geophysical Union*, 68(26), pp. 609–612. DOI: 10.1029/EO068i026p00609.

McCue, K., V. Wesson, and G. Gibson (1990). "The Newcastle, New South Wales, earthquake of 28 December 1989". *BMR Journal of Australian Geology & Geophysics*, 11(4), pp. 559–568.

Métivier, L., X. Collilieux, D. Lercier, Z. Altamimi, and F. Beauducel (2014). "Global coseismic deformations, GNSS time series analysis, and earthquake scaling laws". *Journal of Geophysical Research: Solid Earth*, 2014JB011280. DOI: 10.1002/2014jb011280.

Métivier, L., M. Greff-Lefftz, and Z. Altamimi (2010). "On secular geocenter motion: The impact of climate changes". *Earth and Planetary Science Letters*, 296(3–4), pp. 360–366. DOI: http://dx.doi.org/10.1016/j.epsl.2010.05.021.

Métivier, L., H. Rouby, P. Rebischung, and Z. Altamimi (2020). "ITRF2014, Earth figure changes, and geocenter velocity: implications for GIA and recent ice melting". *Journal of Geophysical Research: Solid Earth*, 124. DOI: 10.1029/2019jb018333.

Meyrath, T., T. van Dam, X. Collilieux, and P. Rebischung (2017). "Seasonal low-degree changes in terrestrial water mass load from global GNSS measurements". *Journal of Geodesy*, pp. 1–22. DOI: 10.1007/s00190-017-1028-8.

Ming, F., Y. Yang, A. Zeng, and B. Zhao (2017). "Spatiotemporal filtering for regional GPS network in China using independent component analysis". *Journal of Geodesy*, 91(4), pp. 419–440. DOI: 10.1007/s00190-016-0973-y.

Mitrovica, J. and G. Milne (2002). "On the origin of late Holocene sea-level highstands within equatorial ocean basins". *Quaternary Science Reviews*, 21(20–22), pp. 2179–2190. DOI: http://dx.doi.org/10.1016/S0277-3791(02)00080-X.

Mitrovica, J., M. Tamisiea, J. Davis, and G. Milne (2001). "Recent mass balance of polar ice sheets inferred from patterns of global sea-level change". *Nature*, 409(6823), pp. 1026–1029. DOI: http://www.nature.com/nature/journal/v409/n6823/suppinfo/4091026a0_S1.html.

Moore, M., C. Watson, M. King, S. McClusky, and P. Tregoning (2014). "Empirical modelling of site-specific errors in continuous GPS data". *Journal of Geodesy*, 88(9), pp. 887–900. DOI: 10.1007/s00190-014-0729-5.

Müller, D. and M. Seton (2015). "Plate Motion". In: *Encyclopedia of Marine Geosciences*. Ed. by J. Harff, M. Meschede, S. Petersen, and J. Thiede. Netherlands: Springer, pp. 1–10. DOI: 10.1007/978-94-007-6644-0_131-1.

Márquez-Azúa, B. and C. DeMets (2009). "Deformation of Mexico from continuous GPS from 1993 to 2008". *Geochemistry, Geophysics, Geosystems*, 10(2). DOI: 10.1029/2008GC002278.

Nikolaidis, R. (2002). "Observation of geodetic and seismic deformation with the Global Positioning System". Thesis.

Nocquet, J., E. Calais, and B. Parsons (2005). "Geodetic constraints on glacial isostatic adjustment in Europe". *Geophysical Research Letters*, 32(6). DOI: 10.1029/2004GL022174.

Noël, B., W. van de Berg, E. van Meijgaard, P. Kuipers Munneke, R. van de Wal, and M. van den Broeke (2015). "Evaluation of the updated regional climate model RACMO2.3: summer snowfall impact on the Greenland Ice Sheet". *The Cryosphere*, 9(5), pp. 1831–1844. DOI: 10.5194/tc-9-1831-2015.

Ostanciaux, E., L. Husson, G. Choblet, C. Robin, and K. Pedoja (2012). "Present-day trends of vertical ground motion along the coast lines". *Earth-Science Reviews*, 110(1), pp. 74–92. DOI: https://doi.org/10.1016/j.earscirev.2011.10.004.

Otsubo, T., K. Matsuo, Y. Aoyama, K. Yamamoto, T. Hobiger, T. Kubo-oka, and M. Sekido (2016). "Effective expansion of satellite laser ranging network to improve global geodetic parameters". *Earth, Planets and Space*, 68(1), pp. 1–7. DOI: 10.1186/s40623-016-0447-8.

Peltier, W. (2004). "Global Glacial Isostasy and the Surface of the Ice-Age Earth: The ICE-5G (VM2) Model and GRACE". *Annual Review of Earth and Planetary Sciences*, 32(1), pp. 111–149. DOI: doi:10.1146/annurev.earth.32.082503.144359.

Peltier, W., D. Argus, and R. Drummond (2015). "Space geodesy constrains ice age terminal deglaciation: The global ICE-6G_C (VM5a) model". *Journal of Geophysical Research: Solid Earth*, 120(1), pp. 450–487. DOI: 10.1002/2014jb011176.

Petit, G. and B. Luzum (2010). *IERS Conventions*. Report.

Petrie, E., M. Hernández-Pajares, P. Spalla, P. Moore, and M. King (2011). "A Review of Higher Order Ionospheric Refraction Effects on Dual Frequency GPS". *Surveys in Geophysics*, 32(3), pp. 197–253. DOI: 10.1007/s10712-010-9105-z.

Petrov, L. (2015). "The International Mass Loading Service". DOI: arXiv:1503.00191.

Pfeffer, J. and P. Allemand (2016). "The key role of vertical land motions in coastal sea level variations: A global synthesis of multisatellite altimetry, tide gauge data and GPS measurements". *Earth and Planetary Science Letters*, 439, pp. 39–47. DOI: http://dx.doi.org/10.1016/j.epsl.2016.01.027.

Pfeffer, J., G. Spada, A. Mémin, J. Boy, and P. Allemand (2017). "Decoding the origins of vertical land motions observed today at coasts". *Geophysical Journal International*, 210(1), pp. 148–165. DOI: 10.1093/gji/ggx142.

Polcari, M., M. Albano, S. Atzori, C. Bignami, and S. Stramondo (2018). "The Causative Fault of the 2016 M_{wp} 6.1 Petermann Ranges Intraplate Earthquake (Central Australia) Retrieved by C- and L-Band InSAR Data". *Remote Sensing*, 10(8), p. 1311.

Pollitz, F. (1992). "Postseismic relaxation theory on the spherical earth". *Bulletin of the Seismological Society of America*, 82(1), pp. 422–453.

Pollitz, F. (1996). "Coseismic Deformation From Earthquake Faulting On A Layered Spherical Earth". *Geophysical Journal International*, 125(1), pp. 1–14. DOI: 10.1111/j.1365-246X.1996.tb06530.x.

Pollitz, F. (1997). "Gravitational viscoelastic postseismic relaxation on a layered spherical Earth". *Journal of Geophysical Research: Solid Earth*, 102(B8), pp. 17921–17941. DOI: 10.1029/97JB01277.

Press, W., S. Teukolsky, W. Vetterling, and B. Flannery (1992). *Numerical recipes in C (2nd ed.): the art of scientific computing*. Cambridge University Press, p. 994.

Purcell, A., P. Tregoning, and A. Dehecq (2016). "An assessment of the ICE6G_C(VM5a) glacial isostatic adjustment model". *Journal of Geophysical Research: Solid Earth*, 121(5), pp. 3939–3950. DOI: 10.1002/2015JB012742.

Rajabi, M., M. Tingay, O. Heidbach, R. Hillis, and S. Reynolds (2017). "The present-day stress field of Australia". *Earth-Science Reviews*, 168, pp. 165–189. DOI: https://doi.org/10.1016/j.earscirev.2017.04.003.

Ray, J., Z. Altamimi, X. Collilieux, and T. van Dam (2007). "Anomalous harmonics in the spectra of GPS position estimates". *GPS Solutions*, 12(1), pp. 55–64. DOI: 10.1007/s10291-007-0067-7.

Reichle, R., C. Draper, Q. Liu, M. Girotto, S. Mahanama, R. Koster, and G. Lannoy (2017). "Assessment of MERRA-2 Land Surface Hydrology Estimates". *Journal of Climate*, 30(8), pp. 2937–2960. DOI: 10.1175/jcli-d-16-0720.1.

Revets, S. A., M. Keep, and B. L. N. Kennett (2009). "NW Australian intraplate seismicity and stress regime". *Journal of Geophysical Research: Solid Earth*, 114(B10). DOI: 10.1029/2008jb006152.

Riddell, A., M. King, and C. Watson (2020). "Present-Day Vertical Land Motion of Australia From GPS Observations and Geophysical Models". *Journal of Geophysical Research: Solid Earth*, 125(2), e2019JB018034. DOI: 10.1029/2019jb018034.

Riddell, A., M. King, C. Watson, Y. Sun, R. Riva, and R. Rietbroek (2017). "Uncertainty in geocenter estimates in the context of ITRF2014". *Journal of Geophysical Research: Solid Earth*, 122(5), pp. 4020–4032. DOI: 10.1002/2016JB013698.

Rietbroek, R. (2015). "Global and Regional Sea level budget components from GRACE and radar altimetry (2002-2014)". *Supplement to: Rietbroek, Roelof; Brunnabend, Sandra-Ester; Kusche, Jürgen; Schröter, Jens; Dahle, Christoph (2016): Revisiting the Contemporary Sea Level Budget on Global and Regional Scales. Proceedings of the National Academy of Sciences, 113, 1504-1509*, DOI: 10.1594/PANGAEA.855539.

Rietbroek, R., S.-E. Brunnabend, J. Kusche, J. Schröter, and C. Dahle (2016). "Revisiting the contemporary sea-level budget on global and regional scales". *Proceedings of the National Academy of Sciences*, 113(6), pp. 1504–1509. DOI: 10.1073/pnas.1519132113.

Riva, R., T. Frederikse, M. King, B. Marzeion, and M. van den Broeke (2017). "Brief communication: The global signature of post-1900 land ice wastage on vertical land motion". *The Cryosphere*, 11(3), pp. 1327–1332. DOI: 10.5194/tc-11-1327-2017.

Rodell, M., P. Houser, U. Jambor, J. Gottschalck, K. Mitchell, C.-J. Meng, K. Arsenault, B. Cosgrove, J. Radakovich, M. Bosilovich, J. Entin*, J. Walker, D. Lohmann, and D. Toll (2004). "The Global Land Data Assimilation System". *Bulletin of the American Meteorological Society*, 85(3), pp. 381–394. DOI: doi:10.1175/BAMS-85-3-381.

Ruddick, R. and J. Dawson (1990). *Geodesy - Continuously Operating*. Dataset. DOI: http://dx.doi.org/10.4225/25/552B5AAD0C34A.

Sakumura, C., S. Bettadpur, and S. Bruinsma (2014). "Ensemble prediction and intercomparison analysis of GRACE time-variable gravity field models". *Geophysical Research Letters*, 41(5), pp. 1389–1397. DOI: 10.1002/2013GL058632.

Sandiford, M. (2007). "The tilting continent: A new constraint on the dynamic topographic field from Australia". *Earth and Planetary Science Letters*, 261(1), pp. 152–163. DOI: https://doi.org/10.1016/j.epsl.2007.06.023.

Sandiford, M., W. Malcolm, and C. David (2004). "Origin of the in situ stress field in south-eastern Australia". *Basin Research*, 16(3), pp. 325–338. DOI: 10.1111/j.1365-2117.2004.00235.x.

Sandiford, M. and D. L. Egholm (2008). "Enhanced intraplate seismicity along continental margins: Some causes and consequences". *Tectonophysics*, 457(3), pp. 197–208. DOI: https://doi.org/10.1016/j.tecto.2008.06.004.

Santamaría-Gómez, A., M.-N. Bouin, X. Collilieux, and G. Wöppelmann (2011). "Correlated errors in GPS position time series: Implications for velocity estimates". *Journal of Geophysical Research: Solid Earth*, 116(B1), B01405. DOI: 10.1029/2010jb007701.

Santamaría-Gómez, A., M.-N. Bouin, X. Collilieux, and G. Wöppelmann (2013). "Time-Correlated GPS Noise Dependency on Data Time Period". In: *Reference Frames for Applications in Geosciences*. Ed. by Z. Altamimi and X. Collilieux. Berlin, Heidelberg: Springer Berlin Heidelberg, pp. 119–124. DOI: 10.1007/978-3-642-32998-2_19.

Santamaría-Gómez, A., M. Gravelle, X. Collilieux, M. Guichard, B. Míguez, P. Tiphaneau, and G. Wöppelmann (2012). "Mitigating the effects of vertical land motion in tide gauge records using a state-of-the-art GPS velocity field". *Global and Planetary Change*, 98–99, pp. 6–17. DOI: http://dx.doi.org/10.1016/j.gloplacha.2012.07.007.

Santamaría-Gómez, A., M. Gravelle, S. Dangendorf, M. Marcos, G. Spada, and G. Wöppelmann (2017). "Uncertainty of the 20th century sea-level rise due to vertical land motion errors". *Earth and Planetary Science Letters*, 473, pp. 24–32. DOI: https://doi.org/10.1016/j.epsl.2017.05.038.

Santamaría-Gómez, A. and A. Mémin (2015). "Geodetic secular velocity errors due to interannual surface loading deformation". *Geophysical Journal International*, 202(2), pp. 763–767. DOI: 10.1093/gji/ggv190.

Schumacher, M., M. King, J. Rougier, Z. Sha, S. Khan, and J. Bamber (2018). "A new global GPS data set for testing and improving modelled GIA uplift rates". *Geophysical Journal International*, 214(3), pp. 2164–2176. DOI: 10.1093/gji/ggy235.

Schwarz, G. (1978). "Estimating the Dimension of a Model". *The Annals of Statistics*, 6(2), pp. 461–464. DOI: 10.1214/aos/1176344136.

Seeber, L. and J. Armbruster (2000). "Earthquakes as beacons of stress change". *Nature*, 407, p. 69. DOI: 10.1038/35024055.

Sella, G., S. Stein, T. Dixon, M. Craymer, T. James, S. Mazzotti, and R. Dokka (2007). "Observation of glacial isostatic adjustment in "stable" North America with GPS". *Geophysical Research Letters*, 34(2). DOI: 10.1029/2006GL027081.

Serpelloni, E., C. Faccenna, G. Spada, D. Dong, and S. Williams (2013). "Vertical GPS ground motion rates in the Euro-Mediterranean region: New evidence of velocity gradients at different spatial scales along the Nubia-Eurasia plate boundary". *Journal of Geophysical Research: Solid Earth*, 118(11), pp. 6003–6024. DOI: 10.1002/2013JB010102.

Shen, Y., W. Li, G. Xu, and B. Li (2014). "Spatiotemporal filtering of regional GNSS network's position time series with missing data using principal component analysis". *Journal of Geodesy*, 88(1), pp. 1–12. DOI: 10.1007/s00190-013-0663-y.

Spatar, C., P. Moore, and P. Clarke (2015). "Collinearity assessment of geocentre coordinates derived from multi-satellite SLR data". *Journal of Geodesy*, 89(12), pp. 1197–1216. DOI: 10.1007/s00190-015-0845-x.

Steffen, W., J. Hunter, and L. Hughes (2014). *Counting the costs: climate change and coastal flooding*. Report. Climate Council of Australia Ltd.

Steffen, W., K. Mallon, T. Kompas, A. Dean, and M. Rice (2019). *Compound Costs: How climate change is damaging Australia's economy*. Report. Climate Council of Australia Ltd.

Stein, R. (1999). "The role of stress transfer in earthquake occurrence". *Nature*, 402, p. 605. DOI: 10.1038/45144.

Sun, Y., R. Riva, P. Ditmar, and R. Rietbroek (2019). "Using GRACE to Explain Variations in the Earth's Oblateness". *Geophysical Research Letters*, 46(1), pp. 158–168. DOI: 10.1029/2018gl080607.

Swenson, S., D. Chambers, and J. Wahr (2008). "Estimating geocenter variations from a combination of GRACE and ocean model output". *Journal of Geophysical Research: Solid Earth*, 113(B8). DOI: 10.1029/2007JB005338.

Tamisiea, M. (2011). "Ongoing glacial isostatic contributions to observations of sea level change". *Geophysical Journal International*, 186(3), pp. 1036–1044. DOI: 10.1111/j.1365-246X.2011.05116.x.

Tamisiea, M., E. Hill, R. Ponte, J. Davis, I. Velicogna, and N. Vinogradova (2010). "Impact of self-attraction and loading on the annual cycle in sea level". *Journal of Geophysical Research: Oceans*, 115(C7). DOI: 10.1029/2009JC005687.

Tamisiea, M. and J. Mitrovica (2011). "The moving boundaries of sea level change: Understanding the origins of geographic variability". *Oceanography*, 24(2), pp. 24–39. DOI: 10.5670/oceanog.2011.25.

Teferle, F., R. Bingley, E. Orliac, S. Williams, P. Woodworth, D. McLaughlin, T. Baker, I. Shennan, G. Milne, S. Bradley, and D. Hansen (2009). "Crustal motions in Great Britain: evidence from continuous GPS, absolute gravity and Holocene sea level data". *Geophysical Journal International*, 178(1), pp. 23–46. DOI: 10.1111/j.1365-246X.2009.04185.x.

Thom, A. (2017). "Australian Earthquakes 2016". In: *Australian Earthquake Engineering Society 2017 Conference*.

Toscano, M. A., W. R. Peltier, and R. Drummond (2011). "ICE-5G and ICE-6G models of postglacial relative sea-level history applied to the Holocene coral reef record of northeastern St Croix, U.S.V.I.: investigating the influence of rotational feedback on GIA processes at tropical latitudes". *Quaternary Science Reviews*, 30(21), pp. 3032–3042. DOI: https://doi.org/10.1016/j.quascirev.2011.07.018.

Tregoning, P., R. Burgette, S. McClusky, S. Lejeune, C. Watson, and H. McQueen (2013). "A decade of horizontal deformation from great earthquakes". *Journal of Geophysical Research: Solid Earth*, 118(5), pp. 2371–2381. DOI: 10.1002/jgrb.50154.

Tregoning, P. and T. van Dam (2005). "Effects of atmospheric pressure loading and seven-parameter transformations on estimates of geocenter motion and station heights from space geodetic observations". *Journal of Geophysical Research: Solid Earth*, 110(B3). DOI: 10.1029/2004JB003334.

Tregoning, P. and T. Herring (2006). "Impact of a priori zenith hydrostatic delay errors on GPS estimates of station heights and zenith total delays". *Geophysical Research Letters*, 33(23). DOI: 10.1029/2006GL027706.

Tregoning, P. and C. Watson (2009). "Atmospheric effects and spurious signals in GPS analyses". *Journal of Geophysical Research: Solid Earth*, 114(B9), B09403. DOI: 10.1029/2009jb006344.

Trubienko, O., L. Fleitout, J.-D. Garaud, and C. Vigny (2013). "Interpretation of interseismic deformations and the seismic cycle associated with large subduction earthquakes". *Tectonophysics*, 589, pp. 126–141. DOI: http://dx.doi.org/10.1016/j.tecto.2012.12.027.

Trubienko, O., J. Garaud, and L. Fleitout (2014). "Models of postseismic deformation after megaearthquakes: the role of various rheological and geometrical parameters of the subduction zone". *Solid Earth Discuss.* 2014, pp. 427–466. DOI: 10.5194/sed-6-427-2014.

Twardzik, C., M. Vergnolle, A. Sladen, and A. Avallone (2019). "Unravelling the contribution of early postseismic deformation using sub-daily GNSS positioning". *Scientific Reports*, 9(1), p. 1775. DOI: 10.1038/s41598-019-39038-z.

van Dam, T., X. Collilieux, J. Wuite, Z. Altamimi, and J. Ray (2012). "Nontidal ocean loading: amplitudes and potential effects in GPS height time series". *Journal of Geodesy*, 86(11), pp. 1043–1057. DOI: 10.1007/s00190-012-0564-5.

van Dam, T., J. Wahr, P. Milly, A. Shmakin, G. Blewitt, D. Lavallée, and K. Larson (2001). "Crustal displacements due to continental water loading". *Geophysical Research Letters*, 28(4), pp. 651–654. DOI: 10.1029/2000GL012120.

van Dam, T., G. Blewitt, and M. Heflin (1994). "Atmospheric pressure loading effects on Global Positioning System coordinate determinations". *Journal of Geophysical Research: Solid Earth*, 99(B12), pp. 23939–23950. DOI: 10.1029/94jb02122.

van den Broeke, M., E. Enderlin, I. Howat, P. Kuipers Munneke, B. Noël, W. van de Berg, E. van Meijgaard, and B. Wouters (2016). "On the recent contribution of the Greenland ice sheet to sea level change". *The Cryosphere*, 10(5), pp. 1933–1946. DOI: 10.5194/tc-10-1933-2016.

van der Wal, W., P. Whitehouse, and E. Schrama (2015). "Effect of GIA models with 3D composite mantle viscosity on GRACE mass balance estimates for Antarctica". *Earth and Planetary Science Letters*, 414, pp. 134–143. DOI: https://doi.org/10.1016/j.epsl.2015.01.001.

Varghese, T. (2013). "Engineering Changes to the NASA SLR Network to Overcome Obsoleteness, Improve Performance and Reliability". In: *Eighteenth International Workshop on Laser Ranging Instrumentation*.

Wada, Y., L. van Beek, C. van Kempen, J. Reckman, S. Vasak, and M. Bierkens (2010). "Global depletion of groundwater resources". *Geophysical Research Letters*, 37(20). DOI: 10.1029/2010GL044571.

Walwer, D., E. Calais, and M. Ghil (2016). "Data-adaptive detection of transient deformation in geodetic networks". *Journal of Geophysical Research: Solid Earth*, 121(3), pp. 2129–2152. DOI: 10.1002/2015JB012424.

Wang, K., Y. Hu, and J. He (2012). "Deformation cycles of subduction earthquakes in a viscoelastic Earth". *Nature*, 484(7394), pp. 327–332.

Wang, K., Y. Ma, W. Jiang, Z. Li, H. Chen, and L. Deng (2018). "Improved vertical displacements induced by a refined thermal expansion model and its quantitative analysis in GPS height time series". *Journal of Geophysics and Engineering*, 15(2), pp. 554–567. DOI: 10.1088/1742-2140/aa93ae.

Wang, L., C. Chen, J. Du, and T. Wang (2017). "Detecting seasonal and long-term vertical displacement in the North China Plain using GRACE and GPS". *Hydrology and Earth System Science*, 21(6), pp. 2905–2922. DOI: 10.5194/hess-21-2905-2017.

Watson, C., R. Burgette, P. Tregoning, N. White, J. Hunter, R. Coleman, R. Handsworth, and H. Brolsma (2010). "Twentieth century constraints on sea level change and earthquake deformation at Macquarie Island". *Geophysical Journal International*, 182(2), pp. 781–796. DOI: 10.1111/j.1365-246X.2010.04640.x.

Watson, C. S., N. J. White, J. A. Church, M. A. King, R. J. Burgette, and B. Legresy (2015). "Unabated global mean sea-level rise over the satellite altimeter era". *Nature Clim. Change*, advance online publication. DOI: 10.1038/nclimate2635http://www.nature.com/nclimate/journal/vaop/ncurrent/abs/nclimate2635.html#supplementary-information.

Wdowinski, S., Y. Bock, J. Zhang, P. Fang, and J. Genrich (1997). "Southern California permanent GPS geodetic array: Spatial filtering of daily positions for estimating coseismic and postseismic displacements induced by the 1992 Landers earthquake". *Journal of Geophysical Research: Solid Earth*, 102(B8), pp. 18057–18070. DOI: 10.1029/97JB01378.

Webb, T. and M. Lowry (1982). "The Puysegur Bank earthquake of 1979 October 12". *New Zealand Journal of Geology and Geophysics*, 25(4), pp. 383–395. DOI: 10.1080/00288306.1982.10421505.

White, N., I. Haigh, J. Church, T. Koen, C. Watson, T. Pritchard, P. Watson, R. Burgette, K. McInnes, Z.-J. You, X. Zhang, and P. Tregoning (2014). "Australian sea levels—Trends, regional variability and influencing factors". *Earth-Science Reviews*, 136(0), pp. 155–174. DOI: http://dx.doi.org/10.1016/j.earscirev.2014.05.011.

Whitehouse, P. (2018). "Glacial isostatic adjustment modelling: historical perspectives, recent advances, and future directions". *Earth Surface Dynamics*, 6(2), pp. 401–429. DOI: 10.5194/esurf-6-401-2018.

Williams, S. (2003a). "Offsets in Global Positioning System time series". *Journal of Geophysical Research: Solid Earth*, 108(B6). DOI: 10.1029/2002JB002156.

Williams, S. (2003b). "The effect of coloured noise on the uncertainties of rates estimated from geodetic time series". *Journal of Geodesy*, 76(9-10), pp. 483–494. DOI: 10.1007/s00190-002-0283-4.

Williams, S., Y. Bock, P. Fang, P. Jamason, R. Nikolaidis, L. Prawirodirdjo, M. Miller, and D. Johnson (2004). "Error analysis of continuous GPS position time series". *Journal of Geophysical Research: Solid Earth*, 109(B3). DOI: 10.1029/2003jb002741.

Williams, S. and N. Penna (2011). "Non-tidal ocean loading effects on geodetic GPS heights". *Geophysical Research Letters*, 38(9). DOI: 10.1029/2011GL046940.

Wöppelmann, G., C. Letetrel, A. Santamaria, M. Bouin, X. Collilieux, Z. Altamimi, S. Williams, and B. Miguez (2009). "Rates of sea-level change over the past century in a geocentric reference frame". *Geophysical Research Letters*, 36(12). DOI: 10.1029/2009gl038720.

Wöppelmann, G. and M. Marcos (2016). "Vertical land motion as a key to understanding sea level change and variability". *Reviews of Geophysics*, 54(1), pp. 64–92. DOI: 10.1002/2015RG000502.

Wu, X., X. Collilieux, Z. Altamimi, B. Vermeersen, R. Gross, and I. Fukumori (2011). "Accuracy of the International Terrestrial Reference Frame origin and Earth expansion". *Geophysical Research Letters*, 38(13). DOI: 10.1029/2011GL047450.

Wu, X., J. Ray, and T. van Dam (2012). "Geocenter motion and its geodetic and geophysical implications". *Journal of Geodynamics*, 58, pp. 44–61. DOI: http://dx.doi.org/10.1016/j.jog.2012.01.007.

Xu, X., D. Dong, M. Fang, Y. Zhou, N. Wei, and F. Zhou (2017). "Contributions of thermoelastic deformation to seasonal variations in GPS station position". *GPS Solutions*, pp. 1–10. DOI: 10.1007/s10291-017-0609-6.

Yan, H., W. Chen, Y. Zhu, W. Zhang, and M. Zhong (2009). "Contributions of thermal expansion of monuments and nearby bedrock to observed GPS height changes". *Geophysical Research Letters*, 36(13). DOI: 10.1029/2009GL038152.

Yong, C. Z., P. H. Denys, and C. F. Pearson (2017). "Present-day kinematics of the Sundaland plate". *Journal of Applied Geodesy*, 11(3), pp. 169–177. DOI: https://doi.org/10.1515/jag-2016-0024.

Yue, H., T. Lay, and K. Koper (2012). "En echelon and orthogonal fault ruptures of the 11 April 2012 great intraplate earthquakes". *Nature*, 490(7419), pp. 245–249. DOI: 10.1038/nature11492.

Zerbini, S., F. Raicich, M. Errico, and G. Cappello (2013). "An EOF and SVD analysis of interannual variability of GPS coordinates, environmental parameters and space gravity data". *Journal of Geodynamics*, 67, pp. 111–124. DOI: http://doi.org/10.1016/j.jog.2012.04.006.

Zhang, J., Y. Bock, H. Johnson, P. Fang, S. Williams, J. Genrich, S. Wdowinski, and J. Behr (1997). "Southern California permanent GPS geodetic array: Error analysis of daily position estimates and site velocities". *Journal of Geophysical Research: Solid Earth*, 102(B8), pp. 18035–18055. DOI: 10.1029/97JB01380.

Zumberge, J., M. Heflin, D. Jefferson, M. Watkins, and F. Webb (1997). "Precise point positioning for the efficient and robust analysis of GPS data from large networks". *Journal of Geophysical Research: Solid Earth*, 102(B3), pp. 5005–5017. DOI: 10.1029/96JB03860.

Appendix A

Supporting Information for Chapter 2

A.1 Constituent datasets

Further description of the constituent datasets that are included in the Mass Surface Model (MSM) dataset are provided here.

Antarctica and Greenland: Surface mass balance estimates are based on the Regional Atmospheric Climate Model (RACMO) 2.3 (Noël et al., 2015). For ice discharge over Greenland, the data from van den Broeke et al. (2016) is used. For ice discharge over Antarctica, a model is developed based on Gravity Recovery and Climate Experiment (GRACE) and Ice-sheet Mass Balance Inter-comparison Exercise (IMBIE) (www.imbie.org).

Dam Retention: Annual dam retention data is based on Global Reservoir and Dam (GRanD) database (http://www.gwsp.org/products/html). Rates estimates are based on the method proposed by Chao et al. (2008). Monthly estimates are obtained based on a linear interpolation.

Groundwater Depletion: Groundwater pumped away by humans that is not replaced. The data is from Wada et al. (2010). The dataset is not available after 2010. To make the time series consistent with other components, annual and semi-annual variations, and linear trend are estimated and then the data series is extrapolated from 2011 to 2014.

Glaciers: Annual glacier mass balance estimates are based on Marzeion et al. (2015). Monthly data is obtained based on a linear interpolation.

Atmosphere over land and Ocean Bottom Pressure: The atmospheric contribution over land and Ocean Bottom Pressure (OBP) are all sourced from the Atmosphere and Ocean Dealiasing level-1B (AOD1B) product (Flechtner et al., 2015), which is constructed from the European Centre for Medium-range Weather Forecasts (ECMWF) and Ocean Model for Circulation and Tides (OMCT) datasets.

Terrestrial Water Storage: The Noah Global Land Data Assimilation System (GLDAS) products (Rodell et al., 2004) currently contains snow, soil moisture and canopy contributions (the surface water and groundwater components are not included). The GLDAS Noah v1 is used (variables considered are the same as described by `http://grace.jpl.nasa.gov/data/get-data/land-water-content/`). Note that Greenland and the periphery area (300 km) are masked out as snow and ice dynamics are poorly modelled there.

Self Attraction and Loading Effects: To ensure mass conservation, the non-zero total mass of all considered components is balanced by adding/removing water from oceans. The distribution of this added/removed water layer is not uniform, but should follow footprints (Mitrovica et al., 2001) calculated by solving the sea level equation after taking into account Self-Attraction and Loading system effects (Gordeev et al., 1977; Tamisiea et al., 2010).

A more detailed description of the datasets for Antarctica, Greenland, glaciers, dam retention and groundwater depletion can be found in the online supplement to Frederikse et al. (2016).

A.2 Copyright and License details

JOHN WILEY AND SONS LICENSE TERMS AND CONDITIONS

Jun 04, 2019

This Agreement between University of Tasmania -- Anna Riddell ("You") and John Wiley and Sons ("John Wiley and Sons") consists of your license details and the terms and conditions provided by John Wiley and Sons and Copyright Clearance Center.

License Number	4602150569098
License date	Jun 04, 2019
Licensed Content Publisher	John Wiley and Sons
Licensed Content Publication	Journal of Geophysical Research: Solid Earth
Licensed Content Title	Uncertainty in geocenter estimates in the context of ITRF2014
Licensed Content Author	Anna R. Riddell, Matt A. King, Christopher S. Watson, et al
Licensed Content Date	May 13, 2017
Licensed Content Volume	122
Licensed Content Issue	5
Licensed Content Pages	13
Type of use	Dissertation/Thesis
Requestor type	Author of this Wiley article
Format	Print and electronic
Portion	Full article
Will you be translating?	No
Title of your thesis / dissertation	Vertical Land Motion of the Australian Plate
Expected completion date	Jul 2019
Expected size (number of pages)	100
Requestor Location	University of Tasmania 85 Beaurepaire Crescent Holt, ACT 2615 Australia Attn: University of Tasmania
Publisher Tax ID	EU826007151
Total	0.00 AUD

Appendix B

Supporting Information for Chapter 3

B.1 Overview

This supporting information provides a detailed description of the GPS data processing in section B.2 and a list of the GPS sites in Table B.1. The daily RINEX files for each GPS site can be accessed from the Geoscience Australia ftp website: `ftp://ftp.ga.gov.au/geodesy-outgoing/gnss/data`. Table B.2 provides evidence for the result that shortening the GPS series to six years has no adverse effects on the noise characteristics of the time series. Figures B.1 and B.2 show the additional semi-variogram plots of the GPS and GIA models. Figure B.3 shows the second modes for PCA and ICA to complement Figure 3.4 of the main text.

B.2 GPS processing

Daily GPS data from the Geoscience Australia data archive was processed using the GIPSY/OASIS II software, version 6.3, developed at NASA Jet Propulsion Laboratory (JPL), with no net rotation Earth orientation parameters, satellite orbit and satellite clock fiducial-free final products using the precise point positioning technique.

Absolute phase centre offsets for the ground antennas with elevation and azimuth dependent corrections were applied. Observations below 10 degrees were excluded and elevation dependent weighting (square-root sine) were applied to minimise the effects of mis-modelled antenna phase centre variation and mis-modelled low-elevation troposphere errors. Absolute corrections were also applied for satellite antennas with block-specific nadir angle-dependent, and satellite-specific antenna phase centre offsets used. Satellite arcs with a duration less than 20 minutes were rejected.

The dual-frequency and linear combination of carrier phase measurements were used to correct the first-order effects of the ionosphere. The International Geomagnetic Reference Model was used to correct second-order ionospheric refraction following Kedar et al. (2003). Using the International Reference Ionosphere 2016 model (Bilitza et al., 2017), with an effective shell height of 600 km (Petrie et al., 2011), the slant Total Electron Content was extracted. Tables of monthly satellite-dependent P1-C1 differential code biases from the Astronomical Institute of the University of Bern were applied for the whole period.

Following the International Earth Rotation and Reference Systems Service (IERS) Conventions 2010 (Petit and Luzum, 2010), solid Earth tides, including ocean pole tides and frequency-dependent corrections were corrected to account for the motion of the Earth's crust. Deformations from ocean-tidal loading were modelled in the centre of mass of the total Earth system frame using the TPXO7.2 tide model and SPOTL software (Agnew, 1997; Egbert et al., 2009; Fu et al., 2012; Petit and Luzum, 2010).

Station positions were estimated in daily batches with receiver clock biases, real-valued phase ambiguities and tropospheric delays. Intervals of 24 hours were used to estimate station positions, while 5 minute intervals were used for clock bias and tropospheric delays. Zenith tropospheric delays were mapped to the elevation of each satellite using the Vienna Mapping Functions 1 (VMF1, Boehm et al., 2006), with a priori hydrostatic zenith delays extracted from the European Centre for Medium range Weather Forecast meteorological data (Tregoning and Herring, 2006). Assuming that the tropospheric delays are dominated by the un-modelled wet component, they were adjusted using a random walk process. Real-valued phase ambiguities were adjusted to integer values (Bertiger et al., 2010) for each station. The daily non-fiducial position time series were then transformed to ITRF2014 (Altamimi et al., 2016), using computed X-files with a 7-parameter transformation.

B.3 Supporting figures

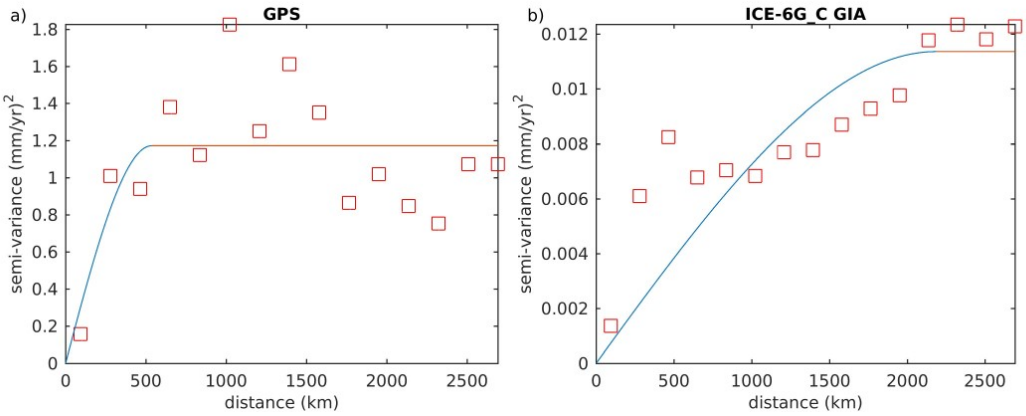

FIGURE B.1: Semi-variogram of a) vertical velocities at AuScope GPS sites and b) radial velocities from ICE-6G_C GIA model interpolated at AuScope GPS sites.

The empirical semi-variogram for the GPS sites is shown in Figure B.1a and for ICE-6G_C in Figure B.1b. These are computed using 15 bins representing spacing at 185 km and the semi-variogram was then modelled using an empirical spherical model. The number of bins were selected to mitigate high-frequency variation. Varying the bin sizes (spacing between sites) did not significantly alter the sill and range values. The range is the distance at which the semi-variance model 'flattens', and the sill represents the value at which the model reaches at the range, represented in Figure B.1 and Figure B.2 as a change of the line colour from blue to red.

The semi-variogram for GPS (Figure B.1a) shows increased power at shorter wavelengths as expected given the existence of site-specific noise. The range for GPS is 536 km, after which the sites are no longer considered to be spatially correlated. The range for the ICE6G_C GIA model (Figure B.1b) is 2185 km using a spherical fit to the variogram. There were negligible changes to the range for both GPS and GIA using alternative variogram functions. The nugget for both models is estimated and is small (non-zero). There appears to be a double sill for the GIA data, with the first sill at $\sim$500 km which is not resolved by the variogram functional model.

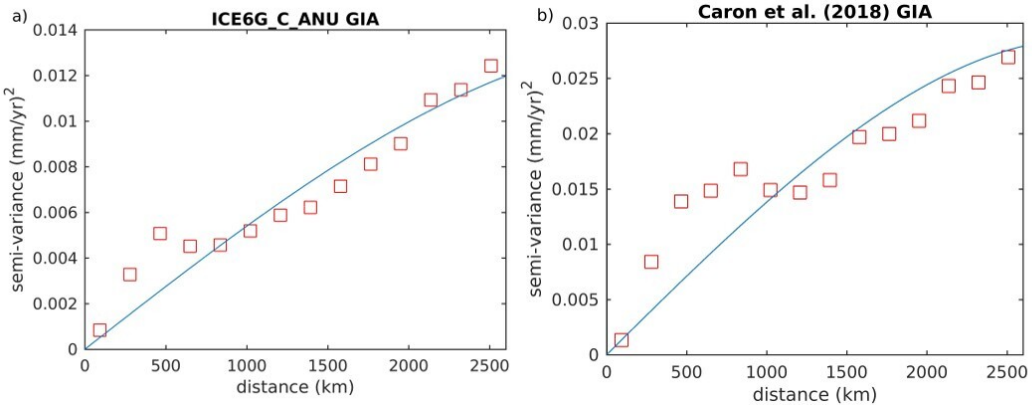

FIGURE B.2: Semi-variograms of alternative GIA models interpolated at AuScope GPS sites for a) ICE6GC_ANU and, b) Caron et al., (2018) GIA model.

The semivariogram for ICE6G_C_ANU and Caron et al. (2018) GIA models (Figure B.2) show a similar pattern where there appears to be an initial sill ∼500-1000 km and then reaches a secondary sill ∼2500 km. This suggests that the data is spatially correlated up until a point and then model error begins to influence data correlation.

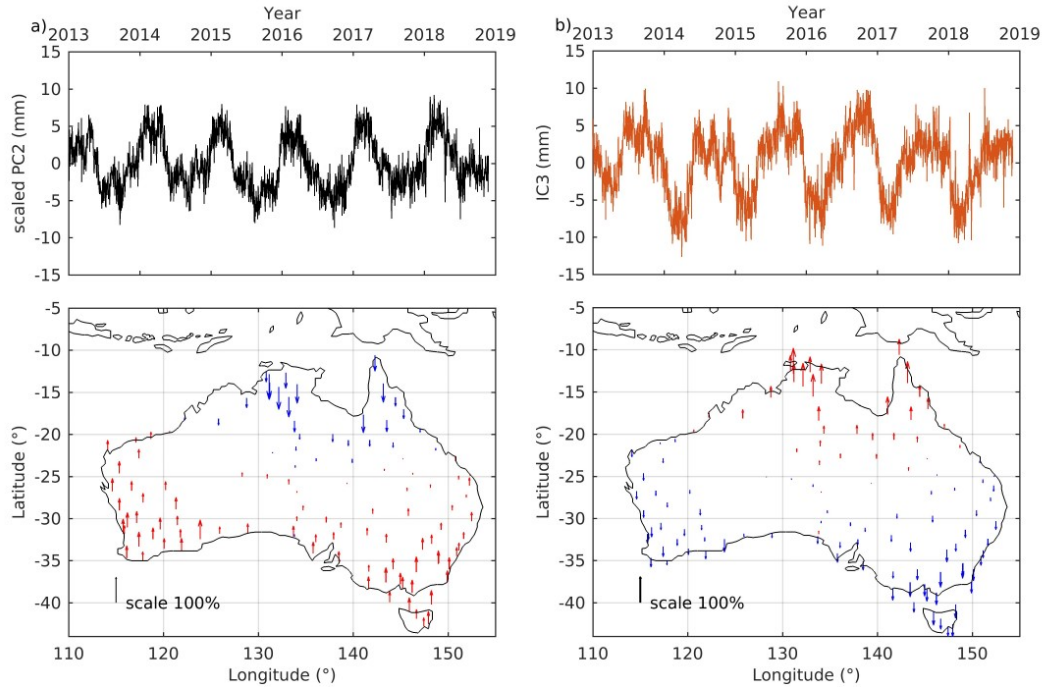

FIGURE B.3: Temporal and spatial response of the third modes from PCA and ICA, where the loading due to surface mass transport (atmosphere, land water storage, non-tidal ocean) at each site has been removed prior to analysis. Top is the scaled leading component time series and below is the normalised spatial eigenvector (not displacement direction). The up arrows represent a positive spatial response, and down arrows represent a negative spatial response.

Figure B.3 highlights the spatial pattern and temporal variability that can be associated with Inter-annual variability of the terrestrial water storage deformation signal, largely driven by the El-Niño Southern Oscillation (ENSO) and the Indian Ocean Dipole (Forootan et al., 2012; García-García et al., 2011).

B.4 Supporting tables

TABLE B.1: Sites used from the Australian AuScope network that have continuous time series from 2013.0-2019.0 and their approximate geographic coordinates. SF is scale factor from the multivariate regression analysis. *excluded due to noisy time series

Site	Latitude	Longitude	Height (m)	Up velocity (mm/yr)	PC1 SF	IC1 SF
ALBY	-35° 02′ 59"	117° 48′ 36"	34.121	-0.20 ± 0.34	0.66	0.71
ALIC	-24° 19′ 48"	133° 53′ 08"	602.315	-1.89 ± 0.55	0.86	0.77
ANDA	-31° 32′ 48"	137° 09′ 36"	103.721	0.00 ± 0.51	0.95	0.92
ARMC	-23° 02′ 36"	145° 14′ 44"	271.505	-1.54 ± 0.88	0.84	0.68
ARUB	-32° 11′ 27"	125° 55′ 28"	101.601	-0.53 ± 0.65	0.81	0.83
BALA	-33° 32′ 21"	123° 52′ 05"	125.073	-0.71 ± 0.66	0.76	0.86
BBOO	-33° 11′ 23"	136° 03′ 31"	292.122	-0.19 ± 0.42	0.91	0.92
BDVL	-26° 05′ 59"	139° 20′ 53"	66.088	-1.04 ± 0.38	0.87	0.75
BEEC	-37° 39′ 13"	146° 39′ 28"	445.391	-1.36 ± 0.40	0.93	0.77
BING	-33° 35′ 18"	151° 39′ 08"	487.280	-0.90 ± 0.63	0.78	0.53
BKNL	-32° 00′ 13"	141° 28′ 12"	309.366	-0.12 ± 0.56	0.93	0.84
BMAN	-32° 53′ 37"	138° 42′ 25"	618.132	-1.42 ± 0.72	0.94	0.85
BNDY	-25° 05′ 30"	152° 19′ 16"	81.375	-0.48 ± 0.72	0.78	0.56
BRO1	-19° 59′ 46"	122° 12′ 33"	45.598	-0.22 ± 0.82	0.76	0.68
BROC	-37° 58′ 07"	144° 12′ 14"	132.059	-1.19 ± 0.45	0.91	0.78
BULA	-23° 05′ 11"	139° 54′ 11"	201.199	-0.34 ± 0.60	0.87	0.73
BUR2	-42° 56′ 60"	145° 54′ 54"	2.139	-0.15 ± 0.32	0.81	0.73
BURA	-31° 28′ 28"	117° 10′ 29"	327.566	-0.06 ± 0.57	0.65	0.72
CEDU	-32° 07′ 60"	133° 48′ 35"	142.371	0.01 ± 0.62	0.90	0.79
CNBN	-32° 40′ 00"	149° 16′ 10"	682.128	0.31 ± 0.66	0.79	0.46
COEN	-14° 02′ 28"	143° 10′ 36"	250.755	-0.90 ± 0.65	0.84	0.45
COOB	-30° 57′ 55"	134° 43′ 21"	232.533	-0.01 ± 0.59	0.95	0.90
COOL	-27° 15′ 28"	145° 40′ 49"	335.166	-0.28 ± 0.61	0.83	0.65
DARW	-13° 09′ 23"	131° 07′ 58"	128.177	-0.98 ± 0.87	0.66	0.20
DODA	-14° 09′ 55"	131° 11′ 13"	87.113	0.49 ± 0.54	0.73	0.45
EDSV	-26° 37′ 27"	151° 07′ 11"	288.718	-1.98 ± 0.75	0.79	0.65
ESPA	-34° 07′ 32"	121° 53′ 40"	29.379	-0.20 ± 0.42	0.72	0.79
EXMT	-22° 02′ 22"	114° 06′ 48"	16.697	-0.42 ± 0.40	0.66	0.63
FLND	-41° 47′ 08"	148° 14′ 30"	6.604	-0.78 ± 0.25	0.81	0.78
FROY	-19° 52′ 27"	125° 48′ 02"	160.766	-0.40 ± 0.88	0.70	0.62
GABO	-38° 25′ 55"	149° 54′ 55"	18.461	-0.72 ± 0.33	0.80	0.68
GASC	-25° 22′ 03"	115° 20′ 19"	185.042	0.16 ± 0.46	0.49	0.46
GGTN	-19° 41′ 38"	143° 32′ 26"	366.602	-2.13 ± 0.74	0.82	0.63
HERN	-31° 40′ 24"	152° 29′ 13"	1241.537	-1.09 ± 0.85	0.79	0.68

HIL1	-32° 10′ 28"	115° 44′ 19"	-32.432	-2.53 ± 0.71	0.63	0.62
HNIS	-11° 24′ 35"	142° 17′ 46"	90.440	0.05 ± 0.51	0.79	0.39
HOB2	-43° 11′ 43"	147° 26′ 19"	43.239	-2.28 ± 0.42	0.71	0.51
HUGH	-21° 03′ 09"	144° 12′ 16"	526.539	0.72 ± 0.85	0.89	0.75
HYDN	-33° 33′ 02"	118° 53′ 31"	298.085	-0.46 ± 0.51	0.67	0.79
IHOE	-33° 08′ 09"	143° 29′ 31"	152.119	-0.06 ± 0.63	0.93	0.82
JAB2	-13° 20′ 24"	132° 53′ 40"	80.119	2.46 ± 1.10	0.79	0.14
JERV	-23° 08′ 22"	136° 06′ 02"	382.295	-0.36 ± 0.42	0.91	0.77
JLCK	-21° 19′ 51"	141° 44′ 21"	168.775	-0.20 ± 0.82	0.91	0.70
KALG	-31° 12′ 56"	121° 27′ 33"	339.514	0.21 ± 0.63	0.77	0.82
KARR	-21° 01′ 07"	117° 05′ 50"	110.470	1.04 ± 0.45	0.62	0.59
KAT1	-15° 37′ 26"	132° 09′ 12"	180.178	0.02 ± 0.67	0.78	0.40
KGIS	-40° 03′ 29"	143° 50′ 49"	9.367	-1.84 ± 0.32	0.86	0.74
KILK	-27° 54′ 57"	152° 15′ 07"	249.107	-0.58 ± 0.84	0.75	0.75
KUNU	-16° 19′ 23"	128° 45′ 46"	89.225	0.06 ± 0.67	0.82	0.68
LAMB	-27° 03′ 41"	134° 03′ 46"	309.035	-0.01 ± 0.45	0.92	0.87
LARR	-16° 25′ 37"	133° 12′ 46"	230.405	-0.32 ± 0.80	0.85	0.62
LIAW	-42° 05′ 52"	146° 40′ 23"	1049.591	-0.78 ± 0.42	0.78	0.57
LKYA	-13° 32′ 40"	130° 49′ 29"	69.925	0.07 ± 0.43	0.90	0.94
LONA	-29° 07′ 18"	121° 19′ 09"	358.423	-0.26 ± 0.50	0.78	0.80
LURA	-16° 25′ 21"	144° 27′ 25"	149.864	-0.35 ± 0.48	1.00	0.87
MAIN	-15° 57′ 14"	134° 05′ 34"	160.086	-0.07 ± 0.74	0.86	0.54
MCHL	-27° 38′ 28"	148° 08′ 42"	531.905	-0.37 ± 0.85	0.94	0.80
MEDO	-27° 14′ 33"	114° 36′ 34"	115.786	-0.07 ± 0.52	0.67	0.65
MNGO	-39° 13′ 13"	143° 39′ 06"	63.761	-0.30 ± 0.48	0.86	0.85
MOBS	-38° 10′ 14"	144° 58′ 31"	41.099	-1.40 ± 0.48	0.87	0.74
MRBA	-18° 58′ 55"	145° 19′ 26"	647.383	-0.15 ± 0.94	0.83	0.62
MRO1	-27° 18′ 12"	116° 38′ 15"	353.265	0.83 ± 0.44	0.59	0.60
MTCV	-26° 03′ 16"	133° 12′ 24"	544.991	-0.25 ± 0.37	0.91	0.86
MTDN	-23° 52′ 02"	131° 29′ 34"	668.516	-0.06 ± 0.56	0.82	0.75
MTEM	-38° 24′ 45"	143° 26′ 56"	515.234	0.55 ± 0.81	0.90	0.80
MTIS	-21° 18′ 35"	139° 29′ 11"	397.333	-0.75 ± 0.69	0.88	0.72
MTMA	-29° 53′ 05"	117° 50′ 35"	391.956	0.10 ± 0.45	0.69	0.73
MULG	-31° 43′ 05"	134° 03′ 31"	213.747	-1.29 ± 0.57	0.92	0.84
NBRK	-30° 19′ 22"	145° 48′ 51"	182.660	-0.85 ± 0.50	0.93	0.80
NCLF	-35° 17′ 30"	116° 07′ 24"	73.854	0.28 ± 0.34	0.69	0.71
NEBO	-22° 21′ 35"	148° 41′ 55"	342.745	-1.87 ± 0.65	0.80	0.57
NHIL	-37° 41′ 30"	141° 38′ 46"	142.270	0.47 ± 0.49	0.95	0.77
NMTN	-18° 19′ 42"	141° 04′ 09"	58.211	0.90 ± 1.02	0.88	0.54
NNOR	-32° 57′ 05"	116° 11′ 34"	232.783	-0.18 ± 0.71	0.72	0.69
NORS	-33° 44′ 24"	121° 47′ 14"	457.216	-0.07 ± 0.48	0.67	0.75
NSTA	-30° 57′ 16"	150° 26′ 39"	460.342	-0.46 ± 0.58	0.89	0.67

NTJN	-22° 32′ 34"	133° 58′ 12"	620.952	-0.86 ± 0.76	0.83	0.71
PARK	-33° 00′ 05"	148° 15′ 53"	399.866	1.32 ± 0.79	0.78	0.96
PERT	-32° 11′ 53"	115° 53′ 07"	18.569	-0.96 ± 0.59	0.64	0.56
PTHL	-21° 27′ 37"	118° 40′ 44"	38.201	2.38 ± 0.55	0.61	0.55
PTKL	-35° 31′ 28"	150° 54′ 49"	40.182	0.16 ± 0.56	0.83	0.55
PTLD	-39° 39′ 20"	141° 36′ 49"	1.093	-0.59 ± 0.27	0.87	0.83
PTSV	-36° 54′ 19"	138° 29′ 09"	53.429	-1.67 ± 0.41	0.93	0.92
RAVN	-34° 24′ 12"	120° 04′ 15"	205.236	-0.10 ± 0.42	0.71	0.77
RKLD	-20° 01′ 57"	137° 50′ 05"	273.072	-0.06 ± 0.73	0.88	0.72
RNSP	-19° 36′ 44"	133° 48′ 59"	346.978	-0.69 ± 0.84	0.85	0.76
RSBY	-24° 50′ 21"	150° 47′ 24"	55.831	0.66 ± 0.63	0.97	0.81
SA45	-33° 31′ 47"	137° 56′ 04"	201.340	0.07 ± 0.42	0.98	0.95
SPBY	-43° 27′ 13"	147° 55′ 51"	6.981	-0.79 ± 0.24	0.82	0.73
STHG*	-25° 38′ 59"	143° 17′ 07"	194.667	6.70 ± 1.18	0.90	0.95
STNY	-39° 37′ 29"	145° 12′ 50"	25.889	-0.29 ± 0.32	0.94	0.79
STR1	-36° 41′ 04"	149° 00′ 36"	798.627	-0.53 ± 0.54	0.84	0.58
SYDN	-34° 13′ 09"	151° 09′ 01"	87.603	-0.34 ± 0.52	0.82	0.64
TBOB	-30° 32′ 59"	142° 03′ 27"	191.898	0.33 ± 0.52	0.92	0.80
THEV	-33° 52′ 17"	133° 41′ 49"	1.451	-0.56 ± 0.42	0.94	1.00
TID1	-36° 36′ 03"	148° 58′ 48"	667.141	-0.43 ± 0.39	0.80	0.49
TMBO	-25° 13′ 42"	146° 17′ 03"	589.956	-1.81 ± 0.89	0.88	0.73
TOMP	-23° 09′ 13"	117° 24′ 01"	430.063	0.86 ± 0.46	0.72	0.70
TOOW	-28° 27′ 56"	151° 55′ 42"	684.005	-0.68 ± 0.99	0.74	0.41
TOW2	-20° 43′ 51"	147° 03′ 21"	83.802	-0.01 ± 0.60	0.81	0.56
TURO	-37° 57′ 53"	150° 07′ 20"	51.796	-1.28 ± 0.34	0.84	0.69
UCLA	-32° 19′ 14"	128° 52′ 59"	65.917	0.48 ± 0.49	0.87	0.92
WAGN	-34° 40′ 01"	117° 24′ 36"	291.679	-0.97 ± 0.55	0.64	0.67
WARA	-26° 57′ 46"	128° 17′ 46"	592.257	-0.36 ± 0.40	0.86	0.81
WILU	-27° 22′ 28"	120° 13′ 06"	490.709	-0.27 ± 0.45	0.68	0.72
WLAL	-20° 13′ 17"	120° 38′ 37"	23.566	1.99 ± 0.53	0.69	0.61
WMGA	-20° 03′ 60"	134° 21′ 16"	417.466	-1.16 ± 0.65	0.85	0.72
WWLG	-34° 17′ 48"	147° 19′ 18"	359.843	-1.34 ± 0.49	0.87	0.65
YAR2	-30° 57′ 12"	115° 20′ 49"	245.084	-1.27 ± 0.56	0.65	0.62
YEEL	-35° 51′ 21"	135° 47′ 04"	173.070	-0.06 ± 0.38	0.91	0.91
YELO	-32° 42′ 33"	119° 38′ 45"	350.926	-0.59 ± 0.53	0.71	0.81
YNKI	-39° 11′ 16"	146° 13′ 06"	36.530	-1.34 ± 0.42	0.84	0.78
YULA	-26° 46′ 08"	130° 56′ 30"	514.084	0.03 ± 0.54	0.87	0.81

TABLE B.2: Difference in median PLW noise parameters and median PLW trend of the full GPS time series (variable for each site) and truncated GPS time series (2013.0 – 2019.0)

	FULL SERIES	2013-2019	Δ
Trend (mm/yr)	-0.6 (0.4)	-0.3 (0.5)	0.3
PLW amplitude ($mm/yr^{-\kappa/4}$)	9.6 (0.2)	9.0 (0.2)	0.6
Spectral Index (κ)	-0.6 (0.1)	-0.6 (0.1)	0.0
Annual Amplitude (mm)	4.2 (0.5)	4.1 (0.5)	0.1

B.5 Copyright and License details

©2020 Geoscience Australia, Commonwealth of Australia

This is an open access article under the terms of the Creative Commons Attribution License, which permits use, distribution and reproduction in any medium, provided the original work is properly cited.

Appendix C

Supporting Information for Chapter 4

C.1 PYGR coseismic offsets (PT09)

Our coseismic estimates at Puysegur Point, New Zealand (PYGR) using two weeks of data either site of the earthquake event are -59.7 $\pm$ 23.7 mm, -323.8 $\pm$ 11.7 mm, and 6.4 $\pm$ 2.4 mm for north, east and up components respectively. The coseismic offsets for sites in the near-field may be influenced by postseismic deformation, however PYGR is included for completeness. The high uncertainty on the PYGR coseismic offsets is largely due to the immediate postseismic deformation. This site was very close to the hypocentre of the earthquake ($\sim$47 km), and so it is difficult to distinguish between afterslip and postseismic deformation, which can skew the coseismic offset estimation. Using one week either side of the event we calculated the coseismic offset at PYGR to be -52.5 $\pm$ 22.1 mm, -320.1 $\pm$ 9.7 mm, and 2.1 $\pm$ 4.0 mm for north, east and up components respectively. These differ from those of Mahesh et al. (2011) who estimate coseismic offsets at permanent GPS sites in New Zealand within the near- and far-field of the earthquake, but only consider three days of data either side of the event and do not provide uncertainty estimates. For the closest permanent GPS site, PYGR, Mahesh et al. (2011) estimate the coseismic offsets to be -30 mm, -301 mm and -200 mm for north, east and up components respectively. Our results show substantially smaller changes coseismic uplift suggesting that afterslip could be occurring.

When investigating the inversion of GPS and differential InSAR observations Beavan et al. (2010b) estimate the maximum horizontal slip displacement from PT09 to be approximately 1.7 m and demonstrate that the pre- and post-earthquake velocities are different up to 3 mm/yr at sites in New Zealand. Due to site availability, the displacement inversion for the total slip in Beavan et al. (2010b) only uses ten sparsely located continuous GPS sites that are supplemented with campaign observations. This is not an optimal solution, but unfortunately the availability of permanently operating sites at the time of the event does not allow for a more rigorous

inversion or comparison of results. We were able to obtain similar coseismic offsets at a New Zealand sites (PYGR) with those from Beavan et al. (2010b), meaning that our offsets observed at Australian sites can be considered realistic and significant.

C.2 Supporting File

This is an example of the modified earth.model used in VISCO1D (v3) with extra parameters defining the lower mantle.

```
67 4  6371.000     0.714
 3480.000 3481.000    5.000   44.000   22.000 1.000000E+03
 3481.000 3500.000    5.000   44.000   22.000 1.000000E+03
 3500.000 3600.000    5.000   44.000   22.000 1.000000E+03
 3600.000 3700.000    5.000   44.000   22.000 1.000000E+03
 3700.000 3800.000    5.000   44.000   22.000 1.000000E+03
 3800.000 3900.000    5.000   44.000   22.000 1.000000E+03
 3900.000 4000.000    5.000   44.000   22.000 1.000000E+03
 4000.000 4100.000    5.000   44.000   22.000 1.000000E+03
 4100.000 4200.000    5.000   44.000   22.000 1.000000E+03
 4200.000 4300.000    5.000   44.000   22.000 1.000000E+03
 4300.000 4400.000    5.000   44.000   22.000 1.000000E+03
 4400.000 4500.000    5.000   44.000   22.000 1.000000E+03
 4500.000 4600.000    5.000   44.000   22.000 1.000000E+03
 4600.000 4700.000    5.000   44.000   22.000 1.000000E+03
 4700.000 4800.000    5.000   44.000   22.000 1.000000E+03
 4800.000 4900.000    5.000   44.000   22.000 1.000000E+03
 4900.000 5000.000    5.000   44.000   22.000 1.000000E+03
 5000.000 5100.000    5.000   44.000   22.000 1.000000E+03
 5100.000 5200.000    5.000   44.000   22.000 1.000000E+03
 5200.000 5319.100    5.000   44.000   22.000 1.000000E+03
 5319.100 5353.700    5.000   44.000   22.000 1.000000E+03
 5353.700 5388.300    5.000   44.000   22.000 1.000000E+03
 5388.300 5422.900    5.000   44.000   22.000 1.000000E+03
 5422.900 5457.600    5.000   44.000   22.000 1.000000E+03
 5457.600 5492.200    5.000   44.000   22.000 1.000000E+03
 5492.200 5526.800    5.000   44.000   22.000 1.000000E+03
 5526.800 5561.500    5.000   44.000   22.000 1.000000E+03
 5561.500 5596.100    5.000   44.000   22.000 1.000000E+03
 5596.100 5630.700    5.000   44.000   22.000 1.000000E+03
 5630.700 5665.400    5.000   44.000   22.000 1.000000E+03
 5665.400 5701.000    5.000   44.000   22.000 1.000000E+03
 5701.000 5731.300    3.800    5.000    3.000    1.500 0.100000E+01 0.100000E+02
 5731.300 5771.000    3.800    5.000    3.000    1.500 0.100000E+01 0.100000E+02
```

```
5771.000 5793.800    3.800    5.000    3.000    1.500 0.100000E+01 0.100000E+02
5793.800 5825.000    3.800    5.000    3.000    1.500 0.100000E+01 0.100000E+02
5825.000 5856.300    3.800    5.000    3.000    1.500 0.100000E+01 0.100000E+02
5856.300 5887.500    3.800    5.000    3.000    1.500 0.100000E+01 0.100000E+02
5887.500 5918.700    3.800    5.000    3.000    1.500 0.100000E+01 0.100000E+02
5918.700 5950.000    3.800    5.000    3.000    1.500 0.100000E+01 0.100000E+02
5950.000 5975.600    3.800    5.000    3.000    1.500 0.100000E+01 0.100000E+02
5975.600 6001.200    3.800    5.000    3.000    1.500 0.100000E+01 0.100000E+02
6001.200 6026.900    3.800    5.000    3.000    1.500 0.100000E+01 0.100000E+02
6026.900 6052.500    3.800    5.000    3.000    1.500 0.100000E+01 0.100000E+02
6052.500 6078.100    3.800    5.000    3.000    1.500 0.100000E+01 0.100000E+02
6078.100 6103.800    3.800    5.000    3.000    1.500 0.100000E+01 0.100000E+02
6103.800 6129.400    3.800    5.000    3.000    1.500 0.100000E+01 0.100000E+02
6129.400 6155.000    3.800    5.000    3.000    1.500 0.100000E+01 0.100000E+02
6155.000 6180.600    3.800    5.000    3.000    1.500 0.100000E+01 0.100000E+02
6180.600 6206.300    3.800    5.000    3.000    1.500 0.100000E+01 0.100000E+02
6206.300 6231.900    3.800    5.000    3.000    1.500 0.100000E+01 0.100000E+02
6231.900 6257.500    3.800    5.000    3.000    1.500 0.100000E+01 0.100000E+02
6257.500 6283.100    3.800    5.000    3.000    1.500 0.100000E+01 0.100000E+02
6283.100 6308.800    3.800    5.000    3.000    1.500 0.100000E+01 0.100000E+02
6308.800 6321.000    3.800    5.000    3.000    1.500 0.100000E+01 0.100000E+02
6321.000 6334.400    3.800    5.000    3.000    1.500 0.100000E+01 0.100000E+02
6334.400 6338.000    3.800    5.000    3.000    1.500 0.100000E+01 0.100000E+02
6338.000 6341.000    3.800    5.000    3.000    1.500 0.100000E+01 0.100000E+02
6341.000 6346.000    3.300    5.000    3.000 0.100000E+12
6346.000 6351.000    3.300    5.000    3.000 0.100000E+12
6351.000 6357.000    3.300    5.000    3.000 0.100000E+12
6357.000 6359.000    3.300    5.000    3.000 0.100000E+12
6359.000 6361.000    3.300    5.000    3.000 0.100000E+12
6361.000 6363.000    3.300    5.000    3.000 0.100000E+12
6363.000 6365.000    3.300    5.000    3.000 0.100000E+12
6365.000 6367.000    3.300    5.000    3.000 0.100000E+12
6367.000 6369.000    3.300    5.000    3.000 0.100000E+12
6369.000 6371.000    3.300    5.000    3.000 0.100000E+12
```

C.3 Supporting figures

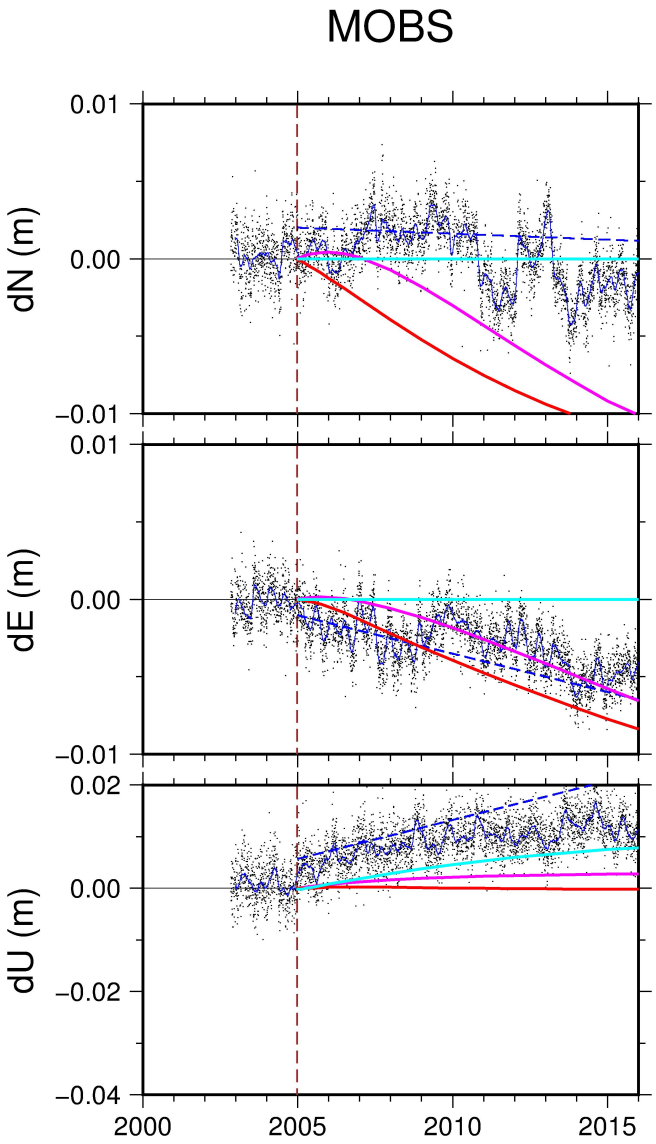

FIGURE C.1: GPS time series at Melbourne (MOBS) after removing a trend computed over the pre-earthquake period (2000.0–2004.9) for MI04. A 100-day running mean is shown in blue. Blue dashed line is the estimated linear velocity post-earthquake. Red is the best fitting viscoelastic model for the horizontal components, cyan is the best fitting visco model for the vertical component and magenta is the best fitting visco model for all components. The dashed vertical line indicates the date of the Macquarie Island earthquake (23 December 2004).

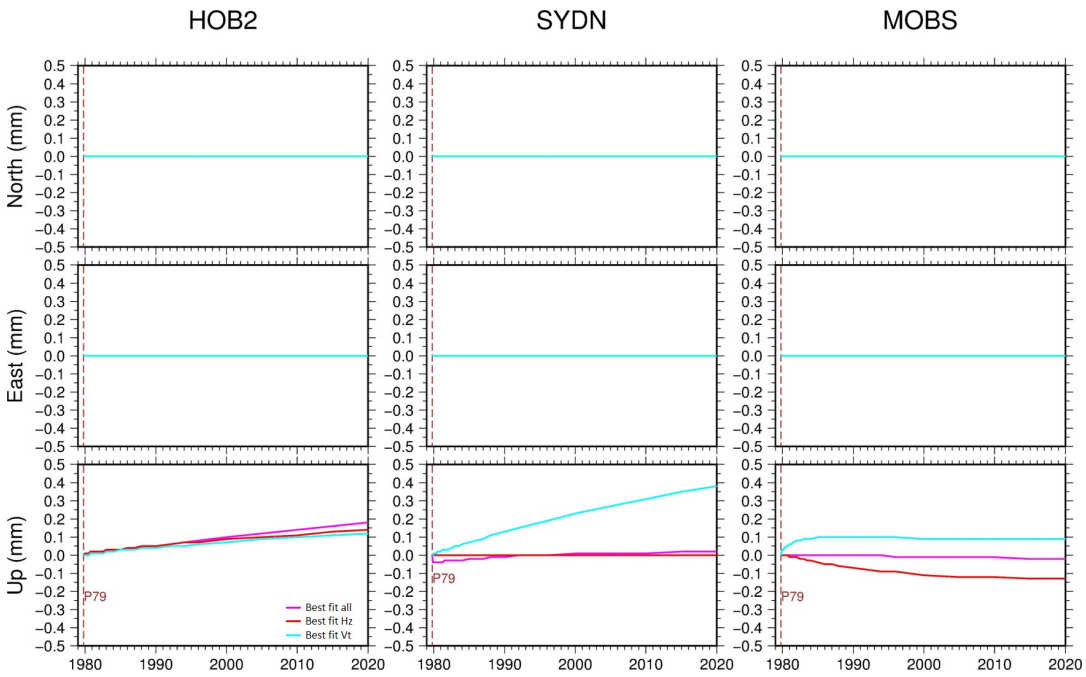

FIGURE C.2: Modelled postseismic deformation for the 1979 Puysegur Trench earthquake at sites Hobart (HOB2), Sydney (SYDN), and Melbourne (MOBS) using the Puy09 best fit models and fault geometry from Anderson et al. (1993).

C.4 Supporting tables

TABLE C.1: GPS sites used in this research with approximate coordinates

Site	Latitude	Longitude	Height (m)	EQ's	Time period
ALIC	-23° 40′ 12.25"	133° 53′ 7.71"	602.315	SU12	2007.4-2019.0
BRO1	-18° 00′ 14.41"	122° 12′ 32.76"	45.598	SU12	2010.5-2019.0
CEDU	-31° 52′ 0.03"	133° 48′ 35.34"	142.371	SU04, SU05, SU07, SU12, MI04	1997.7-2019.0
COCO	-12° 11′ 18.12"	96° 50′ 02.31"	-36.433	SU04, SU05, SU07, SU12	1996.0-2019.0
DARW	-12° 50′ 37.31"	131° 07′ 57.81"	128.177	SU04, SU05, SU07, SU12, MI04	1996.5-2019.0
HIL1	-31° 49′ 31.82"	115° 44′ 18.90"	-32.432		2005.5-2019.0
HOB2	-42° 48′ 16.99"	147° 26′ 19.23"	43.239	MI04, PT09, PT79	1996.0-2019.0
KARR	-20° 58′ 52.97"	117° 05′ 49.73"	110.470	SU04, SU05, SU07, SU12	1996.3-2019.0
MAC1	-54° 29′ 58.22"	158° 56′ 9.175"	-10.050	MI04, PT09, PT79	1996.0-2019.0
MOBS	-37° 49′ 45.83"	144° 58′ 31.41"	41.099	MI04, PT09, PT79	2002.8-2019.0
NNOR	-31° 02′ 55.30"	116° 11′ 33.70"	232.783	SU05, SU07, SU12	2002.5-2019.0
PERT	-31° 48′ 7.12"	115° 53′ 6.94"	18.569	SU04, SU05, SU07, SU12	1996.0-2019.0
STR1	-35° 18′ 55.97"	149° 00′ 36.12"	798.627	MI04, PT09	1998.4-2019.0
SYDN	-33° 46′ 51.18"	151° 09′ 1.24"	87.603	MI04, PT09	2004.3-2019.0
TID1	-35° 23′ 56.96"	148° 58′ 47.97"	667.141	MI04, PT09	1996.5-2019.0
TIDB	-35° 23′ 56.96"	148° 58′ 47.97"	667.141	MI04	1996.0-2019.0
TOW2	-19° 16′ 9.48"	147° 03′ 20.55"	83.802	SU04, SU05, SU07, SU12	1996.0-2019.0
XMIS	-10° 27′ 0.018"	105° 41′ 18.46"	261.133	SU07, SU12	2005.5-2019.0
YAR2	-29° 02′ 47.52"	115° 20′ 49.20"	245.084	SU04, SU05, SU07, SU12	1996.2-2019.0

TABLE C.2: Offsets calculated from the GPS time series at the time of equipment changes or coseismic earthquake displacement. Uncertainty is one-sigma.

Site	N (mm)	E (mm)	U (mm)	Time (decimal year)	Offset cause
ALIC	2.50 ± 0.72	0.37 ± 0.34	0.42 ± 0.61	2007.696	SU07
ALIC	2.69 ± 1.23	1.45 ± 0.52	-0.47 ± 0.89	2008.290	rcvr change
ALIC	1.96 ± 0.80	1.38 ± 0.65	-2.35 ± 0.98	2009.534	PT09
ALIC	4.18 ± 0.70	1.17 ± 0.45	5.33 ± 1.53	2011.551	ant change
ALIC	2.37 ± 0.57	0.81 ± 0.61	-0.74 ± 0.97	2012.276	SU12
ALIC	2.68 ± 1.07	1.10 ± 0.73	-0.04 ± 1.32	2016.093	rcvr change
BRO1	2.74 ± 1.54	0.97 ± 0.74	-1.04 ± 1.37	2012.276	SU12
CEDU	3.69 ± 0.26	3.52 ± 1.30	0.45 ± 1.44	2000.358	rcvr change

CEDU	1.45 ± 0.79	1.75 ± 0.93	-3.49 ± 2.42	2004.975	MI04
CEDU	1.02 ± 0.74	1.33 ± 0.41	-5.97 ± 2.37	2004.984	SU04
CEDU	2.59 ± 0.64	-1.23 ± 0.68	-2.90 ± 1.14	2005.236	SU05
CEDU	4.32 ± 0.75	3.32 ± 0.54	-5.04 ± 1.96	2005.416	rcvr change
CEDU	0.80 ± 1.79	0.76 ± 0.83	-2.82 ± 1.99	2006.156	both rcvr and antenna changed
CEDU	3.80 ± 1.77	0.06 ± 1.28	8.54 ± 1.60	2006.537	both rcvr and antenna changed
CEDU	0.42 ± 1.85	2.36 ± 0.78	-0.99 ± 1.45	2007.312	rcvr change
CEDU	3.18 ± 0.71	0.88 ± 0.47	0.36 ± 0.65	2007.696	SU07
CEDU	2.01 ± 0.48	1.22 ± 0.63	-3.46 ± 1.53	2009.534	PT09
CEDU	1.23 ± 0.66	0.38 ± 0.69	2.44 ± 1.27	2011.375	rcvr change
CEDU	2.24 ± 0.69	0.56 ± 0.52	0.60 ± 1.01	2012.276	SU12
CEDU	1.97 ± 0.40	0.70 ± 0.75	-9.70 ± 1.06	2016.577	rcvr change, radome removed
COCO	3.61 ± 2.26	1.25 ± 3.39	3.73 ± 3.82	1999.945	rcvr change
COCO	-3.12 ± 4.34	33.29 ± 1.39	4.92 ± 1.64	2000.437	unknown
COCO	-0.69 ± 5.48	3.02 ± 2.93	1.10 ± 3.45	2001.455	rcvr change
COCO	2.48 ± 2.05	1.64 ± 1.89	3.35 ± 2.79	2001.592	rcvr change
COCO	1.88 ± 2.11	2.17 ± 2.04	-1.07 ± 2.14	2004.478	rcvr change, radome removed
COCO	3.75 ± 2.79	1.82 ± 1.03	-2.77 ± 1.79	2004.975	MI04
COCO	5.33 ± 3.67	1.47 ± 1.28	0.70 ± 2.45	2005.238	SU05
COCO	10.46 ± 1.52	5.40 ± 0.79	1.53 ± 1.84	2007.696	SU07
COCO	2.32 ± 1.30	2.21 ± 2.61	-3.99 ± 1.55	2009.534	PT09
COCO	2.96 ± 3.73	1.56 ± 1.84	0.07 ± 2.46	2011.811	rcvr change
COCO	18.93 ± 3.92	-4.19 ± 0.77	-0.85 ± 3.05	2012.279	SU12
COCO	1.40 ± 1.24	2.41 ± 0.66	0.52 ± 2.09	2015.452	rcvr change
COCO	3.40 ± 3.00	-0.17 ± 2.27	-0.46 ± 3.15	2016.167	SU16
DARW	2.61 ± 2.40	-0.52 ± 2.97	-8.43 ± 3.45	1999.899	rcvr change, radome removed
DARW	3.84 ± 4.20	-0.13 ± 4.45	3.23 ± 4.09	2003.211	rcvr change
DARW	-3.36 ± 3.96	3.20 ± 2.06	2.05 ± 2.79	2003.258	ant change
DARW	1.20 ± 0.71	0.72 ± 0.35	5.43 ± 4.25	2004.538	rcvr change
DARW	3.14 ± 3.19	-0.42 ± 1.58	-0.70 ± 2.77	2004.975	MI04
DARW	3.04 ± 3.95	0.70 ± 1.76	-3.43 ± 3.14	2004.984	SU04
DARW	1.68 ± 1.08	-1.12 ± 1.26	0.26 ± 2.30	2005.236	SU05
DARW	3.52 ± 0.50	0.26 ± 0.51	2.45 ± 1.83	2007.696	SU07
DARW	3.01 ± 0.63	1.40 ± 0.76	3.28 ± 1.47	2008.363	rcvr change
DARW	2.54 ± 1.07	2.10 ± 0.45	1.83 ± 1.55	2009.534	PT09
DARW	-2.52 ± 3.47	-0.34 ± 1.24	0.18 ± 2.53	2012.276	SU12
DARW	2.00 ± 1.76	0.04 ± 0.91	3.13 ± 3.21	2016.801	rcvr change
DARW	12.49 ± 0.45	6.80 ± 0.54	1.09 ± 0.90	2017.507	ant change
HIL1	6.28 ± 9.88	0.49 ± 1.29	6.23 ± 4.73	2004.858	ant change
HIL1	3.57 ± 1.95	2.57 ± 3.31	-1.29 ± 2.32	2004.975	MI04
HIL1	2.42 ± 1.78	2.41 ± 2.15	-0.24 ± 2.38	2004.984	SU04
HIL1	3.90 ± 1.34	2.43 ± 1.42	-1.94 ± 2.65	2005.236	SU05

HIL1	4.01 ± 2.31	1.33 ± 0.86	-1.97 ± 1.73	2005.882	rcvr change
HIL1	2.93 ± 0.78	1.51 ± 1.25	-1.05 ± 1.20	2006.800	ant change
HIL1	4.22 ± 0.66	2.25 ± 0.95	3.02 ± 1.55	2007.696	SU07
HIL1	1.97 ± 0.88	0.84 ± 0.90	0.98 ± 1.60	2009.534	PT09
HIL1	3.26 ± 0.53	1.08 ± 0.95	2.07 ± 0.92	2012.276	SU12
HIL1	1.49 ± 0.65	2.95 ± 0.80	1.29 ± 0.95	2014.926	rcvr change
HIL1	2.44 ± 1.16	3.86 ± 0.98	-3.36 ± 1.08	2017.874	rcvr change
HOB2	1.68 ± 1.06	-1.82 ± 2.89	8.32 ± 2.30	1999.910	rcvr change
HOB2	-1.82 ± 1.79	-1.84 ± 2.73	5.54 ± 2.39	2000.566	rcvr change
HOB2	1.05 ± 2.07	-0.21 ± 2.99	4.18 ± 2.21	2002.236	rcvr change
HOB2	2.75 ± 1.78	1.45 ± 1.96	-2.48 ± 2.15	2002.249	rcvr change
HOB2	0.47 ± 1.30	6.07 ± 2.22	-1.07 ± 2.02	2004.975	MI04
HOB2	-0.27 ± 1.57	5.38 ± 2.69	0.28 ± 1.99	2004.984	SU04
HOB2	2.80 ± 1.09	-0.47 ± 2.31	-0.37 ± 1.24	2005.236	SU05
HOB2	4.66 ± 1.93	1.67 ± 1.19	-2.07 ± 3.37	2005.753	rcvr change
HOB2	2.56 ± 1.35	0.57 ± 1.38	1.28 ± 1.65	2007.696	SU07
HOB2	1.88 ± 0.99	0.09 ± 1.06	0.25 ± 1.85	2008.937	rcvr change
HOB2	0.72 ± 1.72	1.11 ± 1.71	-2.86 ± 2.23	2009.534	PT09
HOB2	0.80 ± 0.74	0.42 ± 1.57	2.16 ± 1.04	2012.276	SU12
HOB2	1.30 ± 1.33	2.55 ± 1.92	-1.72 ± 2.61	2016.888	rcvr change
KARR	1.04 ± 0.97	1.89 ± 1.05	-4.78 ± 1.56	1999.501	rcvr change
KARR	1.52 ± 0.91	1.89 ± 2.06	3.19 ± 3.44	1999.948	rcvr change
KARR	4.29 ± 0.84	-0.17 ± 1.35	-5.54 ± 1.30	2000.448	rcvr change
KARR	5.16 ± 2.52	-0.31 ± 0.45	-2.08 ± 1.37	2001.660	rcvr change
KARR	3.18 ± 1.29	1.22 ± 1.01	-3.42 ± 1.40	2001.732	rcvr change
KARR	4.33 ± 0.73	0.84 ± 1.11	0.15 ± 2.92	2001.797	rcvr change
KARR	1.19 ± 0.79	1.49 ± 0.70	4.06 ± 0.96	2003.422	rcvr change
KARR	1.73 ± 1.92	1.33 ± 0.79	1.73 ± 2.12	2004.975	MI04
KARR	1.35 ± 2.05	0.67 ± 0.76	1.16 ± 2.44	2004.984	SU04
KARR	4.05 ± 1.47	-0.22 ± 0.32	-2.07 ± 1.50	2005.236	SU05
KARR	3.72 ± 0.88	1.94 ± 1.03	0.84 ± 0.81	2007.696	SU07
KARR	1.92 ± 0.64	0.97 ± 0.73	1.71 ± 1.22	2009.534	PT09
KARR	2.79 ± 0.88	0.68 ± 0.36	2.88 ± 1.00	2010.381	both rcvr and antenna changed
KARR	3.54 ± 0.98	0.26 ± 0.83	2.28 ± 1.34	2012.276	SU12
KARR	3.23 ± 6.93	0.07 ± 1.50	3.54 ± 4.61	2013.696	both rcvr and antenna changed
MAC1	2.37 ± 0.64	1.42 ± 1.23	-4.59 ± 1.58	1999.649	rcvr change
MAC1	2.92 ± 1.32	-2.02 ± 1.59	2.87 ± 1.33	2001.008	rcvr change
MAC1	0.67 ± 0.60	-0.81 ± 2.20	-1.45 ± 1.65	2005.236	SU05
MAC1	0.36 ± 0.43	0.98 ± 0.88	1.75 ± 1.22	2005.304	rcvr change
MAC1	1.69 ± 0.60	-2.15 ± 1.26	1.68 ± 0.89	2007.696	SU07
MAC1	0.88 ± 1.01	-1.13 ± 1.73	-3.31 ± 1.32	2009.534	PT09
MAC1	-0.42 ± 0.81	-0.63 ± 3.81	0.10 ± 1.35	2011.310	rcvr change
MAC1	-0.60 ± 0.63	-0.10 ± 1.55	-0.37 ± 1.00	2012.276	SU12
MAC1	2.45 ± 0.56	1.27 ± 1.24	-1.17 ± 1.55	2016.913	both rcvr and antenna changed

MOBS	1.81 ± 1.89	4.65 ± 1.62	-3.62 ± 1.72	2004.975	MI04
MOBS	0.68 ± 1.40	3.29 ± 1.90	-1.32 ± 1.76	2004.984	SU04
MOBS	2.70 ± 0.49	-1.51 ± 0.59	-0.44 ± 1.15	2005.236	SU05
MOBS	2.83 ± 1.20	2.08 ± 1.22	0.47 ± 1.45	2006.063	rcvr change
MOBS	2.07 ± 0.51	-0.74 ± 0.86	-3.31 ± 1.02	2007.468	rcvr change
MOBS	3.94 ± 1.04	0.36 ± 0.51	-1.21 ± 1.13	2007.696	SU07
MOBS	2.52 ± 0.60	3.21 ± 0.63	-1.55 ± 0.88	2008.877	rcvr change
MOBS	0.97 ± 0.71	0.91 ± 0.77	1.55 ± 1.34	2009.534	PT09
MOBS	3.15 ± 0.33	0.11 ± 0.55	2.12 ± 1.26	2009.559	rvcr tracking issue
MOBS	2.25 ± 0.60	0.76 ± 0.40	1.58 ± 1.17	2012.276	SU12
MOBS	1.60 ± 0.45	-0.41 ± 0.72	-0.22 ± 1.22	2016.055	rcvr change
NNOR	2.96 ± 1.09	1.42 ± 1.23	-0.87 ± 2.19	2004.975	MI04
NNOR	1.71 ± 1.51	1.25 ± 0.65	-3.24 ± 2.20	2004.984	SU04
NNOR	3.36 ± 0.99	0.87 ± 0.81	-3.56 ± 1.45	2005.236	SU05
NNOR	3.49 ± 0.74	1.37 ± 1.29	-1.04 ± 1.32	2007.696	SU07
NNOR	1.40 ± 0.67	1.18 ± 0.85	-2.76 ± 2.11	2009.534	PT09
NNOR	3.31 ± 0.61	0.62 ± 0.63	2.48 ± 2.15	2012.276	SU12
PERT	1.14 ± 1.21	2.40 ± 0.68	-2.96 ± 2.08	2004.975	MI04
PERT	1.34 ± 1.07	2.00 ± 0.87	-3.66 ± 1.94	2004.984	SU04
PERT	3.54 ± 0.99	0.81 ± 0.44	-3.00 ± 0.98	2005.236	SU05
PERT	3.83 ± 0.97	1.99 ± 1.23	0.58 ± 1.70	2007.696	SU07
PERT	3.67 ± 0.83	1.64 ± 0.16	-7.42 ± 2.52	2008.022	rcvr change
PERT	-2.26 ± 1.39	4.58 ± 2.90	6.96 ± 2.39	2008.852	unknown
PERT	1.49 ± 0.76	0.57 ± 1.97	-0.17 ± 1.18	2009.534	PT09
PERT	2.86 ± 1.02	1.68 ± 3.79	-2.14 ± 3.13	2009.871	unknown
STR1	5.33 ± 2.23	-0.63 ± 3.77	14.49 ± 5.49	1999.049	radome removed
STR1	1.04 ± 1.00	-0.46 ± 1.60	1.51 ± 2.23	1999.882	ant change
STR1	4.60 ± 2.19	-1.38 ± 2.57	-0.87 ± 3.05	2000.145	rcvr change
STR1	4.29 ± 1.73	2.46 ± 2.05	1.05 ± 1.85	2000.656	rcvr change
STR1	4.23 ± 1.21	1.42 ± 0.99	-2.07 ± 2.61	2004.803	rcvr change
STR1	1.55 ± 0.90	3.82 ± 1.74	-0.63 ± 1.76	2004.975	MI04
STR1	1.16 ± 0.82	3.53 ± 1.56	-1.72 ± 1.92	2004.984	SU04
STR1	2.23 ± 0.42	-0.53 ± 0.94	0.02 ± 1.66	2005.236	SU05
STR1	1.53 ± 0.39	1.08 ± 0.80	1.27 ± 1.78	2006.326	rcvr change
STR1	2.86 ± 0.79	0.17 ± 0.70	-0.74 ± 1.47	2007.696	SU07
STR1	1.88 ± 0.70	2.51 ± 1.44	-0.67 ± 1.41	2008.803	rcvr change
STR1	2.09 ± 0.62	1.61 ± 2.70	2.84 ± 2.21	2009.534	PT09
STR1	1.92 ± 0.58	0.74 ± 0.75	0.27 ± 1.24	2012.276	SU12
STR1	2.33 ± 0.51	0.73 ± 0.64	-2.13 ± 1.66	2016.702	rcvr change
SYDN	1.33 ± 1.09	2.25 ± 0.74	-0.92 ± 2.89	2004.975	MI04
SYDN	1.13 ± 0.79	2.22 ± 0.65	-0.73 ± 2.80	2004.984	SU04
SYDN	2.29 ± 0.92	-1.92 ± 1.68	-5.81 ± 2.26	2005.236	SU05
SYDN	2.85 ± 0.80	0.56 ± 0.75	-2.77 ± 2.33	2007.696	SU07
SYDN	0.95 ± 1.74	1.98 ± 2.62	-1.61 ± 2.42	2009.534	PT09
SYDN	0.97 ± 0.84	0.68 ± 0.50	-1.74 ± 1.52	2012.276	SU12
TID1	1.97 ± 1.02	1.17 ± 1.96	0.34 ± 2.35	2004.934	ant change
TID1	0.70 ± 0.77	2.63 ± 2.55	-0.05 ± 2.27	2004.975	MI04

TID1	0.78 ± 0.70	3.19 ± 1.95	0.89 ± 2.03	2004.984	SU04
TID1	2.57 ± 0.82	-1.92 ± 0.62	-3.17 ± 1.52	2005.236	SU05
TID1	2.93 ± 0.96	1.57 ± 1.75	0.38 ± 1.31	2007.696	SU07
TID1	1.43 ± 0.67	2.39 ± 1.22	1.78 ± 1.56	2009.323	rcvr change
TID1	2.82 ± 1.00	3.78 ± 4.85	3.21 ± 2.29	2009.534	PT09
TID1	1.54 ± 0.66	0.02 ± 1.87	-1.96 ± 1.59	2012.276	SU12
TID1	1.95 ± 1.38	0.63 ± 1.83	-1.30 ± 2.14	2016.227	radome removed
TID1	4.01 ± 1.17	2.45 ± 2.62	2.50 ± 1.27	2016.590	ant change
TID1	1.91 ± 0.77	0.09 ± 2.13	-0.99 ± 1.77	2017.337	rcvr change
TIDB	6.81 ± 4.68	4.00 ± 3.12	-10.13 ± 5.37	1996.484	ant change
TIDB	2.33 ± 1.01	2.63 ± 3.70	-11.06 ± 2.97	1999.466	rcvr change
TIDB	2.35 ± 0.82	0.67 ± 2.41	-0.51 ± 2.06	2004.934	ant change
TIDB	0.62 ± 0.55	3.45 ± 3.91	0.16 ± 2.71	2004.975	MI04
TIDB	0.54 ± 0.58	3.51 ± 3.73	-0.55 ± 2.68	2004.984	SU04
TIDB	3.28 ± 0.60	-2.03 ± 0.85	0.58 ± 1.75	2005.236	SU05
TIDB	3.54 ± 1.32	1.61 ± 1.93	-0.04 ± 1.50	2007.696	SU07
TIDB	3.24 ± 0.93	4.01 ± 5.20	4.04 ± 2.23	2009.534	PT09
TIDB	-0.43 ± 1.32	-0.93 ± 0.42	1.42 ± 2.01	2010.504	rcvr change
TIDB	1.10 ± 0.79	0.26 ± 2.08	-2.98 ± 1.76	2012.276	SU12
TIDB	3.72 ± 1.21	1.94 ± 2.92	2.49 ± 1.29	2016.590	ant change
TOW2	0.51 ± 1.96	-1.07 ± 1.84	-1.11 ± 2.98	1999.904	rcvr change
TOW2	-0.36 ± 1.59	0.66 ± 0.67	5.93 ± 1.63	2002.748	rcvr change
TOW2	2.11 ± 2.02	3.22 ± 2.16	0.00 ± 2.08	2004.975	MI04
TOW2	3.01 ± 2.06	2.59 ± 2.10	0.54 ± 1.89	2004.984	SU04
TOW2	1.37 ± 4.32	-0.89 ± 1.43	-0.92 ± 2.65	2005.236	SU05
TOW2	1.18 ± 2.13	0.85 ± 0.96	4.12 ± 3.49	2006.121	rcvr change
TOW2	2.85 ± 0.54	-0.86 ± 0.65	0.44 ± 1.33	2007.696	SU07
TOW2	2.94 ± 1.07	0.46 ± 1.22	1.67 ± 1.82	2008.743	rcvr change
TOW2	1.94 ± 1.17	0.83 ± 0.51	2.41 ± 2.03	2009.534	PT09
TOW2	5.61 ± 1.04	0.03 ± 1.72	-11.16 ± 1.62	2011.729	ant change
TOW2	2.35 ± 0.82	0.76 ± 1.05	-2.71 ± 1.35	2012.276	SU12
TOW2	1.61 ± 0.85	0.19 ± 1.06	0.29 ± 1.50	2015.644	rcvr change
XMIS	4.23 ± 1.49	3.15 ± 6.50	2.06 ± 1.79	2006.540	EQ
XMIS	2.51 ± 1.79	3.72 ± 3.45	-0.13 ± 1.70	2007.696	SU07
XMIS	1.98 ± 5.49	0.20 ± 5.76	1.85 ± 2.38	2009.534	PT09
XMIS	6.64 ± 4.32	-4.40 ± 3.71	1.40 ± 2.94	2012.279	antenna cable changed
XMIS	2.73 ± 1.76	0.82 ± 3.64	1.21 ± 2.05	2014.482	both rcvr and antenna changed
YAR2	-3.81 ± 1.07	2.75 ± 1.07	-5.62 ± 3.04	1997.633	ant change
YAR2	5.87 ± 0.96	0.48 ± 0.81	4.33 ± 1.72	2002.370	ant change
YAR2	2.20 ± 0.92	2.51 ± 1.07	-1.98 ± 2.07	2004.975	MI04
YAR2	1.39 ± 1.02	2.25 ± 0.60	-0.24 ± 2.11	2004.984	SU04
YAR2	3.04 ± 1.78	0.99 ± 1.07	-5.63 ± 2.63	2005.236	SU05
YAR2	2.00 ± 0.81	1.87 ± 0.89	-0.13 ± 1.48	2005.584	rcvr change
YAR2	3.45 ± 0.67	1.77 ± 1.42	0.26 ± 0.99	2007.696	SU07
YAR2	2.92 ± 0.74	2.29 ± 1.62	-4.09 ± 2.50	2008.352	rcvr change

YAR2	1.27 ± 0.72	0.82 ± 0.92	0.74 ± 1.16	2009.534	PT09
YAR2	4.53 ± 1.14	1.34 ± 1.65	1.85 ± 1.60	2012.276	SU12
YAR2	2.26 ± 1.47	4.27 ± 1.99	-2.83 ± 1.58	2012.391	radome removed
YAR2	1.55 ± 0.67	1.12 ± 0.65	-0.01 ± 1.13	2012.686	radome replaced
YAR2	3.12 ± 0.74	3.46 ± 0.64	-3.32 ± 1.52	2013.466	radome removed

TABLE C.3: GPS site velocities calculated before and after the Macquarie Island 2004 earthquake. Uncertainty is one-sigma.

Site	Distance from MI04 eq (km)	Pre EQ trend N (mm/yr) [2000.0-2004.9]	Post EQ trend N (mm/yr) [2004.9-2011.0]	ΔN trend (mm/yr)	Pre EQ trend E (mm/yr) [2000.0-2004.9]	Post EQ trend E (mm/yr) [2004.9-2011.0]	ΔE trend (mm/yr)	Pre EQ trend U (mm/yr) [2000.0-2004.9]	Post EQ trend U (mm/yr) [2004.9-2011.0]	ΔU trend (mm/yr)
HOB2	1291	55.95 ± 0.22	55.40 ± 0.11	-0.55	13.78 ± 0.13	14.21 ± 0.12	0.43	0.21 ± 0.47	-0.78 ± 0.19	-0.99
MOBS	1830	57.52 ± 0.31	57.45 ± 0.21	-0.07	19.51 ± 0.29	19.32 ± 0.18	-0.19	-2.44 ± 0.47	-1.12 ± 0.30	1.32
STR1	1880	55.95 ± 0.36	55.63 ± 0.12	-0.32	18.68 ± 0.26	18.21 ± 0.18	-0.47	1.97 ± 0.50	-0.68 ± 0.40	-2.66
TID1	1873	55.24 ± 0.22	55.66 ± 0.10	0.42	18.10 ± 0.14	18.02 ± 0.13	-0.08	1.24 ± 0.44	-0.92 ± 0.46	-2.16

TABLE C.4: GPS site velocities calculated before and after the Sumatra 2004 earthquake. Uncertainty is one-sigma

Site	Distance from SU04 eq (km)	Pre EQ trend N (mm/yr) [2000.0-2004.9]	Post EQ trend N (mm/yr) [2004.9-2019.0]	Pre EQ trend E (mm/yr) [2000.0-2004.9]	Post EQ trend E (mm/yr) [2004.9-2019.0]	Pre EQ trend U (mm/yr) [2000.0-2004.9]	Post EQ trend U (mm/yr) [2004.9-2019.0]
COCO	1709	50.15 ± 0.36	53.60 ± 0.58	47.33 ± 0.30	43.97 ± 0.22	2.20 ± 0.64	-2.08 ± 0.33
KARR	3492	58.28 ± 0.26	58.66 ± 0.08	39.08 ± 0.18	38.87 ± 0.08	1.76 ± 0.61	-1.07 ± 0.26
YAR2	4061	57.36 ± 0.29	57.90 ± 0.10	38.95 ± 0.21	38.81 ± 0.10	1.55 ± 0.70	-0.99 ± 0.26
DARW	4196	59.74 ± 0.48	59.90 ± 0.19	36.15 ± 0.49	35.91 ± 0.16	-3.95 ± 1.59	-1.78 ± 0.49
HIL1	4325	56.39 ± 0.50	57.25 ± 0.13	41.19 ± 0.65	38.56 ± 0.16	-9.00 ± 1.53	-3.63 ± 0.37
PERT	4330	57.98 ± 0.34	58.00 ± 0.12	39.10 ± 0.32	38.11 ± 0.12	-5.08 ± 0.68	-2.49 ± 0.36
CEDU*	5402	59.08 ± 0.21	59.46 ± 0.13	28.98 ± 0.18	28.97 ± 0.13	0.29 ± 0.64	-0.31 ± 0.43
TOW2	5887	55.35 ± 0.20	57.09 ± 0.14	28.68 ± 0.20	29.46 ± 0.13	0.66 ± 0.50	-1.16 ± 0.37
STR1*	6636	55.96 ± 0.35	55.59 ± 0.11	18.51 ± 0.25	18.19 ± 0.11	1.20 ± 0.44	-1.08 ± 0.29
TID1*	6637	55.23 ± 0.22	55.53 ± 0.13	18.04 ± 0.13	18.09 ± 0.14	1.07 ± 0.36	-1.33 ± 0.36
HOB2*	6869	55.93 ± 0.22	55.64 ± 0.10	13.75 ± 0.14	14.00 ± 0.11	-1.09 ± 0.52	-1.85 ± 0.22

* these sites may be influenced by MI04

Appendix D

List of publications, research output and public engagement

D.1 Peer-reviewed journal papers

Year	Citation
2017	Riddell, A. R., King, M. A., Watson, C. S., Sun, Y., Riva, R. E. M., & Rietbroek, R. 2017. *Uncertainty in geocenter estimates in the context of ITRF2014*. Journal of Geophysical Research: Solid Earth, 122, pp. 4020-4032, doi: 10.1002/2016JB013698
2020	Riddell, A.R., King, M. A., & Watson, C. S. 2020. *Present-day vertical land motion of Australia from GPS observations and geophysical models*. Journal of Geophysical Research: Solid Earth, 125, e2019JB018034, doi: 10.1029/2019jb018034
2020	Riddell, A. R., King, M. A., & Watson, C. S. 2020. *Ongoing postseismic vertical deformation of the Australian continent from far-field earthquakes*. Submitted to Geophysical Journal International.

D.2 Oral presentations

Year	Event
2016	25 August. Tasmanian Surveying and Spatial Conference (Launceston, Australia). *Up and Down: Dealing with a disruptive Earth*.
2016	16 December. American Geophysical Union Fall Meeting (San Francisco, USA). *Uncertainty in ITRF2014 origin residuals*.
2017	25 April. European Geosciences Union (Vienna, Austria). *Temporal variability and coloured noise of SLR translations with respect to the ITRF2014 origin*.
2017	9 May. Bonn University (Bonn, Germany). *Geodesy at Geoscience Australia & Uncertainty in the Geocentre*.
2017	13 June. School of Land and Food conference (Hobart, Australia). *Motion of the Earth's centre of mass*.
2017	29 June. Australian Geodesy Workshop (Canberra, Australia). *Temporal variability and coloured noise of SLR translations wrt ITRF2014*.
2017	14 September. GeoRabble (Hobart, Australia). *Measuring Earth's 'wiggle': A journey to the centre*.
2017	16 November. Geological Society of Australia Earth Science Student Symposium (Hobart, Australia). *Surface deformation of Australia from nearby earthquakes*.
2018	28 March. FameLab (Melbourne, Australia), *Measuring Earth's wiggle*.
2020	25 June. Australian National University Research School of Earth Sciences Seminar (Canberra, Australia). *Estimating present-day Australian vertical deformation using space geodetic techniques*.
2020	15 July. Geoscience Australia Distinguished Lecture Series (Canberra, Australia). *What goes up must come down... Why is Australia sinking?*.

D.3 Poster presentations

Year	Event
2016	Riddell, A. R., *Vertical Motion of the Australia Plate*, Graduate Research Conference, 2 September, Hobart, Australia.
2019	Riddell, A. R., King, M. A., Watson, C. S., *Up & Down: Vertical land motion of the Australian continent*, The International Union of Geodesy and Geophysics 8-18 July, Montreal, Canada.
2019	Riddell, A. R., King, M. A., Watson, C. S., Brennand S., *Deformation of the Australian Continent from Intraplate and Far-field Earthquakes*, American Geophysical Union Fall Meeting, 8-12 December, San Francisco, United States of America.

D.4 Professional development and research exchanges

Year	Event
2016	Seven Secrets of Highly Successful Research Students, 29 July, Hobart, Australia.
2017	Australia-Germany Joint Research Cooperation Scheme, 28 April - 4 May, Bonn, Germany.
2018	France-Australia Science Innovation Collaboration Fellowship, 5-20 May, Toulouse, France.
2018	British Council, FameLab Australia, 28 March, Melbourne Australia.
2018	Theo Murphy Grant, Early Mid Career Research Science Pathways 2018: Diversify your thinking, 23-24 April, Brisbane, Australia.

D.5 Media and outreach

Year	Citation
2017	Riddell, A. R., King, M. A., *Melting ice and satellites: how to measure the Earth's 'wiggle'*, The Conversation. https://theconversation.com/melting-ice-and-satellites-how-to-measure-the-earths-wiggle-77799
2018	Lusuan, A. *The woman who explores Australia's outback to measure the Earth's sea level*, Angies Ink Untold: Women in Science. https://sketchessciencestories.wordpress.com/2018/01/15/the-woman-who-explores-australias-outback-to-measure-the-earths-sea-level/
2018	Wright, C., *Tides of time - analysing changes in sea level to reconstruct Earth's history*, NatureVolve, 1, pp. 5-8. https://issuu.com/naturevolve/docs/naturevolve_issue_1_summer_high_res
2019	xyHt, *Outlook 2019, 40 under 40 Remarkable Geospatial Professionals*, https://www.xyht.com/surveying/anna-riddell/
2019	AGU, *Deformation of the Australian Continent from Intraplate and Far-Field Earthquakes*, [video file], retrieved from https://www.youtube.com/watch?v=L0Yvu5e1CDE